Self-Assembly of Faceted Colloidal Particles

Cover: A mosaic, obtained from simulations of a binary mixture of hard squares and triangles. The composition ratio of triangles to squares is 0.36. The particles are given random colors.

PhD thesis, Utrecht University, the Netherlands, January 2015.
ISBN: 978-94-6108-881-9
A digital version of this thesis is available at https://web.science.uu.nl/SCM/

Self-Assembly of Faceted Colloidal Particles

Self-Assembly of Faceted Colloidal Particles

(met een samenvatting in het Nederlands)

Proefschrift

ter verkrijging van de graad van doctor aan de Universiteit Utrecht op gezag van de rector magnificus, prof. dr. G. J. van der Zwaan, ingevolge het besluit van het college voor promoties in het openbaar te verdedigen op maandag 12 januari 2015 des middags te 12.45 uur

door

Anjan Prasad Gantapara

geboren op 23 maart 1983 te Dharmavaram, India

Promotor: Prof. dr. ir. M. Dijkstra

Contents

1 Introduction **1**
- 1.1 Colloids 2
- 1.2 Polyhedral Colloidal Particles 3
- 1.3 Hard Particles 3
- 1.4 Simulations 4
  - 1.4.1 Monte Carlo Simulations 5
  - 1.4.2 Floppy-box Monte Carlo Simulations 6
  - 1.4.3 Separating Axis Theorem 7
  - 1.4.4 Free-Energy Calculations 8
- 1.5 Thesis Outline 9

2 Phase Behavior of a Family of Truncated Hard Cubes **11**
- 2.1 Introduction 12
- 2.2 Simulation Model 12
- 2.3 Simulation Methods 13
  - 2.3.1 Order Parameters and Correlations Functions 13
  - 2.3.2 Free-Energy Calculations and Confining Potentials 14
- 2.4 Results 15
  - 2.4.1 Determining the Close-Packed Structures 15
  - 2.4.2 Close-Packed Structures 17
  - 2.4.3 Equations of State and Mesophase Structures 21
  - 2.4.4 Mesophase Lattice Vectors 22
  - 2.4.5 Phase Diagram 23
  - 2.4.6 Plastic Crystal Phases 28
- 2.5 Conclusions 32
- 2.6 Acknowledgments 33

3 Vacancies in Simple Cubic Crystals of Truncated Hard Cubes **35**
- 3.1 Introduction 36
- 3.2 Methods 36
  - 3.2.1 Free Energy of a Solid with Vacancies 36
- 3.3 Results 37
- 3.4 Cell Theory Calculations 39
- 3.5 Conclusions 42
- 3.6 Acknowledgments 43

4 Phase Diagram of Colloidal Hard Superballs: from Cubes via Spheres to Octahedra **45**
4.1 Introduction 46
4.2 Model, Methods and Simulations 47
4.3 Results and Discussion 48
4.3.1 The Phase Behavior of Hard Octahedra 48
4.3.2 Octahedron-like Superballs ($0.5 \leq q < 1$) 54
4.3.3 Cube-like Superballs ($1 < q < \infty$) 55
4.4 Conclusion 57

5 Self-Assembly of Colloidal Hexagonal Bipyramid- and Bifrustum-Shaped Nanoparticles into Two-Dimensional Superstructures **59**
5.1 Introduction 60
5.2 Interfacial Adsorption 61
5.3 Monte Carlo Simulations 63
5.4 Conclusions 66
5.5 Acknowledgements 67

6 Phase Diagram of 2D Hard Triangles: A Novel Chiral Phase with Chiral Holes **69**
6.1 Introduction 70
6.2 Methods 71
6.3 Results 73
6.4 Conclusions and Summary 80
6.5 Acknowledgments 80

7 Dispersion Relations for Colloidal Crystals with Diffusion **81**
7.1 Introduction 82
7.2 Theory and Methods 82
7.2.1 Method 1 83
7.2.2 Method 2 83
7.3 Results 84
7.3.1 Hard Spheres 85
7.3.2 Gaussian-Core Particles 85
7.4 Conclusions 89
7.5 Acknowledgments 89

References **91**

Summary **102**

Samenvatting **104**

Acknowledgments **107**

List of Publications **109**

1

Introduction

In this chapter we give a brief introduction to colloids, the simulation methods that we used in this thesis, and an overview of the results chapters. We start with a description of colloids, anisotropic colloids and their self-assembly. We follow this by an overview of the recent developments in the synthesis of anisotropic colloidal particles. Later, we briefly describe the simulation methods used in this thesis followed by an outline to the rest of the thesis.

1.1 Colloids

Colloids are insoluble microscopic particles that are suspended in a substance. A colloid is a particle for which at least one of its dimension is within the size range of a nanometer to a micron [1]. Most colloidal particles are visible in an optical microscope although one needs an electron microscope to visualize nanocolloids. We encounter colloids in our daily life more often than we are aware off. For example butter, salad dressing, mayonnaise, paints, toothpaste, and creams *etc.*, fall into the realm of colloids. Also, colloids are widely used in emerging technologies such as photonic materials, advanced ceramic processing, and 3D-ink-jet technology. A better understanding of colloids not only contributes to the advancement of above mentioned products and technologies but also to our fundamental understanding of matter at micrometer and nanometer scales.

In 1905, Albert Einstein published, as part of his "Annus mirabilis" papers, his work on Brownian motion of colloids [2]. The Brownian motion of a colloidal particle is due to its collision with the surrounding fluid molecules, which are in constant motion because of the thermal energy they possess. Using the kinetic theory of fluids, Einstein derived an expression for the mean square displacement for colloids suspended in a liquid. During this process he also lent credence to Ludwig Boltzmann's statistical mechanics, which had been controversial at that time. In the following years, Jean Baptiste Perrin performed sedimentation experiments [3, 4] on colloids (gamboge particles) and verified Einsteins theoretical predictions that colloids should obey the gas laws. Furthermore, Perrin calculated Avogadro's number and Boltzmann's constant, quantities relevant for atomic systems, from his sedimentation experiments on colloids. Perrin won a Noble Prize in Physics in 1926 for these experiments. Perrin's experiments illustrated that studying colloids can reveal information about atomic systems and that the behavior of colloids is similar to that of atoms.

Brownian motion allows colloidal particles to explore phase space in a similar fashion as thermal motion does for atomic systems. Colloidal particles suspended in a fluid interact with each other in addition to the background interaction with the fluid atoms/molecules. These interactions among the colloids let them exhibit phase behavior similar to that of atomic systems. It is well known that colloids can exhibit rich phase behavior similar to their atomic and molecular counterparts. For example colloids can self-assemble not only into gas, liquid, solid phases but also nematic, smectic, biaxial, hexatic phases as also found for atomic and molecular systems. The type of phases that could emerge in a colloidal system not only depends on the interaction potential between the colloidal particles but also on the shape of the colloidal particle itself. With the advancement of synthesis techniques a wide variety of anisotropic colloids are available to perform self-assembly experiments and to explore their complex phase behavior [5]. In this thesis we study the effect of colloid shape on the phase behavior. In particular, we study the phase behavior of experimentally available polyhedral particles using Monte Carlo simulations.

1.2 Polyhedral Colloidal Particles

Anisotropic colloidal particles like rods [6–8] and discs [9] were long known. Recent breakthroughs in the experimental techniques to synthesize new anisotropic particles have led to a plethora of anisotropic colloidal particles like triangles [10, 11], squares [12], cubes [13, 14], tetrahedra [15], truncated cubes, octahedra [16], superballs [17], hexagonal bi-pyramids [18], icosahedra [19], tetrapods [20], stars [21–23], clusters of spheres [24] and Janus particles [25, 26]. Modern computer platforms have made it possible to perform simulations of these systems, which have resulted in an improved understanding of the experimentally observed phenomenology in colloidal suspensions of these anisotropic particles.

In this thesis we restrict ourselves to the phase behavior studies of polyhedron-shaped building blocks, such as faceted nanocrystals and colloidal particles. Recent interests in the synthesis and self-assembly of polyhedron-shaped particles [5, 13, 27–37] motivates to study the phase behavior of these basic building blocks. The ability to perform self-assembly experiments with these polyhedron-shaped particles [16, 37–43] have attracted the interests of physicists, mathematicians, and computer scientists [44–50]. Predicting the densest packings of hard polyhedra has intrigued mathematicians since the time of the early Greek philosophers, such as Plato and Archimedes [51, 52].

We study the phase behavior of these experimentally available polyhedral particles using hard-particle models. Hard-particle systems are toy model systems to realistic systems, which captures the essential physics and are sufficient at times to understand the experimentally observed self-assembled structures [16, 53, 54]. Simulating polyhedral particles with more complex interactions than the hard-core interactions is interesting and is necessary at times [55], however it lies beyond the scope of this thesis.

1.3 Hard Particles

Hard particles are simple model systems to investigate the role of shape on the phase behavior. For two arbitrary objects R_1 and R_2 the hard-core interaction energy is given as follows:

$$u(R_1, R_2) = \begin{cases} \infty, & \text{if } R_1 \text{ and } R_2 \text{ overlap} \\ 0, & \text{otherwise} \end{cases} . \tag{1.1}$$

This hard-core interaction mimics the strong repulsion between the atoms at close distances, due to the overlap of their outer electronic shells. A hard-core interaction is an idealized representation of repulsive potentials. This explains why the hard-core potential, e.g., the hard-sphere potential, is successful in modeling liquids, glasses and solids [56]. Similarly, hard-core interactions are used to explain the thermodynamics of colloidal systems [56–59]. Many colloidal particles behave like hard particles under certain conditions. For example, long-range electrostatic repulsion between charged colloids are tuned by adding salt to the solvent (increasing ionic concentration of the solvent) which will effectively screen the interaction to be a short-range repulsion [60].

Studies on entropy-driven disorder-order phase transitions in hard-particle systems dates back to the 20$^{\text{th}}$ century. The earliest example of an entropy-driven ordering transition is described in a classic paper of Lars Onsager, where he showed that infinitely long rigid rods exhibit an isotropic-nematic transition [61]. Similarly, John Kirkwood along with his student Bernie Alder predicted that hard spheres crystallize at packing fraction $\phi = 0.5$ [62]. In 1957, Bernie Alder and Tom Wainwright showed using molecular dynamics simulations, and William Wood and J. D. Jacobson using Monte Carlo simulations, that hard spheres exhibit a first-order melting transition, see Ref. [63–65]. Following in similar footsteps, Daan Frenkel, Henk Lekkerkerker and Alain Stroobants have shown that hard rods of finite length exhibit nematic and smectic phases in addition to a crystalline phase [66]. Since then, several ordered phases have been observed for hard-particle systems [16, 49, 50, 54, 67, 67–69].

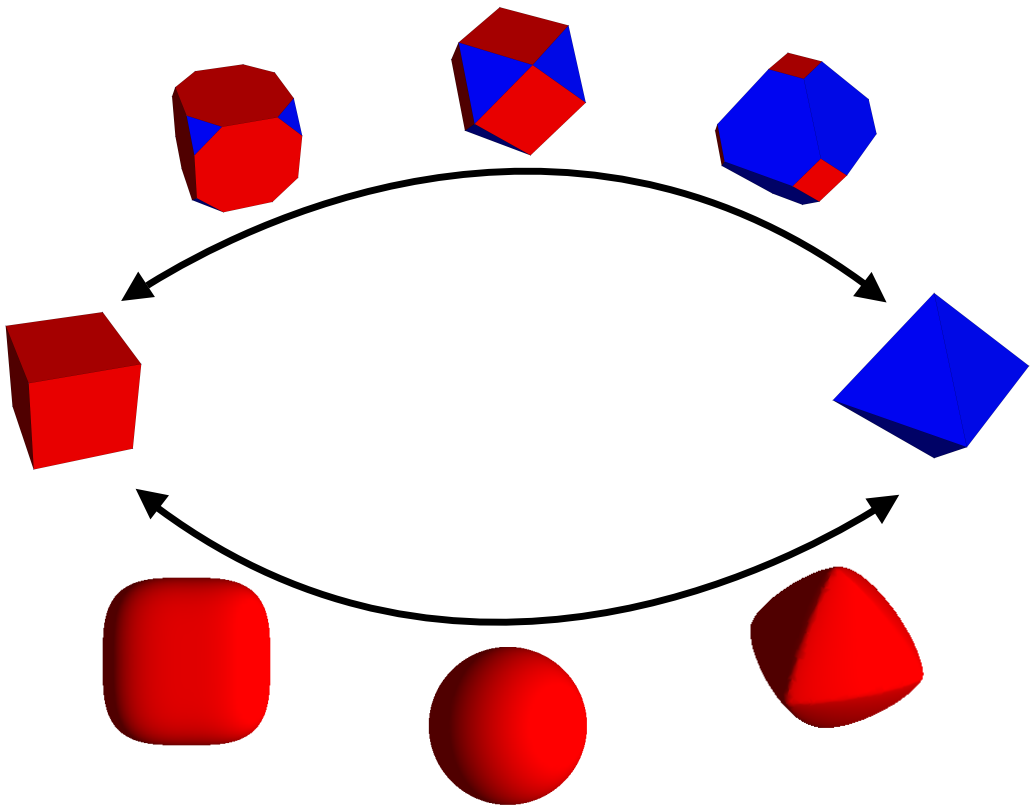

Figure 1.1: Top arrow shows the family of truncated cubes studied in Chapter 2 and the bottom arrow shows the superballs family studied in Chapter 4. These two families are bounded by a cube and an octahedra.

1.4 Simulations

In this thesis we investigate the phase behavior of faceted nanocrystals and colloidal particles shown in Fig. 1.1 and Fig. 1.2 using Monte Carlo simulations. The rest of this

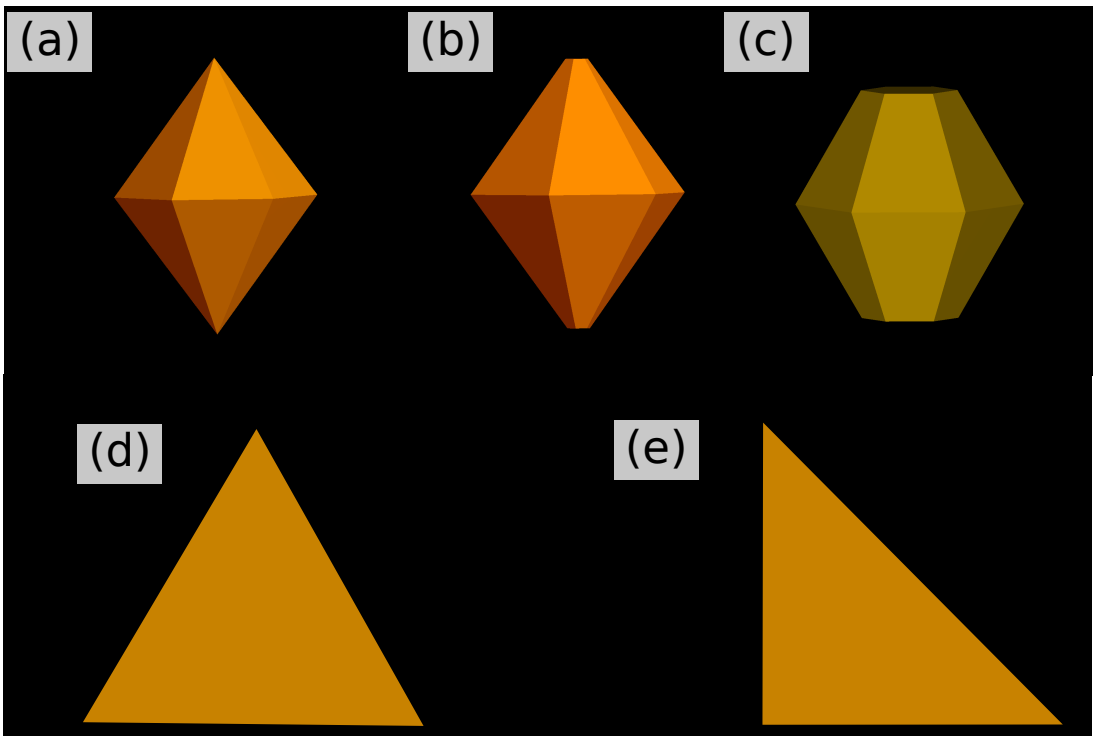

Figure 1.2: Other polyhedral and polygon-shaped particles studied in this thesis. (a) Hexagonal bi-pyramid, (b) truncated hexagonal bi-pyramid (c) hexagonal bi-frustum, (d) equilateral triangle and (e) right-angled isosceles triangle.

introductory chapter is reserved for a brief introduction to the simulation methods used to determine the phase behavior of the anisotropic particles followed by an outline for the remainder of this thesis.

1.4.1 Monte Carlo Simulations

The Monte Carlo method is a powerful numerical technique to solve complex problems using random numbers. We use a Markov chain Monte Carlo method namely the Metropolis algorithm, also called Metropolis-Hastings algorithm, to study the equilibrium phase behavior of many-body systems. Markov chain Monte Carlo simulations allow us to sample the phase space according to a given probability distribution function.

In a canonical ensemble the probability of a configuration with particle positions $\bar{\mathbf{r}}^N$ and Hamiltonian $\mathcal{H}\left(\bar{\mathbf{r}}^N\right)$ is given by the Boltzmann distribution function as

$$P\left(\bar{\mathbf{r}}^N\right) = \frac{\exp\left(-\beta\mathcal{H}\left(\bar{\mathbf{r}}^N\right)\right)}{Q}, \tag{1.2}$$

where $\beta = \frac{1}{k_\mathrm{B}T}$ is the inverse temperature with k_B the Boltzmann's constant and T the temperature, N is the number of particles and

$$Q = \int d\bar{\mathbf{r}}^N \exp\left(-\beta\mathcal{H}\left(\bar{\mathbf{r}}^N\right)\right), \tag{1.3}$$

is the configurational integral. The canonical ensemble is also called the NVT ensemble as the number of particles N, the volume of system V, and the temperature T are kept constant. Thus, the expectation value of a thermodynamic observable A is given by

$$\langle A \rangle = \int d\bar{\mathbf{r}}^N A\left(\bar{\mathbf{r}}^N\right) P\left(\bar{\mathbf{r}}^N\right). \tag{1.4}$$

We use the Metropolis algorithm to compute the expectation value, which allows us to do the calculation without computing Q. For this we first need to generate a Markov chain of configurations using the Boltzmann probability distribution function in Eq. 1.2. Once the system has reached equilibrium we compute the expectation value of A as

$$\langle A \rangle = \frac{1}{M} \sum_{k=1}^{M} A\left(\bar{\mathbf{r}}^N\right), \tag{1.5}$$

where M is the number of uncorrelated equilibrium configurations. The Metropolis algorithm helps us to sample from the phase space region that corresponds to a high Boltzmann weight and hence will allow us to converge to the averaged values with small error bars.

In a NVT ensemble, one can start with a random initial configuration in which there are no overlaps between the hard particles. At each Monte Carlo step we either randomly displace or rotate, a randomly chosen particle at a time. The implementation of Metropolis algorithm for hard particles in an NVT ensemble is easier because the change in potential energy at every Monte Carlo move is either ∞ or 0. Due to this reason, we accept every random configuration with unit probability if there are no overlaps between the particles and reject every configuration that has overlaps between the particles.

Similarly, in an NPT ensemble where pressure P is fixed instead of the volume, we can use the Metropolis algorithm to perform volume moves in addition to particle moves. The trial volume move from a volume V to a new volume $V' = V + \Delta V$, with ΔV the change in volume which is uniformly chosen over the interval $[-\Delta V_{\max}, \Delta V_{\max}]$, is accepted with probability $min\{1, \exp -(\beta \Delta H)\}$. Here

$$\Delta H = \Delta u + P\Delta V - k_{\mathrm{B}} T N \log\left(V'/V\right), \tag{1.6}$$

is related to the change in enthalpy of the system due to scaling the particle coordinates by a factor of $f = \left(\frac{V'}{V}\right)^{1/3}$, where Δu is the associated change in potential energy. If the move is rejected we restore the old coordinates and repeat the procedure in combination with the particle moves. We use floppy-box NPT Monte Carlo simulations to compute the equations of state. For a detailed description of the Monte Carlo simulation methods see Ref. [70].

1.4.2 Floppy-box Monte Carlo Simulations

The floppy-box Monte Carlo (FBMC) simulation is an isothermal-isotensic NPT Monte Carlo method to simulate colloidal particles in a stress-free environment [71, 72]. The main difference between a regular NPT Monte Carlo method and FBMC method is that the three vectors that span the simulation box are allowed to vary independently of each

other in both their lengths and relative orientations. In a regular NPT simulation we scale the whole box preserving the relative dimensions of the box vectors and their orientations. This method in combination with the separating axis theorem is used to determine close-packed structures as well as the equations of state for hard-anisotropic particles, for more details see Ref. [71].

1.4.3 Separating Axis Theorem

The separating axis theorem (SAT), also known as the hyperplane separation theorem is a widely used algorithm to detect overlaps of convex objects. The theorem states that if two convex objects do not overlap then there exists at least one axis onto which the projections of the objects do not intersect. For regular 3D convex polyhedra the number of direction vectors one has to test to determine the separating axis is a finite set. That set includes normal vectors to the faces of the polyhedra and vectors generated by a cross product of two edges, one from each polyhedron. Similarly, for 2D convex polygons the number of direction vectors one has to test consists of normal vectors to the edges of the polygon. If none of the direction vectors from this finite set does not emerge as a separating axis then the particles have an overlap. Figure 1.3 illustrates the separating axis theorem method for two non-intersecting 2D polygons.

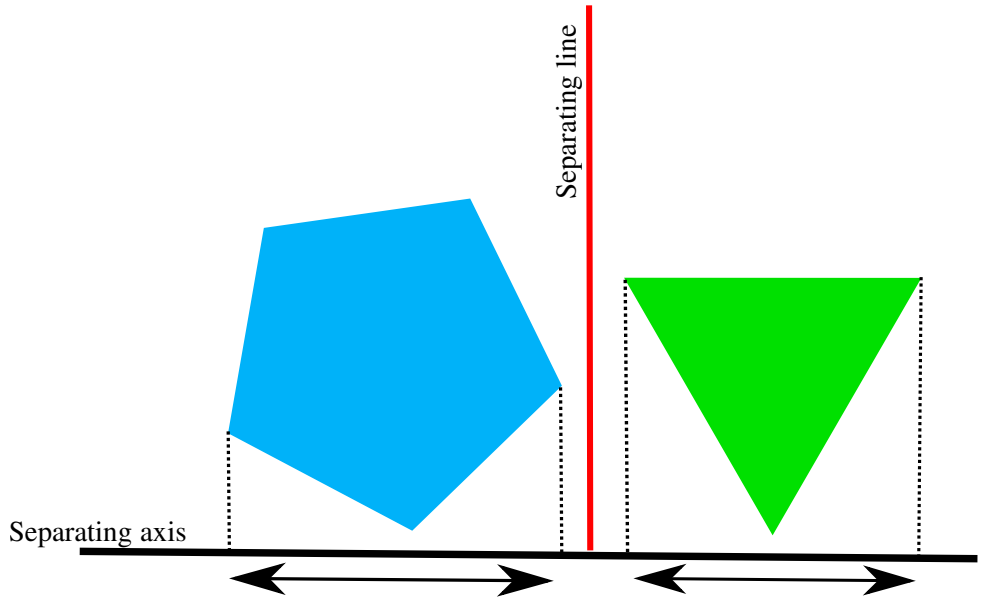

Figure 1.3: Visual illustration of SAT, for a pentagon and a triangle. The separating axis is indicated by the horizontal black line. The vertical red line indicates the separating line (plane) for the polygons. Note that the projections of the polygons, represented by double headed arrows, onto the separating axis do not intersect indicating no overlap between the particles.

SAT is computationally expensive, especially if the objects under consideration for overlap detection have a large number of edges and faces. The number of edges and faces of a polyhedra (polygon) goes up with its asphericity, *i.e.,* how strong the particle shape deviates from that of a sphere (disk). Therefore the number of computations to

determine a separating axis increases for particles with high asphericity. For fast overlap detection one can avoid using parallel axes. To further speed up the procedure we use the circumscribed and inscribed circle/sphere check before we switch to the more complex SAT method to detect overlaps. We first check if the distance between the particles is larger than twice the radius of the circumscribed circle, if so, there is no overlap. Then we check if the distance is smaller than twice the radius of the inscribed circle, if so, there is an overlap. If the distance between the particles is somewhere in between we use SAT to check for overlap.

1.4.4 Free-Energy Calculations

The thermodynamic potential corresponding to a canonical ensemble is given by the Helmholtz free energy

$$F = -k_{\mathrm{B}}T \log Z, \tag{1.7}$$

where Z is the partition function and is given by

$$Z = \frac{Q}{N!\Lambda^N}, \tag{1.8}$$

with Λ the de Broglie wavelength. As there are no direct ways to calculate the partition function for a many-body system, we resort to alternative techniques to compute the free energy. There are many simulation methods in use to determine the free energy of a thermodynamic system. For example, Wang-Landau method, multi-canonical Monte Carlo method, Frenkel-Ladd method *etc.*. Here we use the Frenkel-Ladd method [70, 73, 74] in combination with thermodynamic integration of the equation of state to determine the exact free energy of the crystals over a range of densities. The idea behind the Frenkel-Ladd method is to convert the system of interest into an ideal non-interacting simple harmonic crystal, quasi-statically. The amount of work done in this quasi-static process is equal to the change in the free energy ΔF. The free energy of a simple harmonic crystal F_{Harmonic}, also referred as the Einstein crystal, is known analytically. The free energy of the crystal under consideration, say F, is then given by

$$F = \Delta F + F_{\mathrm{Harmonic}}. \tag{1.9}$$

Once the free energy of the system is known at a given density ρ_0 we can compute the free energy for any density of interest using thermodynamic integration,

$$\frac{\beta F(\rho)}{N} = \frac{\beta F(\rho_0)}{N} + \int_{\rho_0}^{\rho} \frac{\beta P(\rho')}{\rho'^2}\,\mathrm{d}\,\rho'. \tag{1.10}$$

Here N is the number of particles in the system and ρ is the number density.

In the case of fluids, the Helmholtz free energy at reference density ρ_0 is obtained using the Widom's particle insertion technique [75]. More details about the implementation details of both methods and the confining potentials to convert a crystal into an Einstein crystal will be discussed in more detail in Chapter 2.

1.5 Thesis Outline

Here we briefly outline the rest of the thesis. In Chapter 2, we present our study on the phase behavior of a family of truncated cubes. In addition to the phase behavior, we also study and compute the equilibrium vacancy concentration of these truncated cubes in Chapter 3. Then we proceed to study the phase behavior of superballs in Chapter 4. We then describe the phase behavior of hexagonal bi-pyramids and hexagonal bi-frustums adhered at a liquid-air interface and compare our results to the experimentally obtained structures in Chapter 5. In Chapter 6 we study the phase behavior of equilateral and right-angled isosceles triangles in 2D. Finally, in Chapter 7 we compute the dispersion relations for colloidal crystals which exhibit diffusion using a recently developed theoretical technique.

2

Phase Behavior of a Family of Truncated Hard Cubes

We discuss the thermodynamic phase behavior of a family of truncated hard cubes, where the shape evolves smoothly from a cube *via* a cuboctahedron to an octahedron. We used Monte Carlo simulations and free-energy calculations to establish the full phase diagram. Surprisingly, this phase diagram exhibits a remarkable diversity in crystal structures and distinct close-packed structures, including a fully degenerate crystal structure and vacancy-stabilized crystal phases, all depending sensitively on the precise particle shape. Our results are not only crucial for better understanding the relation between phase behavior and building-block shape, but they are also of interest for guiding future experimental studies on polyhedral-shaped nanoparticles.

2.1 Introduction

Recent advances in experimental techniques to synthesize polyhedron-shaped particles, such as faceted nanocrystals and colloidal particles [5, 13, 27–37], and the ability to perform self-assembly experiments with these particles [16, 37–43] have attracted the interests of physicists, mathematicians, and computer scientists [44–48]. Modern computer platforms have made it possible to perform simulations of these systems, which has resulted not only in an improved understanding of the experimentally observed phenomenology in colloidal suspensions of such particles, but also improved ansätze for the morphology of their close-packed configurations [45, 50, 67, 76–78].

Recently, Henzie *et al.* [16] reported the shape-controlled synthesis of truncated cubes. In their research the close-packed crystals of these particles were studied using sedimentation experiments and simulations. They created exotic superlattices and their results also tested several conjectures on the densest packings of hard polyhedra [44, 46–48]. However, Henzie *et al.* did not examine the finite-pressure behavior of the system. At finite pressures the structures that form by self-assembly, may differ substantially from the packings achieved at high (sedimentation and solvent-evaporation) pressures. For instance, liquid-crystal, plastic-crystal, vacancy-rich simple cubic, and quasicrystalline mesophases are obtained under non-close-packed conditions in similar systems [50, 67, 76–80].

In this Chapter we present our investigation of the full phase behavior of a family of truncated hard cubes, which interpolates smoothly between cubes and octahedra (the mathematical dual of the cube) *via* cuboctahedra. Our Monte Carlo simulation studies and free-energy calculations show that the phase diagram for this system exhibits a remarkably rich diversity in crystal structures that depends sensitively on the particle shape. We found distinct changes in phase behavior and crystal structures even for small variations in the level of truncation. This is an unexpected result, since the particle shape varies smoothly from that of a cube to that of an octahedron by truncation. Moreover, we found that the equilibrium concentration of vacancies increases at a fixed packing fraction ϕ upon increasing the level of truncation within the vacancy-rich simple cubic phase, which will be discussed in detail in Chapter 3. Our results differ from the Monte Carlo results for parallel cuboids, where the vacancy concentration remains constant, when the shape is varied from a perfect cube to a sphere *via* rounded cubes (so-called cuboids) [80]. In this Chapter we describe in detail the different phases that we obtained, as well as the nature of the phase transitions between these phases.

2.2 Simulation Model

The particles that we investigated are completely specified by the level of truncation of a perfect cube, which we denote by $s \in [0, 1]$, and the volume of the particle. We define our family of truncated cubes using a simple mathematical expression for the location of the vertices. The line segments that connect these vertices can only be assigned in one (unique) way to obtain a truncated cube. The vertices of a truncated cube may be

written as a function of the shape parameter $s \in [0,1]$:

$$\{\mathbf{v}(s)\} = \begin{cases} \left(1-\frac{4}{3}s^3\right)^{(-1/3)} \mathcal{P}_D\left(\pm\left(\frac{1}{2}-s\right), \pm\frac{1}{2}, \pm\frac{1}{2}\right)^T & \text{if} \quad s \in \left[0, \frac{1}{2}\right] \\ \left(\frac{4}{3}-4\lambda^3\right)^{(-1/3)} \mathcal{P}_D\left(\pm(1-\lambda), \pm\lambda, 0\right)^T & \text{if} \quad \lambda \equiv 1-s \in \left[0, \frac{1}{2}\right] \end{cases}, \tag{2.1}$$

where $\mathcal{P}_D$ is a permutation operation that generates all permutations of each element in the sets of 8 and 4 vertices spanned by the $\pm$-operations, respectively. The duplicate vertices evolving out of our definition are removed after letting $\mathcal{P}_D$ act. The 'T' indicates transposition. The prefactors ensure that the truncated cubes are normalized to unit volume. Several Platonic and Archimedean solids are members of this family: $s = 0$ a cube, $s = (2-\sqrt{2})/2 \approx 0.292893$ a truncated cube, $s = 1/2$ a cuboctahedron, $s = 2/3$ a truncated octahedron, and $s = 1$ an octahedron; these are depicted in Fig. 2.1a.

2.3 Simulation Methods

2.3.1 Order Parameters and Correlations Functions

In this subsection we describe different order parameters we have used to quantify the positional and orientational order of particles in our isothermal-isobaric Monte Carlo simulations also called NPT simulations (fixed pressure P, temperature T and number of particles N) of the truncated cubes. These order parameters play a crucial role in identifying different phases exhibited by the truncated cubes. Truncated cubes have cubatic symmetry. To quantify the orientational order for these particles the cubatic order parameter S_4 is appropriate as shown in earlier simulation studies on cubatic particles [77, 81]. The cubatic order parameter is defined as

$$S_4 = \max_{\mathbf{n}} \left\{ \frac{1}{14N} \sum_{i,j} \left(35|\mathbf{u}_{ij}\cdot\mathbf{n}|^4 - 30|\mathbf{u}_{ij}\cdot\mathbf{n}|^2 + 3\right) \right\}, \tag{2.2}$$

where N is the number of particles as above, $\mathbf{u}_{ij}$ is the unit vector of the j^{th} axis of particle i and $\mathbf{n}$ is a unit vector for which S_4 is maximized. S_4 values range from 0 for a completely disordered system to 1 for perfect crystals.

To investigate the structural correlations in the particle orientations we use an orientational correlation function $g_4(r)$ defined as

$$g_4(r) = \frac{3}{14}\left\langle 35[\mathbf{u}_{aj}(0).\mathbf{u}_{bj}(r)]^4 - 30[\mathbf{u}_{aj}(0).\mathbf{u}_{bj}(r)]^2 + 3 \right\rangle, \tag{2.3}$$

where $\langle . \rangle$ denotes the ensemble average over all the particle axes $j \in \{x, y, z\}$ and particle pairs a and b. For more details about the definitions and computation of these order parameters we would refer the interested reader to Ref. [81].

To determine the translational order in the system we use the radial distribution function $g(r)$ defined as

$$g(r) = \frac{1}{\rho^2}\left\langle \sum_{i=1}^{N}\sum_{j\neq i}^{N} \delta\left(\mathbf{r}-\mathbf{r}_i\right)\delta\left(\mathbf{r}'-\mathbf{r}_j\right) \right\rangle, \tag{2.4}$$

with $r = |\mathbf{r} - \mathbf{r}'|$, $\delta(x)$ is the usual Kronecker δ-function, $\mathbf{r}_i$ and $\mathbf{r}_j$ are the positions of the i^{th} and j^{th} particle, respectively and $\rho = \frac{N}{V}$ is the number density of the system. The radial distribution function along with the order parameters is useful to distinguish plastic crystal from crystal and isotropic fluid phases.

2.3.2 Free-Energy Calculations and Confining Potentials

We obtained the dimensionless free energy per particle $f = \beta F/N$ as a function of packing fraction $\phi = \frac{Nv_p}{V}$, with v_p the particle volume ($\phi = \rho$, since $v_p = 1$ in this Chapter), for the entire density range by thermodynamic integration [70] over the equation of state (EOS), from reference density ρ_0 to the density of interest ρ:

$$f(\rho) = f(\rho_0) + \int_{\rho_0}^{\rho} \frac{\beta P(\rho')}{\rho'^2}\, \mathrm{d}\,\rho'. \tag{2.5}$$

Here $f(\rho_0) \equiv \beta\mu(\rho_0) - \beta P(\rho_0)/\rho_0$ is the reduced Helmholtz free energy per particle at density ρ_0, with $\beta = 1/k_{\mathrm{B}}T$, T the temperature and k_{B} the Boltzmann constant, $\mu(\rho_0)$ the chemical potential, and $P(\rho_0)$ the pressure. The Helmholtz free energy at reference density ρ_0 was obtained as follows.

1. In the fluid phase we used Widom's particle insertion method [75] to obtain the free energy. This method was employed at relatively low densities to obtain small error bars. We performed the calculations at $\phi \approx 0.2$. We note that there were no finite size effects within the computational accuracy for the particle insertion method.

2. In the crystal phase we used the Einstein integration method [70, 73, 74]. The reduced Helmholtz free energy per particle $f = \beta F/N$ of a crystal is given by:

$$f(\rho) = f_{\mathrm{Einst}}(\lambda_{\max}) - \frac{1}{N}\int_0^{\lambda_{\max}} \mathrm{d}\lambda \left\langle \frac{\partial \beta U_{\mathrm{Einst}}(\lambda)}{\partial \lambda} \right\rangle, \tag{2.6}$$

   where f_{Einst} denotes the reduced free energy per particle of the ideal Einstein crystal, which is given by:

$$\begin{aligned} f_{\mathrm{Einst}}(\lambda_{\max}) \;=\; & -\frac{3(N-1)}{2N}\log\left(\frac{\pi}{\lambda_{\max}}\right) + \\ & \log\left(\frac{\Lambda_t^3\Lambda_r}{v_p}\right) + \frac{1}{N}\log\left(\frac{v_p}{VN^{1/2}}\right) - \\ & \frac{1}{N}\log\left\{\frac{1}{8\pi^2}\int \mathrm{d}\theta\sin(\theta)\mathrm{d}\phi\mathrm{d}\chi \times \right. \\ & \left. \exp\left[-\frac{\lambda_{\max}}{k_B T}(\sin^2\psi_{ia} + \sin^2\psi_{ib})\right]\right\}. \end{aligned}$$

   $U_{\mathrm{Einst}}(\lambda)$ denotes the harmonic potential that fixes the particles to the respective Einstein lattice positions:

$$\beta U_{\mathrm{Einst}}(\lambda) = \lambda \sum_{i=1}^{N} [(\mathbf{r}_i - \mathbf{r}_{i,0})^2/v_p^{2/3} + (\sin^2\psi_{ia} + \sin^2\psi_{ib})], \tag{2.7}$$

with $(\mathbf{r}_i - \mathbf{r}_{i,0})$ the displacement of particle i from its position in the ideal Einstein crystal. The angles ψ_{ia} and ψ_{ib} are the minimum angles between vectors, **a** and **b**, describing the orientations of the particles in the ideal Einstein crystal and the equivalent vectors that describe the orientation of the particle in the actual crystal, respectively. When λ is large the translational and orientational displacements of the particles are frozen, while at lower λ's the particles freely displace and rotate not only to explore the possible states but also to explore the underlying degeneracy coming from the symmetry of the particle itself. The translational and rotational thermal wavelengths Λ_t and Λ_r are set to 1 in our calculations. We mostly used the same system sizes of 700 to 1,500 particles to compute the free energies for the (plastic) crystal phases. We found that finite-size scaling (FSS) was only necessary in the octahedron regime, *i.e.*, $s \approx 1$, to establish the phase diagram. For such high levels of truncation the free-energy differences between the various phases at coexistence proved to be very small, see Ref. [77]. For the other phase transitions the free energies obtained without FSS proved to be sufficient to accurately determine the phase boundaries.

3. For the free-energy calculations of a plastic-crystal (rotator) phase, we followed the approach of the authors of Ref. [82], who introduced a method, which allows for a continuous transition from a non-interacting plastic-crystal to an interacting plastic-crystal phase of hard truncated cubes. We used a tunable soft-to-hard interaction potential between the particles

$$\varphi(i,j) = \begin{cases} \gamma[1 - A(1 + \zeta(i,j))] & \text{if } \zeta(i,j) < 0 \\ 0 & \text{otherwise} \end{cases}, \tag{2.8}$$

where $\zeta(i,j)$ is the overlap potential defined in Ref. [83], which is negative when two particles i and j overlap and positive otherwise, and γ is the integration parameter, which runs from $\gamma = 0$ (noninteracting) to $\gamma = \gamma_{\max}$, for which the system interacts fully. In our calculations we have set $A = 0.9$ following Ref. [69]. The dimensionless Helmholtz free energy per particle of the plastic crystal is given by:

$$\begin{aligned} f(\rho) \;=\; & f_{\text{Einst}}(\lambda_{\max}) - \\ & \frac{1}{N}\int_0^{\lambda_{\max}} \mathrm{d}\lambda \left\langle \frac{\partial \beta U_{\text{Einst}}(\lambda)}{\partial \lambda} \right\rangle_{\gamma_{\max}} + \\ & \frac{1}{N}\int_0^{\gamma_{\max}} \mathrm{d}\gamma \left\langle \frac{\partial \sum_{i\neq j}^{N} \beta\varphi(i,j)}{\partial \gamma} \right\rangle_{\lambda_{\max}} . \end{aligned}$$

2.4 Results

2.4.1 Determining the Close-Packed Structures

The simulations by which the close-packed structures were derived, are based on the floppy-box Monte Carlo (FBMC) method [71, 72] in combination with the separating-axis-based overlap algorithm [84]. We obtained the densest crystal structure and the

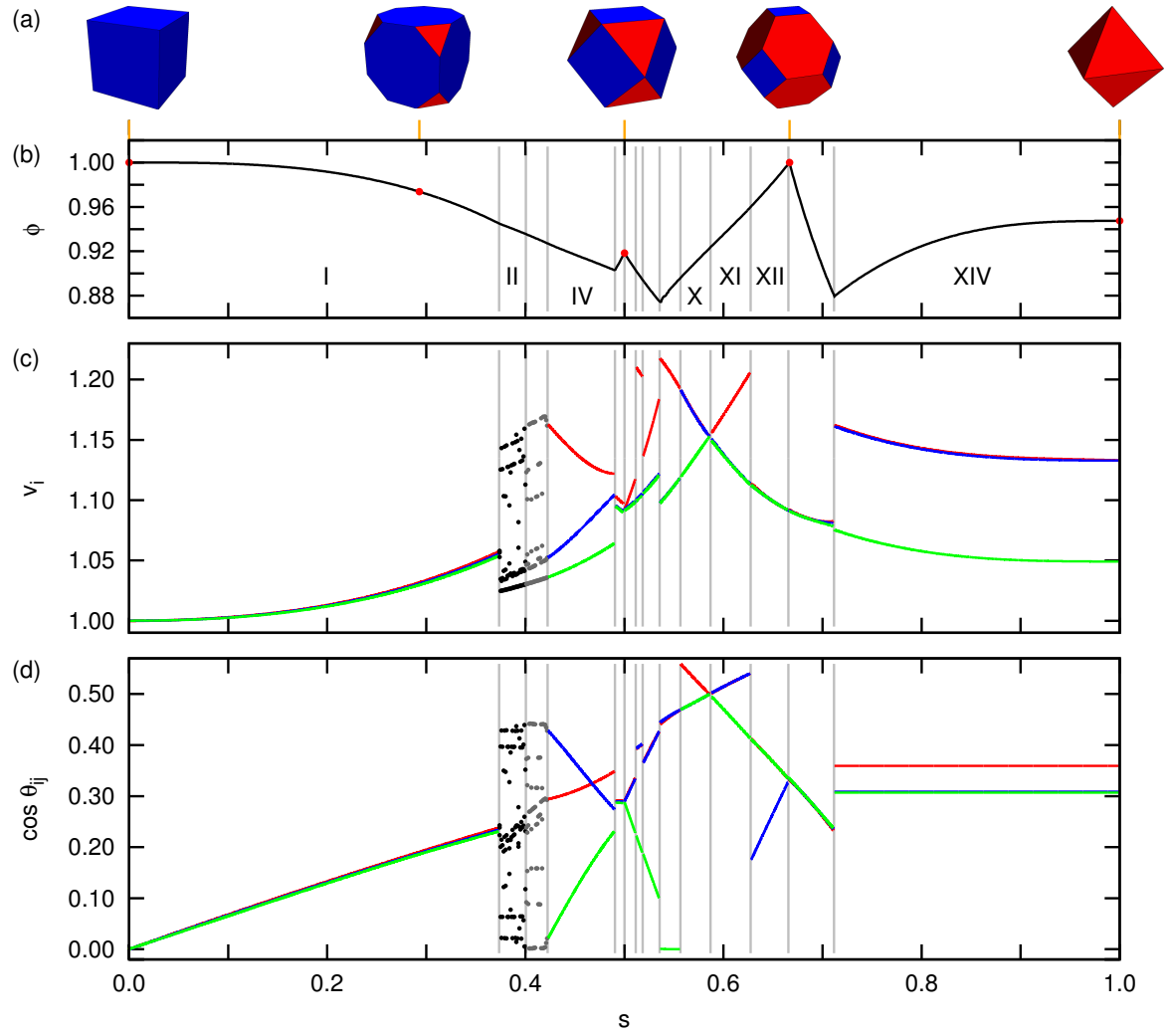

Figure 2.1: (a) Five examples of truncated cubes (Platonic and Archimedean solids only) for levels of truncation s corresponding to the orange lines: $s = 0$ a cube, $s = (2 - \sqrt{2})/2 \approx 0.293$ a truncated cube, $s = 1/2$ a cuboctahedron, $s = 2/3$ a truncated octahedron, and $s = 1$ an octahedron. (b) The packing fraction ϕ for the close-packed structures as a function of s. The values for the five solids shown in (a) are given by red dots. (c) The length v_i ($i = 1$, 2, and 3) of the three lattice vectors, indicated in red, green, and blue, that span the unit cell of the densest crystal structure as a function of s. Not every line is clearly visible, since there is some overlap. In the region where the black and gray dots are used ($s \in (0.37, 0.40]$ and $s \in (0.40, 0.42]$), appears to be a degeneracy in the crystal structures, as explained in the text. (d) The cosine of the angles θ_{ij} ($i < j = 1$, 2, and 3) between the three vectors that span the unit cell as a function of s. Gray vertical lines partition the s-domain into 14 pieces with a 'different' crystal structure, based on the discontinuities shown in the v_i and $\cos\theta_{ij}$ results. These regions are numbered with roman numerals in (b); only those regions large enough to accommodate a label are numbered, but the numbering can be continued from left to right, in the unnumbered regions.

corresponding packing fraction ϕ as a function of the level of particle truncation s by considering 1,000 equidistant points in $s \in [0, 1]$. For each point we prepared systems

of truncated particles in a dilute phase, typically with packing fraction $\phi \approx 0.001$. We increased the reduced pressure in 100 steps according to a geometric series from $p = 1$ to $p \approx 10^5$ over 4×10^6 Monte Carlo (MC) cycles in order to compress these systems to a high-density crystalline state. This pressure increase was typically applied a total of 1,000 times for $N = 1$ particles in the unit cell and for each shape. We restricted ourselves to $N = 1$ particles in the unit cell, because the truncated cubes are all centrosymmetric. We only considered $N = 2, \ldots, 6$ for 14 conveniently chosen values of s, located in the center of the regions indicated in Fig. 2.1, as will be justified shortly. For these $N > 1$ systems we obtained roughly the same value of ϕ and also the same crystal structures. The densest crystal-structure candidate was selected and allowed to compress further for another 10^6 MC cycles at $p = 10^6$ to achieve 5 decimals of precision in ϕ. In practice, these final cycles of compression did not improve the packing fraction substantially. Fig. 2.1b shows ϕ as a function of s. Note that the packing fraction 'curve' is continuous, but has discontinuities in its first derivative. To double check our result, we considered another set of FBMC runs. We used several of the 1,000 densely-packed crystals as our initial configuration and we varied s around these points at high pressure to study the evolution of their structure. Steps of 10^{-5} in s were used and for each step the system is expanded to remove any overlaps, before re-compressing it at $p \approx 10^5$. The packing fractions we obtained showed good correspondence with our original result, but this correspondence failed for a transition between two crystal structures. The consecutive method would often become stuck in the lower density structure that corresponded to the morphology of the crystal phase it came from.

The unit cell for $N = 1$ truncated cubes can be specified by three vectors $\mathbf{v}_i$ ($i = 1$, 2, 3) that are implicitly s dependent. The structure spanned by these three vectors can also be described by the length $v_i = |\mathbf{v}_i|$ of the vectors and the angles θ_{ij} ($i < j = 1$, 2, 3) between them. Note that we ignored the orientation of the particle with respect to the unit cell here. In order to give an unbiased comparison of the different vectors we used lattice reduction [85] to ensure that for each unit cell the surface to volume ratio is minimal. These results are shown in Fig. 2.1(c,d). By analyzing the v_i and θ_{ij}, as well as the location of the kinks in the ϕ-curve, we were able to partition the $s \in [0, 1]$ domain into 14 distinct regions. This is the reason behind our choice of 14 verification points for $N > 1$ simulations. For a discussion of the crystal structures in the different regions, we refer the reader to Sec. 2.4.2.

2.4.2 Close-Packed Structures

In this section we discuss the properties of the close-packed structures that are obtained using the methods described in Sec. 2.4.1. Fig. 2.2 shows the crystal structure in the center of each of the 14 regions that we found in Fig. 2.1. There is a strong difference between the domains $s < 1/2$ and $s > 1/2$. Geometrically the cuboctahedron ($s = 1/2$) is the transition point between shapes which have a more cube-like nature and shapes which have a more octahedron-like nature. It is therefore not surprising that the crystal structures in the two regions ($s < 1/2$ and $s > 1/2$) appear to have a deformed simple cubic symmetry and a deformed body-centered tetragonal symmetry, respectively. We illustrate this in Fig. 2.2 where we show the most orthorhombic unit cell: $N = 1$ for

$s < 1/2$ and $N = 2$ for $s > 1/2$. A remarkable result is the stability of the Minkowski crystal [48], which is the densest-packed Bravais-lattice structure for octahedra [46], under variations in s. For all $s \in [0.71, 1]$, we find a Minkowski structure in the dense-packed limit, which can be inferred from the horizontal $\cos\theta_{ij}$ lines in Fig. 2.1d. The scaled length of the vectors $v_i\phi^{-1/3}$ is also constant on this domain.

Let us now examine the crystal structures in the 14 regions identified by the discontinuities in the vectors of the unit cell. In literature it has become commonplace to assign atomic equivalents to structures observed in simulations or experiments. For example, this is done for binary mixtures of spheres [72, 86], a family of truncated tetrahedra [67], several faceted particles [50], and systems of nanoparticles [53, 54]. We attempted to follow suit by determining the symmetry group of the structures in Fig. 2.2 using *FindSym* [87] and by subsequently assigning an atomic equivalent [88]. However, we found that a description in terms of atomic equivalents inadequately captures the richness in crystal structure, since particle orientation is not taken into account. Moreover, for many of our structures we are unable to determine a nontrivial space group using *FindSym*. We therefore resorted to visual analysis and we used this to group the 14 regions in Fig. 2.1 based on similarities between the respective structures.

1. **I** In this region ($s \in [0.00, 0.37]$) we obtained a continuous and uniform distortion of the simple cubic structure for cubes. For $s = 0$ the particles form a simple cubic (SC) crystal, which has the same morphology as αPo (α-Polonium) [88]. The uniformly distorted simple cubic (UDSC) structure we found for $s > 0$ is similar to that of βPo [88]. We verified this distorted quality for values as low as $s = 10^{-5}$.

2. **II & III** For these two regions ($s \in (0.37, 0.40]$ and $s \in (0.40, 0.42]$) we found that there is a degeneracy in the crystal-structure candidates that achieve the densest-known packing. Although certain structures appear favored over others, there is no clear relation between the structure and s. However, the packing fraction ϕ of the close-packed crystals is continuous in these regions. The observed degeneracy can be explained by the formation of sheets consisting of diagonally-interlocked columns, which can slide up or down (in the direction of the columns) with respect to each other, as shown in Fig. 2.3. For $s = 0.387$, the truncated cubes are arranged in a distorted simple cubic (DSC) crystal lattice, where the particles form columns that are interlocked in a diagonal way. These structures are referred to as mono-interlocking distorted simple cubic (MI-DSC) crystals. This diagonal interlocking together with the close-packing condition prevents lateral motion in the plane normal to the column's direction. However, since the system is not fully interlocked, motion in the direction of the columns is possible for the diagonally interlocked sheets. We refer to these structures as mono-interlocking distorted simple cubic (MI-DSC) crystals. This degeneracy is different from the degeneracy that occurs in structures consisting of cubes or hexagonal prisms for instance, since such systems allow lateral freedom of movement of columns or (perpendicular to the columns) of sheets of aligned particles. That is, there is possible freedom of motion in three directions, albeit not necessarily at the same time. The interlocking nature of the MI-DSC phase only allows for movement in one direction only, namely parallel to the columns, which

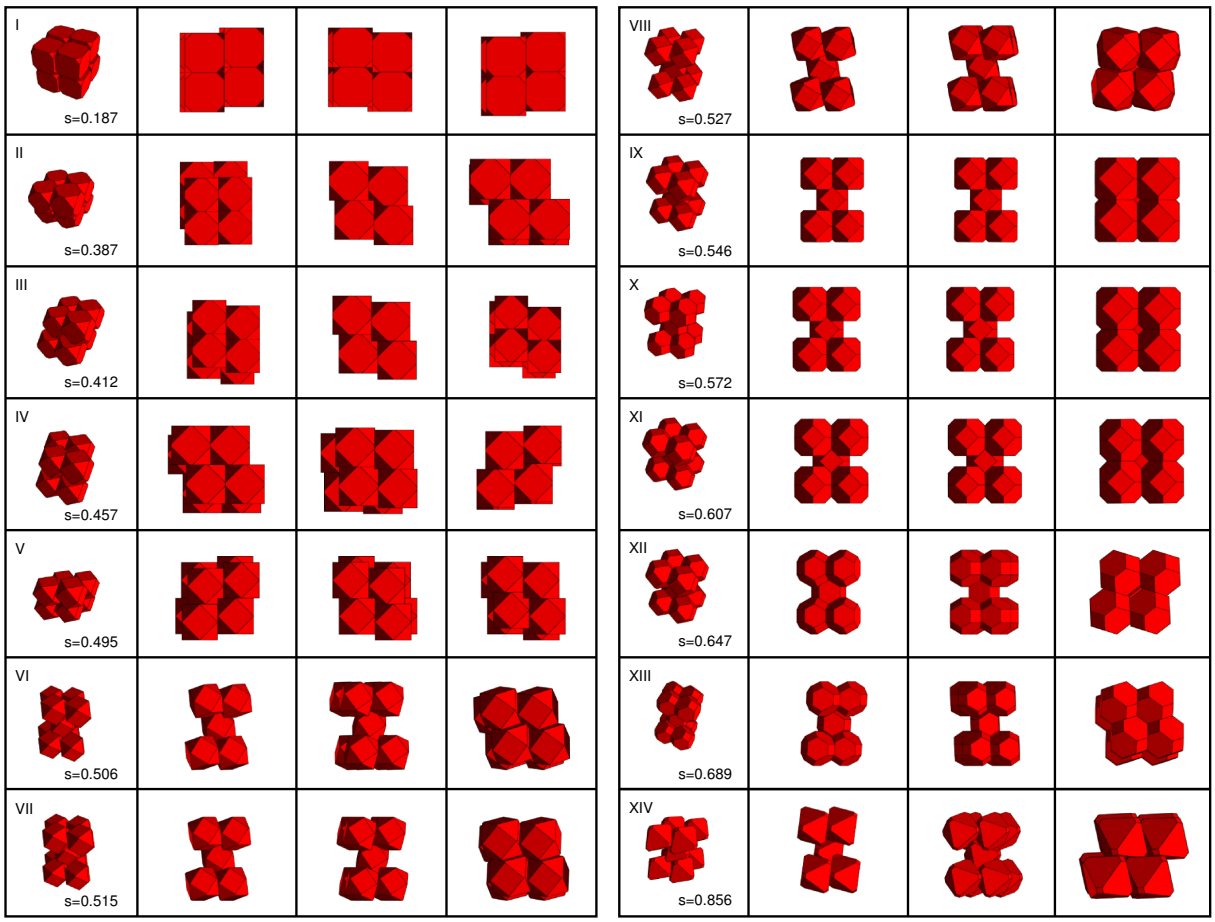

Figure 2.2: Visual representations of the crystal structures obtained for the first 7 regions (left) and the last 7 regions (right) of Fig. 2.1. From left to right each entry (row) contains a bird's eye view, the front view, the side view, and the top view of this structure. The Roman numeral in the top-left corner gives the relevant domain in Fig. 2.1. The truncation parameter s for these structures is given in the bottom-right corner.

may lead to strong rheological differences between this structure and, *e.g.*, the SC structure for cubes.

3. **IV** For this region ($s \in (0.42, 0.49]$) we find a DSC phase that is interlocking in two directions: a bi-interlocking DSC (BI-DSC) phase. For each instance of interlocking two degrees of translational motion are frozen out. This implies that the BI-DSC structure is completely fixed, which is confirmed by the unicity of the v_i and θ_{ij} results in Fig. 2.1(c,d).

4. **V** In this region ($s \in (0.49, 0.50]$) we observed a tri-interlocking DSC (TI-DSC) phase.

5. **VI - VIII** Here ($s \in (0.50, 0.51]$, $(0.51, 0.52]$, and $(0.52, 0.54]$) we found structures that are best described by a distorted body-centered tetragonal (DBCT) structure. The truncated cubes in these crystals are not aligned with the axes of the unit cell.

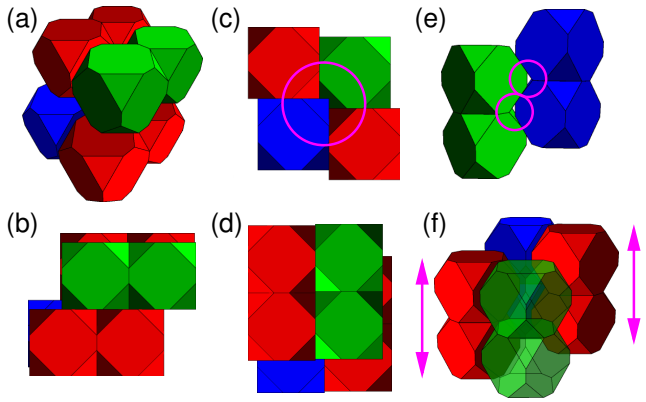

Figure 2.3: A visual representation of the degenerate crystal structure; we consider the value $s = 0.387$ in this figure. Pairs of truncated cubes, for which the octahedral faces are aligned (columns), are color-coded. Different viewpoints are displayed for a piece of crystal consisting of 8 particles: (a) Bird's eye view, (b) side view, (c), front view, and (d) top view of this structure. In (c) we use a magenta circle to indicate that the blue column is interlocking with the green column in a diagonal way. (e) A diagonal view of the crystal structure, where the red columns have been removed. Magenta circles show the interlocking. (f) The two red columns are *not* interlocking with the blue and green column, allowing for freedom of motion in the direction of the magenta arrows. The green column is made translucent to better illustrate the properties of this crystal structure.

It is unclear to what extent structures in regions VI, VII, and VIII are the same. The smooth flow of the ϕ-curve (Fig. 2.1b), as well as their appearance, s implies continuity, but the jumps in the values of v_i and θ_{ij} [Fig. 2.1(c,d)] suggest otherwise.

6. **IX - XI** These structures ($s \in (0.54, 0.56]$, $(0.56, 0.59]$, and $(0.59, 0.63]$) have a body-centered tetragonal (BCT) morphology, for which the particles are aligned with the lattice vectors of the unit cell. It is surprising that the structures in region XII exhibit a DBCT morphology, since regions IX - XII share the same smooth piece of ϕ-curve, see Fig. 2.1b. This leads us to conclude that a smooth dependence of ϕ on s is *not* indicative of uniformity in crystal structure. The strong similarity between the crystal structures in regions IX - XI and the apparent smooth transition between structures from region IX to X and from X to XI, also leads us to conclude that discontinuities in the properties of unit cell are not indicative of discontinuities in the properties of the crystal structure.

7. **XII & XIII** These two DBCT structures ($s \in (0.63, 0.67]$ and $s \in (0.67, 0.71]$) are different from the DBCT structures in regions VI - VIII, since the particles appear to be aligned with the lattice vectors of the unit cell. Moreover, crystals in region XIII are unusual, since there are large 'voids' in the structure. That is, for all other structures we found that the largest facets of a particle are always in contact with a facet of another particle. This is not the case in region XIII, because there is a substantial gap between some of the hexagonal facets.

8. **XIV** The Minkowski crystal of region XIV ($s \in (0.71, 1.00]$) is also peculiar. It is the only structure which does not undergo some form of reorganization upon varying the level of truncation. It is worthwhile to study the origin of this apparent stability, which sharply contrasts with the immediate distortion found around $s = 0$. However, this goes beyond the scope of the current investigation.

2.4.3 Equations of State and Mesophase Structures

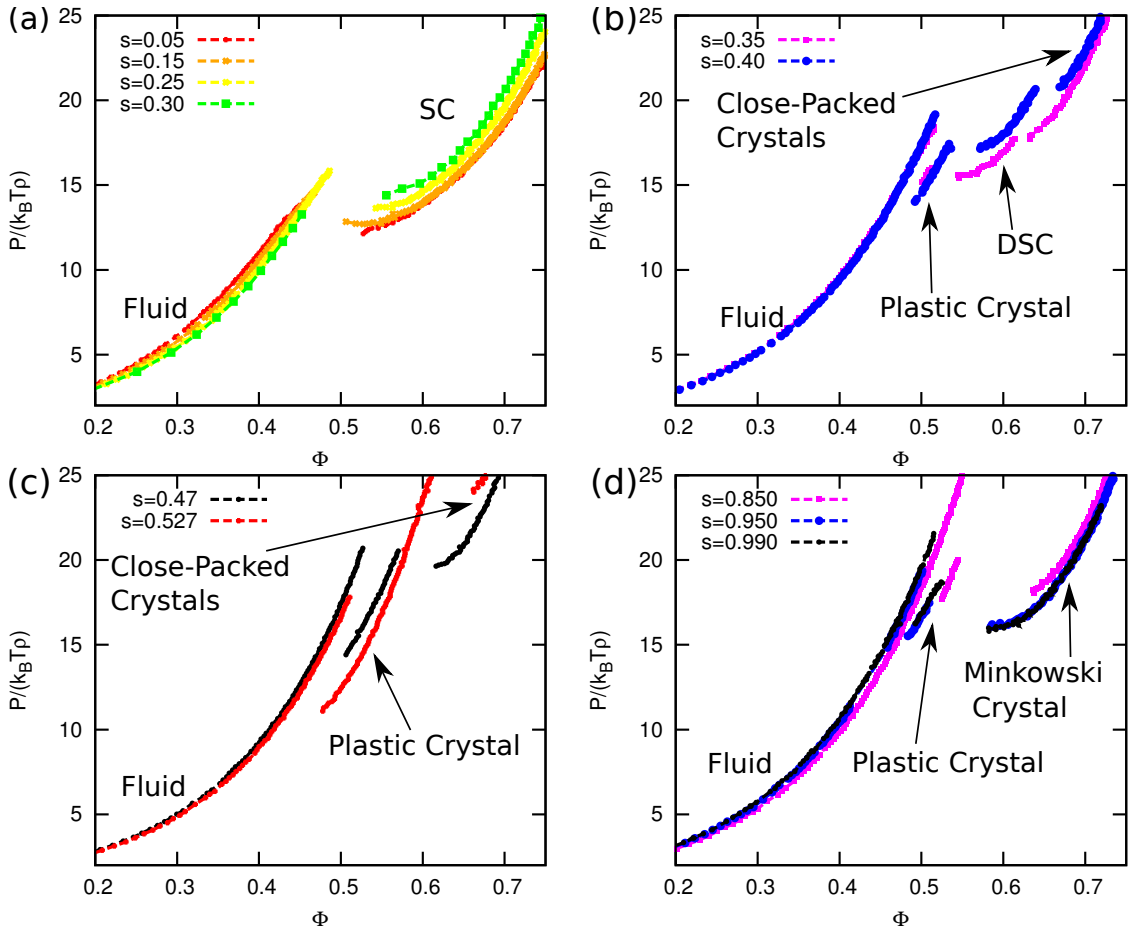

Figure 2.4: We show the reduced pressures $P/(k_BT\rho)$ as a function of packing fraction ϕ, where P is the pressure of the bulk system, ρ is the number density of the system and k_BT is the thermal energy. Equations of state of only selected shapes are shown. We have grouped the equations of state into four sets depending upon their phase behavior. More details about the figure are given in the main text.

We used the close-packed crystal structures obtained from the FBMC calculations as initial configurations for variable-box-shape isothermal-isobaric (NPT) Monte Carlo simulations, to study the phase behavior at intermediate pressures. Initial configurations of 300 to 600 particles were prepared and melted to determine the equations of state (EOSs) for the various phases. Typical equilibration times were around 1.2×10^6 Monte

Carlo sweeps (MCS) and the production times around 2×10^6 MCS. One MCS is defined as N Monte Carlo trial moves (translation, rotation, volume change, or deformation of the box, respectively), where N is the number of particles in the system. We sampled the lattice vectors, as well as the average positions and orientations of the particles as a function of packing fraction and for fixed truncation parameter s. The sampling was done on an interval of 100 MCS to avoid correlated configurations. Using these results we set up regular NPT simulations (possibly with a triclinic box shape) to more accurately sample the EOSs for all phases with larger system sizes of 1,000 to 2,000 particles, including the liquid phase.

In Fig. 2.4 we show the EOS obtained from our FBMC simulations as a function of the packing fraction. We show only EOSs for only selected shapes. The liquid EOS branches are obtained by compressing dilute systems ($\phi \approx 0.1$) while the crystalline branches of the EOS are obtained by melting the close-packed structures. We grouped the EOSs into groups depending on their phase behavior. EOSs for truncated cubes with truncation $s \leq 0.30$ are shown in Fig. 2.4a. These systems exhibit an isotropic liquid phase and a simple cubic phase separated by a first-order phase transition. During our NPT compression runs we observed that these systems crystallize easily with relatively less hysteresis compared to systems with $s > 0.7$. In Fig. 2.4b we show EOSs for $s = 0.35$ and 0.40. These two shapes, surprisingly, exhibits one isotropic phase and three crystalline phases. The rest of the EOSs in Fig. 2.4.(c,d) show three phases: liquid, plastic crystal and crystalline phase. More details about the phase behavior and individual (plastic-)crystalline phases of these systems will be given in the phase diagram Section 2.4.5. These EOSs are used to calculate the Helmholtz free energies at different packing fractions using thermodynamic integration as explained in the Section 2.3.2.

2.4.4 Mesophase Lattice Vectors

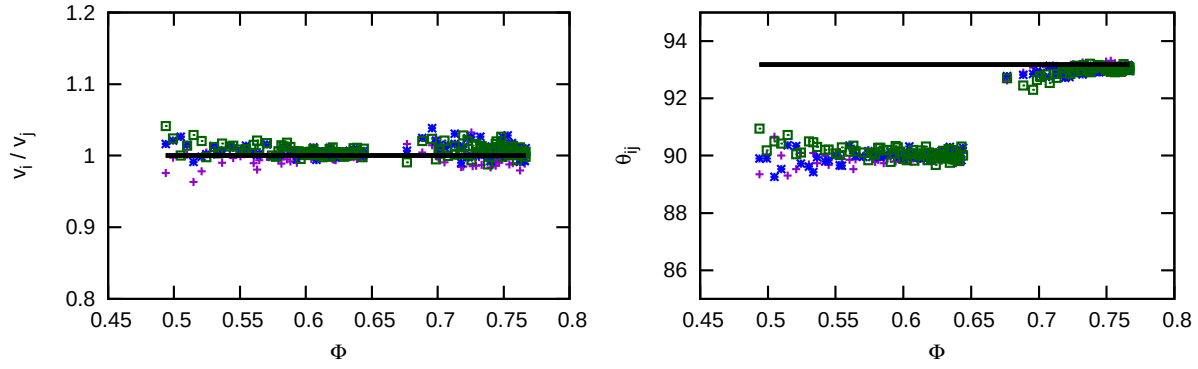

Figure 2.5: Averaged lattice vectors v_i and v_j and the angles between them θ_{ij} *vs* averaged packing fraction ϕ as obtained from our NPT simulations for $s = 0.750$. The index i,j runs over all the x,y,z components of the box as described in Section. 2.4.1. θ_{ij} values are in degrees

Before we turn our attention to the phase diagram section we explain how the NPT simulations data is used to compute free energies and to determine the crystal structure of the mesophases. To compute the free energies and also to determine the structure

of the mesophases we need to determine the inherent ideal lattice at each pressure or packing fraction. To determine the ideal lattice we need to average out the box vectors of the floppy box containing the particles and the angles between these vectors during the NPT simulations at each given pressure. Using these averaged box vectors and the angles between them we reconstruct an ideal lattice. Visual inspection of the ideal lattice helps us to determine the crystal structure. We also use the ideal lattice in the free-energy calculations as the reference Einstein crystal.

For illustration, we show such an averaging procedure for $s = 0.750$ as a function of packing fraction ϕ in Fig. 2.5. The dots in the plots represent the average values from the NPT simulations at each pressure, while the thick lines represent lattice vectors and their angles from the close-packed structure. For $s = 0.750$, the close-packed structure is the Minkowski lattice. For the Minkowski lattice $v_i/v_j = 1$ and the angle between the vectors is $\theta_{ij} \approx 93.1847°$ and for the BCC lattice $v_i/v_j = 1$ and $\theta_{ij} = 90°$. From the Fig. 2.5 we can see that the lattice vectors and the angles show a sharp transition from the close-packed Minkowski lattice to the BCC lattice. In a similar fashion we also average out the orientations and positions of individual particles in our NPT simulations to construct the ideal lattice.

2.4.5 Phase Diagram

As explained in the above sections, using the FBMC results in combination with regular isothermal-isobaric (NPT) simulations and free-energy calculations we were able to establish the full phase diagram for our hard truncated-cubes system. Fig. 2.6 shows the phase diagram for the family of truncated cubes in the packing fraction ϕ versus the level of truncation s representation. For $s < 1/2$ the particles are essentially 'cubic' in shape and we found high-density simple-cubic-like phases. The phase diagram for truncated cubes with shape parameter $s \in [0.00, 0.35]$ displays three stable bulk phases. At very high pressures, we observed a distorted simple cubic (DSC) crystal phase, which is C1-like in nature, see Ref. [76] for the definition of the C1 structure. This phase melted either *via* a weak first-order or *via* a second-order phase transition into a simple cubic (SC) crystal phase. At even lower pressures, the SC crystal is found to coexist with the fluid phase *via* a first-order phase transition. The effect of vacancies on the SC-fluid coexistence densities is not taken into account as the shift is minute. We will discuss the vacancy-rich SC phase in Chapter 3. For $s \in (0.35, 0.422]$ the phase diagram exhibits four stable phases, which are separated by three two-phase coexistence regions. At low pressures, we observed a liquid phase, which transformed into a plastic crystal phase with a hexagonal close-packed crystal structure (the PHCP phase) upon increasing the pressure. With further increasing the pressure the system underwent a first-order transition to a deformed simple cubic crystal (DSC) phase, which has a C0-like morphology, also see Ref. [76]. Finally, the system self-assembled at sufficiently high pressure into the respective densest-packed structures, *i.e.*, for $s \in (0.35, 0.374]$ the system self-assembled into a C1-like structure and for $s \in (0.374, 0.422]$ a mono-interlocking deformed simple cubic (MI-DSC) phase is formed, as discussed in the close-packed structures. We found a triple point (SC/C0 $-$ PHCP $-$ liquid) at $s \approx 0.374$. For $s \in (0.422, 0.5]$ we observed higher orders of the interlocking of the DSC crystal phase at sufficiently high pressures: a bi-interlocking DSC

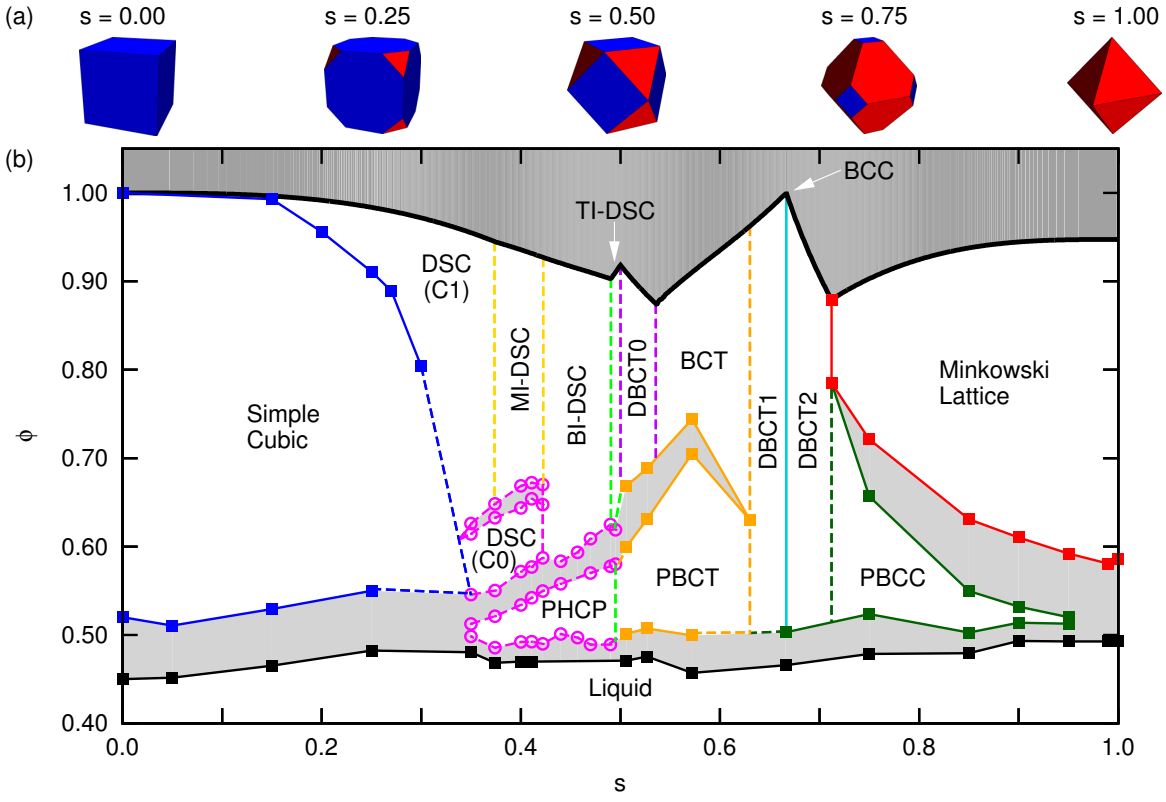

Figure 2.6: (a) Truncated cubes for five different values of the truncation parameter s. Truncated corners are shown in red. (b) Phase diagram for the family of truncated hard cubes in the packing fraction ϕ versus shape parameter s representation. In the dark-gray area ϕ exceeds the maximum packing fraction. The light-gray areas indicate the two-phase coexistence regions. The solid square symbols denote the bulk coexistence densities as obtained from free-energy calculations, while the open circles indicate those derived from the equations of state (EOSs). Coexistence lines that follow from free-energy calculations are represented by solid lines, and those that connect EOS derived points are given by dashed lines. The various labels stand for: distorted simple cubic (DSC), (distorted) body-centered tetragonal ((D)BCT), plastic BCT (PBCT), (plastic) body-centered cubic ((P)BCC), and plastic hexagonal close packed (PHCP). The prefixes MI-, BI-, TI- stand for mono-, bi-, and tri-interlocking, and the numbers that follow the DBCT label signify that these DBCT phases are distinct. The two DSC phases have different morphologies, one is C0-like, the other is C1-like. Finally, the two white arrows in the forbidden region connect the label TI-DSC to the small region between the green and purple dashed line and the label BCC with the turquoise line, respectively.

(BI-DSC) and a tri-interlocking DSC (TI-DSC) crystal, respectively. These phases melted into the PHCP phase and subsequently into the isotropic liquid phase upon lowering the pressure, again *via* first-order phase transitions in both instances. For $s \in [0.35, 0.5]$ we did not perform free-energy calculations, because there are significant fluctuations in the mean position of the particles and the averaged box vectors even for systems as large as $N \approx 1{,}000$, which interfered with obtaining a proper Einstein crystal as reference system for the thermodynamic integration method [69, 73], as described in the methods section.

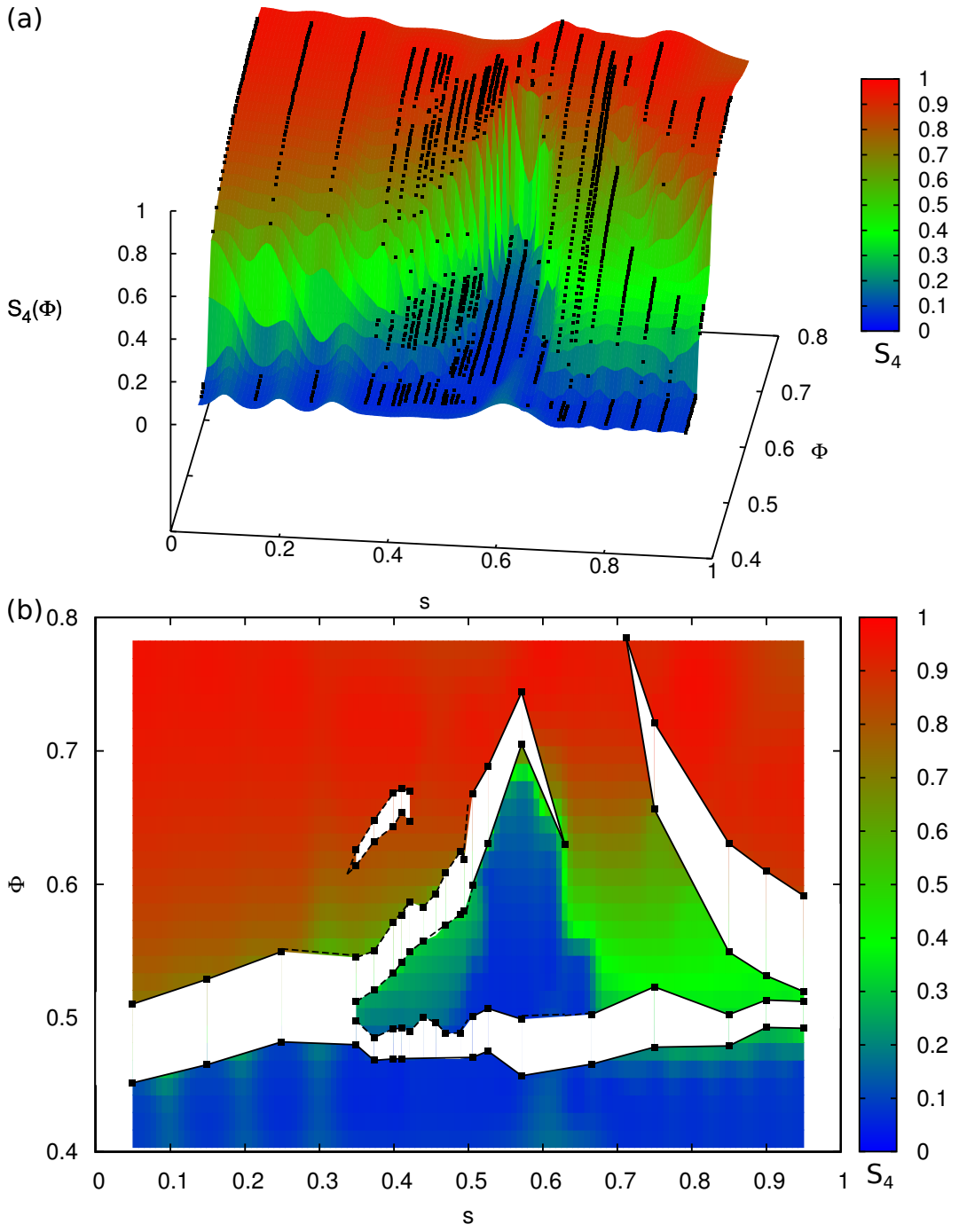

Figure 2.7: Cubatic order parameter S_4 for the family of truncated cubes. (a) Here we plot $S_4(s, \phi)$ as a function of shape s and packing fraction ϕ. The original data is displayed in black squares. We have used the original data to interpolate and create this surface plot. The surface plot is colored according to the values of $S_4(s, \phi)$ as shown in the color map. (b) We have replotted the phase diagram with a color function displayed in the color map beside the figure. The colors indicate the value of S_4 at a given point. The white regions in the plot denote the coexistence regions.

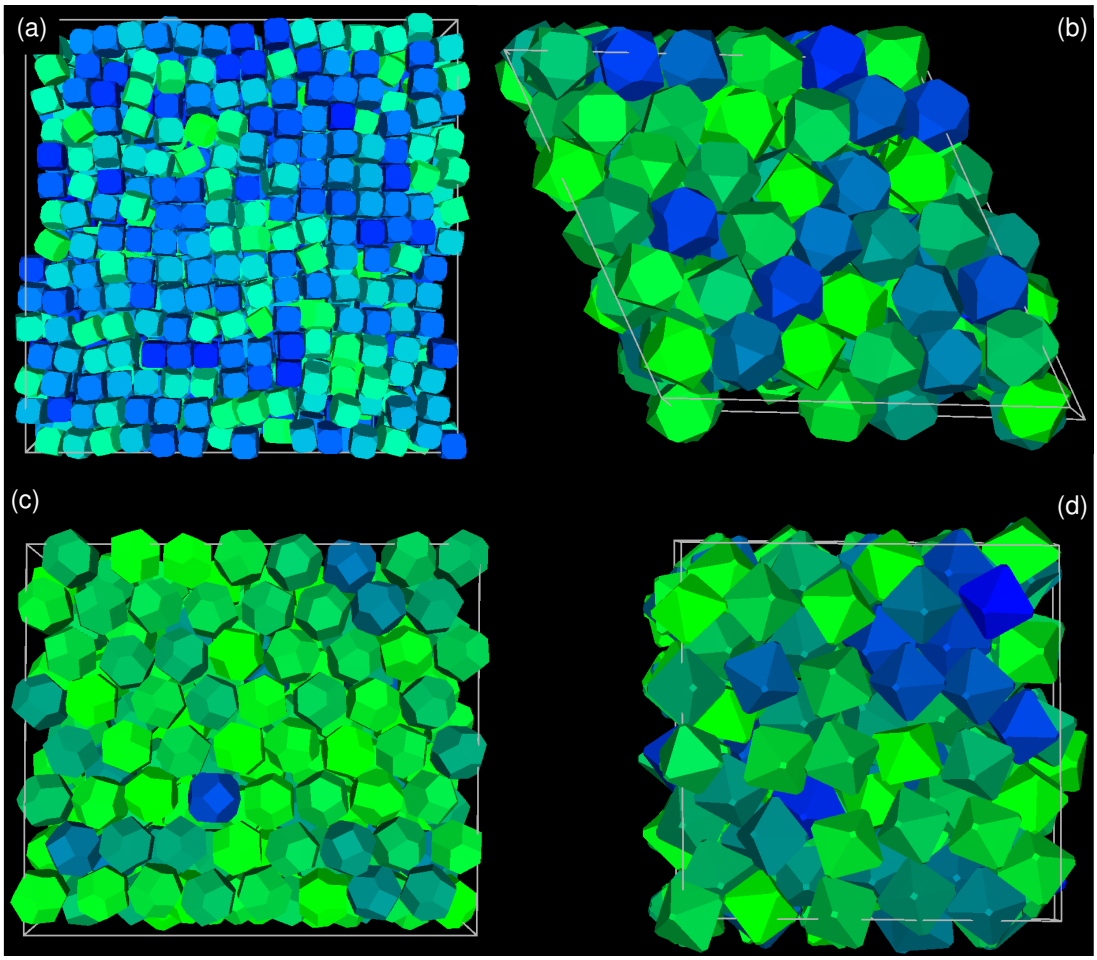

Figure 2.8: Several snapshots of our isothermal-isobaric (NPT) simulations showing the various crystal structures that form in our family of truncated cubes. (a) Equilibrium vacancy-rich simple cubic crystal for a truncation of $s = 0.25$ at packing fraction $\phi = 0.56$. The simulation was performed for $N = 3{,}235$ particles. In this system the vacancy concentration was found to be $\alpha = 0.032$. (b) Plastic hexagonal-close-packed (PHCP) phase for $s = 0.411$ and $\phi = 0.6$ in a box containing $N = 216$ particles. (c) Plastic body-centered-tetragonal (PBCT) phase for $s = 0.607$ and $\phi = 0.58$ in a box containing $N = 512$ particles. (c) Plastic body-centered-cubic (PBCC) phase for $s = 0.900$ and $\phi = 0.52$ in a box containing $N = 250$ particles. The coloring used here indicates the level of alignment of these particles with the lattice vectors of the Einstein crystal, as explained in the text.

For $s > 0.5$ the shape is 'octahedron-like', and we found body-centered-tetragonal-like (BCT-like) structures at close packing. For $s \in [0.5, 0.54]$ the close-packed distorted BCT (DBCT) phase melted into a plastic BCT (PBCT) phase upon lowering the pressure *via* a first-order phase transition. At lower pressures, we found two-phase coexistence between the PBCT and the fluid phase. In the region $s \in (0.54, 0.636]$ we obtained a regular BCT phase at high pressures, which underwent a first-order phase transition into the PBCT phase for intermediate pressures. For $s \in (0.636, 0.712]$ we found two different DBCT crystal structures (DBCT1 and DBCT2 in Fig. 2.6). The transition between

DBCT1 and DBCT2 is located at $s = 2/3$, where the particle shape is such that all sides are of equal length (the mathematical truncated octahedron; a space-filling polyhedron). Remarkably, the $s = 2/3$ system exhibits a body-centered-cubic (BCC) crystal structure, which exists only for this exact value of the truncation parameter. All crystal structures in the region $s \in (0.636, 0.712]$ melt directly into a liquid phase *via* a first-order phase transition upon decreasing the pressure. Further increasing the truncation leads to more octahedron-like shapes. In the region $s \in (0.712, 0.95]$ we found a Minkowski lattice [48] at high pressures. At intermediate pressures, this system melted into a stable plastic BCC (PBCC) phase before melting into fluid. However, for $s \in (0.95, 1.0]$ we found that the PBCC phase became metastable with respect to the solid-liquid phase transition (also see Ref. [77]), such that at $s = 0.95$ a triple point (isotropic liquid − PBCC − Minkowski crystal) appeared in the phase diagram. The straight lines separating the phase boundaries for $s \in [0.374, 0.712]$ at high packing fractions are a continuation of the subdivision that followed from the FBMC simulations. Several simulations close to the boundaries (on either side) are performed, to show that within the numerical accuracy there is no deviation from the vertical phase boundaries shown in Fig. 2.6.

Now that we have described the mesophases in the phase diagram in detail, we will turn our attention to the order in these mesophases. We have computed the cubatic order parameter S_4 defined in Eq. 2.2 as a function of packing fraction ϕ and shape s. For this we first calculated the $S_4(s, \phi)$ for selected values of s at all pressures or packing fractions and in turn used this data to interpolate and determine the cubatic order $S_4(s, \phi)$ in the entire range of $s \in [0.05, 0.95]$ and $\phi \in [0.4, 0.8]$. We show $S_4(s, \phi)$ in Fig. 2.7a using a color function. The color function is set as follows: blue is used for $S_4(s, \phi) \approx 0$, green for $S_4(s, \phi) \approx 0.4$ and red for $S_4(s, \phi) \geq 0.9$ and above, where as the remaining intermediate values are colored with the gradients of the above mentioned colors smoothly. The original $S_4(s, \phi)$ data is also plotted for comparison using black squares. From this three-dimensional plot we observe that the crystal structures of truncated cubes with shape parameter $s < 0.35$ develop global orientational order at relatively low packing fractions compared to the ones in the $s > 0.35$ region. For truncated cubes $s \in [0.35, 0.65]$ the cubatic order parameter $S_4(s, \phi)$ of the plastic crystal phases are similar to those of the isotropic fluid phase. Near $s \approx 0.58$ the cubatic order S_4 is less than 0.1 even for packing fractions as high as $\phi \approx 0.69$.

For better illustration, we replotted the phase diagram in Fig. 2.7b with a background color depending on the S_4. The colors in the Fig. 2.7b have the same meaning as in Fig. 2.7a. The white regions in the Fig. 2.7b represents the coexistence regions. The black dots in the Fig. 2.7b are the exact coexisting densities calculated from the free energies. From this plot we can infer how the order develops from the freezing densities to all the way up to the close-packed densities. We would like to point out that some of the regions near the space filling-truncated octahedra, *i.e.*, $s \approx 0.666$, close to coexistence show cubatic order values that are as low as in a plastic-crystal phase. Our results agree with the presence of low cubatic order values for $s = 0.666$ as observed by the authors of Ref. [78, 89]. However we did not indicate these particles as plastic crystals since there is no first-order phase transition between the dense crystal and the mesophase. Several typical configurations of crystalline phases slightly above fluid-solid coexistence

are displayed in Fig. 2.8 to give an impression of the mesophases that occur in the systems we studied.

2.4.6 Plastic Crystal Phases

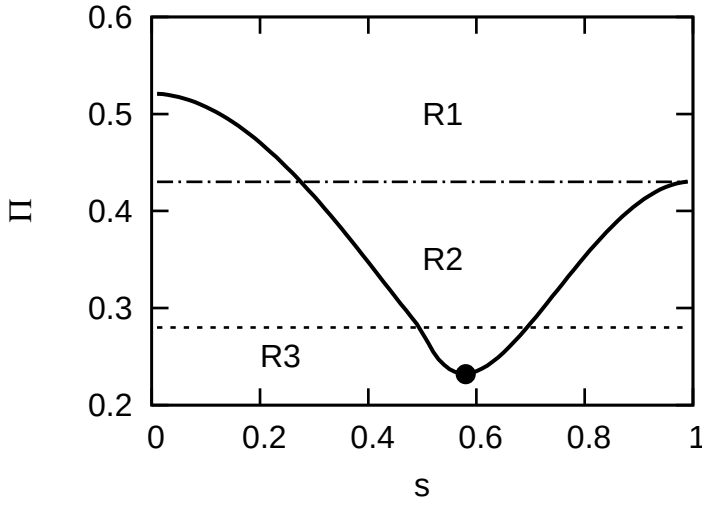

Figure 2.9: Plasticity parameter Π as a function of the shape parameter s, which defines the level of truncation of a cube. The minimum at $s = 0.58$ denotes the possibly best plastic crystal for the truncated cubes family. Depending on our observations of the phase behavior of the truncated cubes we divided the Π into three regions R1, R2 and R3. Properties of truncated cubes belonging to different regions are explained in the main text.

Plastic crystals are characterized by long-ranged positional order but short-ranged orientational order [90–92]. Recent simulation studies on hard anisotropic colloidal systems have shown the existence of intriguing plastic crystalline phases [49, 50, 77, 78]. These studies showed that the particle shape plays an important role in the formation of these plastic crystals for hard-particle systems. In addition, various physical quantities were calculated to quantify the shape of a given colloidal particle with respect to a sphere and to predict whether or not the particles will form a plastic crystal phase. Some of the quantities that were used are the asphericity and the isoperimetric coefficient, see Refs. [50, 77, 78]. The definition of the asphericity reads

$$A = 1 - \pi^{1/3} \, \frac{[6V(s)]^{2/3}}{S(s)}, \tag{2.9}$$

and that of the isoperimetric coefficient

$$I = 36\pi \frac{V(s)^2}{S(s)^3}, \tag{2.10}$$

where $V(s)$ and $S(s)$ are the volume and surface area of a truncated cube with truncation parameter s. Combining these definitions in Eq. 2.9 and Eq. 2.10 along with the moment

of inertia of the particle we define the plasticity parameter Π to quantify the shape of a given particle with respect to a unit sphere. Plasticity

$$\Pi = \sqrt{(1 - \frac{I(s)}{I_{\text{sph}}})^2 + (1 - \frac{M(s)}{M_{\text{sph}}})^2 + (1 - \frac{A(s)}{A_{\text{sph}}})^2}, \tag{2.11}$$

where $I(s)$, $M(s)$ and $A(s)$ are the isoperimetric coefficient, moment of inertia and asphericity of a truncated cube with shape parameter s, respectively, and $I_{\text{sph}} = 1$, $M_{\text{sph}} \approx 0.1539$ and $A_{\text{sph}} = 1$ are the values of a sphere with unit volume. The moment of inertia is calculated using the freely distributed code by the author of Ref. [93]. The plasticity parameter Π of truncated cubes as a function of the shape parameter is shown in Fig. 2.9. We have divided the plasticity Π plot into three different regions based on our observations of the phase behavior of truncated cubes (Fig. 2.6) and the cubatic order parameter $S_4(s, \phi)$ values (Fig. 2.7) close to the fluid-crystal and fluid-plastic-crystal phase coexistence regions. The three divisions are as follows.

1. **R1** Truncated cubes falling in this region freeze into a crystal phase with the cubatic order $S_4(s, \phi) \geq 0.7$ when compressed from a fluid phase.

2. **R2** In this region, we observed that the truncated cubes can form plastic crystals with $S_4(s, \phi) \approx 0.3 - 0.4$ when compressed from a fluid phase.

3. **R3** The region with lowest asphericity values in the family of our truncated cubes. Truncated cubes in this region can form plastic crystals with $S_4(s, \phi) < 0.1$ near the fluid-plastic-crystal phase coexistence densities.

In the remainder of this section we describe the properties of the plastic crystals found in the phase diagram in the region $s \in [0.35, 0.95]$. We found three different plastic crystal regimes namely HCP, BCT and BCC in the phase diagram of truncated cubes. To study and understand the properties of these different plastic crystal phases we have chosen three representative particle shapes $s = 0.457, 0.572$ and 0.750. We also like to point out that $s = 0.457$ and $s = 0.750$ belong to the R2 region, while $s = 0.572$ lie inside the R3 region and is close to minimum value of the plasticity parameter Π as shown in Fig. 2.9. We calculated the orientational distribution functions for these three systems at fixed pressures. Surprisingly, our results show that the plastic-crystal phase exhibits an inhomogeneous orientational distribution on a unit sphere. The orientational distributions show well-defined peaks for a few specific orientations dictated by the shape of the particle in combination with the crystal structure. We also find that some of the peaks in the orientational distribution function increase with increasing packing fraction and that some peaks, corresponding to non-cubatic symmetry, disappear when the system undergoes a transition from a plastic crystal to a solid phase.

The three particle shapes considered for this study are displayed in Fig. 2.10(a,d,g) with their orientational distribution either projected on the surface of a unit sphere or plotted as contour plot in Fig. 2.10(b,e,h) and Fig. 2.10(c,f,i), respectively. These orientational distribution functions are computed just above the fluid-plastic crystal coexistence region. In the orientations projected on the surface of a sphere we identified different

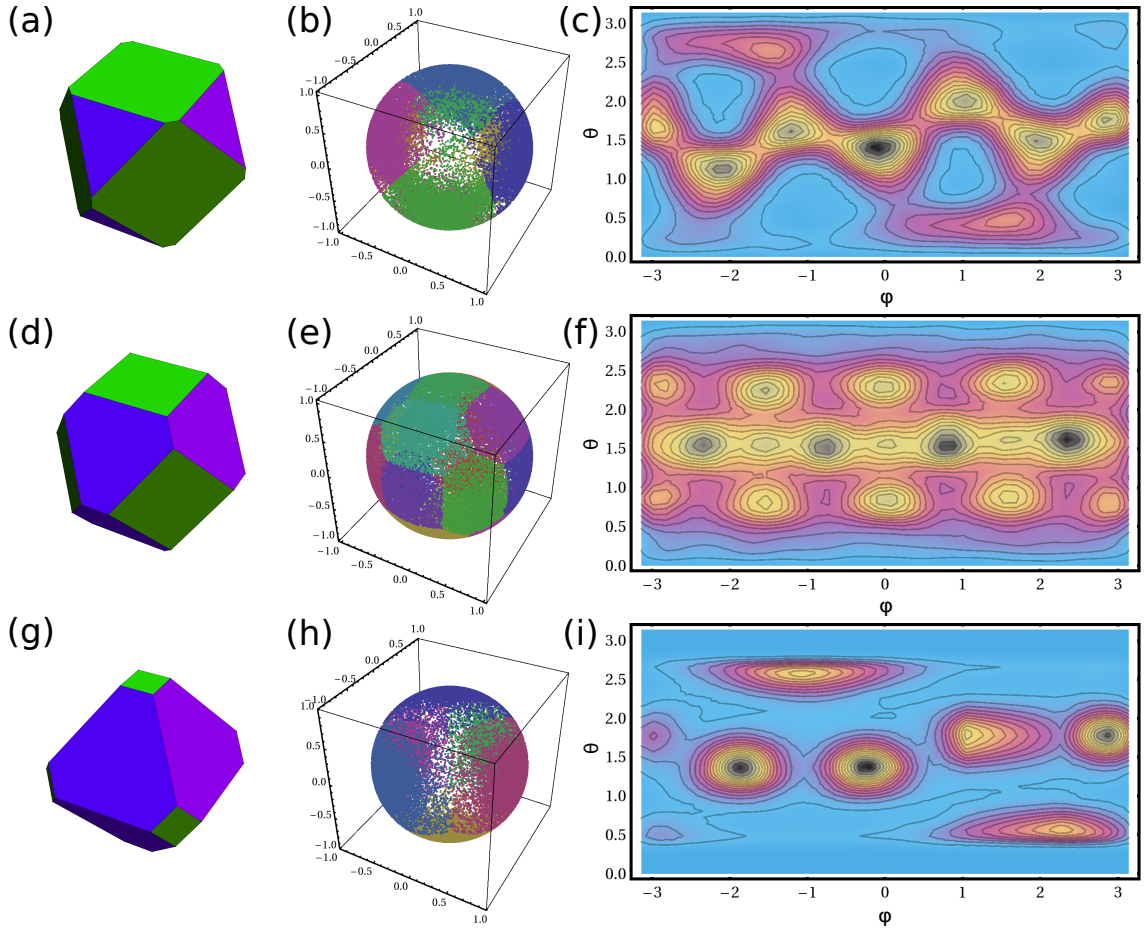

Figure 2.10: Various truncated cubes and their orientational distribution functions in the plastic crystal phase. Panels (a,d,g) show the particle shapes at truncations $s = 0.457, 0.572$ and 0.750. We have chosen these shapes to represent three different plastic crystals in the phase diagram of truncated cubes. Panels (b,e,h) show the orientations projected on the surface of a unit sphere for the particle shapes shown in (a,d,g), respectively, just above the fluid-plastic crystal phase coexistence. We have colored different clusters with different random colors. The clusters are obtained using the "FindClusters" routine in Mathematica. Panels (c,f,i) show contour plots of the corresponding orientational distribution functions in θ and φ representation. The contour plots are color coded as follows: We have used CMYK (cyan, magenta, yellow and black) color coding to explicitly show the probability density of the orientational distribution functions. Low probability regions are colored cyan and high probability regions are colored black, and the intermediate probability regions in magenta and yellow.

clusters using the Mathematica "FindClusters" routine in combination with visual observations. These clusters are randomly colored for visual clarity as shown in Fig. 2.10(b,e,h). The corresponding contour plots for the three particle shapes are shown in the (θ, φ) representation in Fig. 2.10(c,f,i). The contour plots of the orientational distribution functions are colored using four different colors (cyan (c), magenta (m), yellow (y) and black (k)) and their gradients. The order of the colors CMYK is used to determine the probability of the region *i.e.,* cyan is used to color the low probability region, while black is used

to color regions with a high probability and the remaining two colors are used for the intermediate probabilities. Most of the peaks in the contour plots are clearly visible in Fig. 2.10(c,f,i). However, we would like to note that some peaks are overshadowed by other peaks and sometimes new peaks appear due to the periodicity in θ and φ in our method of plotting. By visual observations of the orientational distribution functions along with the "FindClusters" routine we found that there are 8, 18 and 6 different peaks in the orientational distribution functions for $s = 0.457, 0.572$ and 0.750, respectively. We also note that truncated cubes with $\Pi \in$ R2 ($s = 0.457$ and 0.750) have a smaller number of peaks compared to the ones with $\Pi \in$ R3 ($s = 0.572$). Additionally, we found that the cubatic order is inversely proportional to the number of peaks in the orientational distribution function, *i.e.,* more peaks in the orientational distribution functions gives rise to a lower cubatic order.

Now that we have described the three different plastic crystals we will study the orientational distribution of a plastic crystal as a function of packing fraction ϕ. We have chosen $s = 0.572$ for this study as this particle shape corresponds to the lowest plasticity Π value among the particles we simulated. We show the particle shape along with its correlation function and orientational distribution functions in Fig. 2.11. We have chosen three packing fractions, to calculate the correlation functions and orientational distributions:

1. $\phi = 0.547$, which is just above the liquid-plastic crystal coexistence region,

2. $\phi = 0.659$ is slightly below the plastic-crystal-crystal coexistence region,

3. $\phi = 0.715$, in the stable crystal region.

In Fig. 2.11b, we show the positional correlation functions $g(r)$ for a system of truncated cubes with $s = 0.572$ for the above mentioned three packing fractions. We clearly see that $g(r)$ shows long-range positional order for all the chosen packing fractions. However, the $g_4(r)$ shown in Fig. 2.11c, exhibit long-range orientational correlations only in the crystal regime, *i.e.,* for $\phi = 0.715$. In the plastic-crystal phase ($\phi = 0.547$ and 0.659), the orientational correlations vanish at a distance smaller than one lattice spacing as expected. With increasing packing fraction the orientational distribution of the particles in the plastic-crystal phase display long-range orientational order as shown in Fig. 2.11. The probability density in the crystal phase ($\phi = 0.715$) show the same 18 peaks as in the plastic-crystal phase. However the peaks close to the initial state show a high probability as the crystal exhibits orientational long-range order.

To conclude, the orientational distribution function of plastic crystals of hard anisotropic particles can be highly anisotropic and can be strongly peaked for specific orientations. These orientational directions depend not only on the crystal structure of the particle but also on the shape of the particle. Our results show that hard particle plastic crystals are different in nature to that of plastic crystals constituted with particles which have long-range interactions [90]. Systems with long-range interactions tend to form plastic crystals with uniform orientational distribution functions unlike the hard particles as studied. Additionally, we have shown that crystals can have many preferred orientations like plastic crystals however the probability of residing at different directions differ substantially.

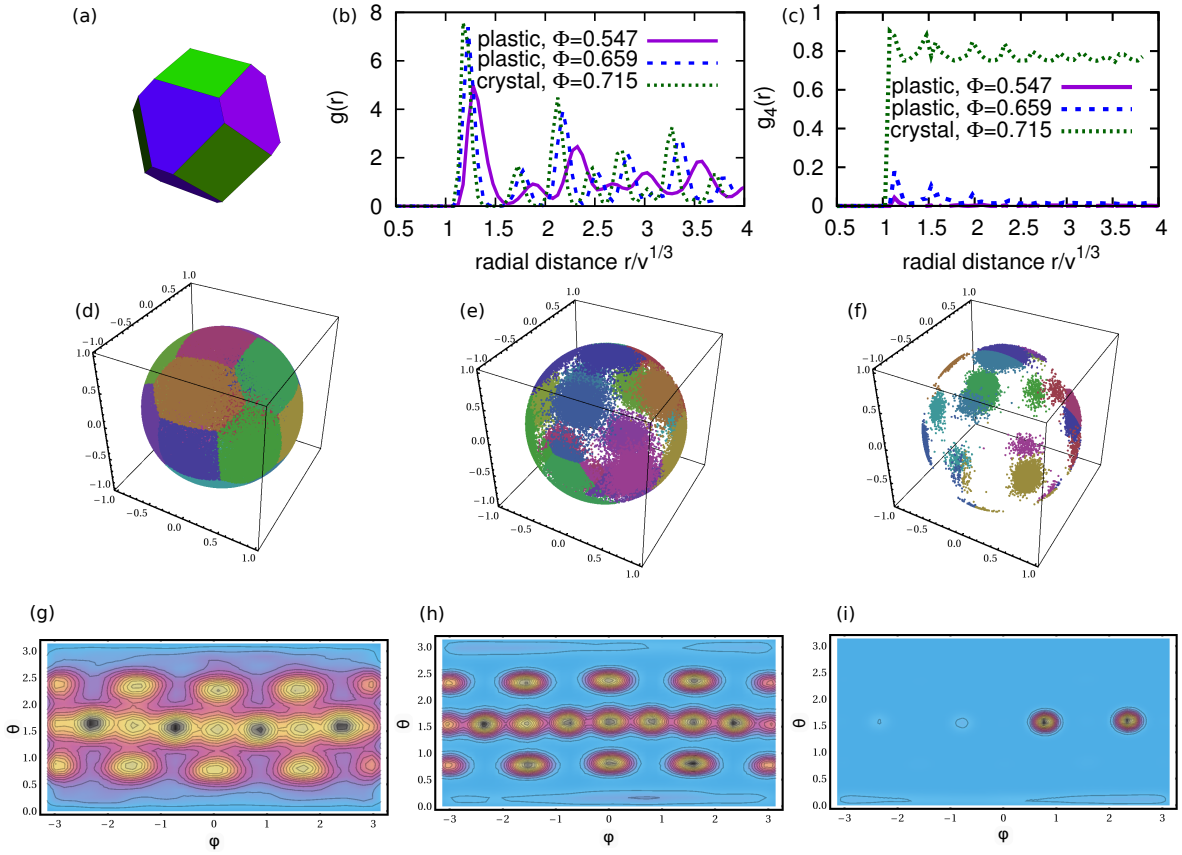

Figure 2.11: Analysis of particle shape $s = 0.572$ as a function of packing fraction. (a) Shows the particle shape. (b) and (c) show the positional and orientational correlation functions, respectively for three different packing fractions. We have chosen three packing fractions such that $\phi = 0.547$ is just above the liquid-plastic crystal coexistence region while the second one $\phi = 0.659$ is slightly below the plastic-close-packed crystal coexistence region and the third one $\phi = 0.715$ is in close-packed crystal region. In (d,e,f) we show the orientational distributions for $s = 0.572$ at $\phi = 0.547, 0.659$ and 0.715, respectively. Different clusters of orientations are colored with random colors for better illustrations. We have found that there are 18 possible directions where the particle resides. Panels (g,h,i) show the density of the orientational distribution in θ and φ representation. The color code in (g,h,i) is as follows: We have used CMYK (cyan, magenta, yellow and black) color coding to explicitly show the probability density of the orientational distributions. Low probable regions are colored cyan and high probable regions are colored black with the intermediate regions with magenta and yellow.

2.5 Conclusions

In conclusion, we have determined the full phase diagram for a family of truncated cubes, which interpolates smoothly from a cube *via* a cuboctahedron to an octahedron, using Monte Carlo simulations and free-energy calculations. The phase diagram shows a remarkable diversity in crystal structures. Of particular interest is the discovery of a fully degenerate crystal phase for a truncation parameter $s \approx 0.4$, in which diagonally interlocked sheets of particles can move with respect to each other in only one direction. The

latter system is remarkable in more than one way, since it also exhibits a fluid state and three different bulk crystals upon increasing the pressure. Both these qualities may make similarly shaped nanoparticles suitable for the creation of highly tunable functional materials, for which optical, electrical, and rheological properties vary strongly with the bulk pressure of the system. We also calculated the cubatic order parameter S_4 for truncated cubes with varying truncation level and have shown that the values of S_4 is related to the number of preferred particle orientations in the plastic-crystal phase. Additionally, we observed and studied the properties of various plastic-crystal phases observed for the truncated-cubes family. We have introduced a new parameter called plasticity parameter Π which we used to understand different plastic crystals as a function of shape. Our present results provide a solid basis for future studies of anisotropic particle systems and pave the way for a full understanding of the recent experimental studies performed on systems of nanoscopic truncated cubes.

2.6 Acknowledgments

It is a pleasure to thank Dr. Joost de Graaf for the fruitful collaboration on this project and his work on the close-packed crystal structures have been instrumental in establishing the phase diagram presented in this Chapter. I would also like to thank Prof. dr. René van Roij for fruitful discussions and for his timely suggestions.

3

Vacancies in Simple Cubic Crystals of Truncated Hard Cubes

Point defects and line defects play an important role in the stability of crystal structures. Recent simulation studies on colloidal hard cubes and hard parallel cuboids have revealed that these systems exhibit roughly three orders of magnitude more vacancies than the simple hard-sphere systems. In this chapter we extend the equilibrium vacancy concentration calculations to truncated cubes. Our results show that at a given packing fraction ϕ the number of vacancies increases with increasing truncation. Using a simple cell theory we show that the increase in vacancy concentration is due to a gain in orientational entropy.

3.1 Introduction

Colloidal crystals are known to exhibit vacancies, interstitials and dislocations. Point defects are the most common of these. Recent studies [79, 80] have shown that colloidal hard cubes and hard parallel cuboids exhibit a large number of vacancies close to the fluid-crystal coexistence region. These studies have shown that the above mentioned systems can have vacancy concentrations as high as three orders of magnitude more than the vacancy concentration of the well-studied hard-sphere systems [94, 95]. Apart from the theoretical interests to compute the equilibrium vacancy concentrations for different colloidal systems, it is also interesting to study systems with vacancy-rich phases to design smart materials with self-healing properties. Also, scientists around the world are working with various crystal structures which have lattice constants comparable to that of the wavelength of visible light to create photonic materials. Since truncated cubes can be synthesized at various sizes [16, 36, 37] and the fact that the equilibrium number of vacancies can influence the nature of photonic states, it is interesting to study the equilibrium vacancy concentrations of these truncated cubes.

Here we use an Einstein integration method with slight modifications, following Ref. [79], to compute the free energies of crystals with vacancies. The modifications are mainly done to the confining potential which will be explained in the Methods section in detail. We compute the free energies of the truncated cubes at a fixed packing fraction $\phi = 0.56$ with varying shape parameter s as defined in Eq. 2.1. Our results show that the equilibrium vacancy concentration increases with increasing shape parameter s for a given packing fraction close to the coexistence densities. In addition, we use a simple cell theory to explain the increase in vacancy concentration at fixed packing fraction. Our results show that the increase in vacancy concentration with truncation of a cube is due to a gain in orientational entropy.

3.2 Methods

3.2.1 Free Energy of a Solid with Vacancies

We calculate the free energy of a solid phase at a fixed vacancy concentration $\alpha = (N_L - N)/N_L$, with N the number of particles and N_L the number of lattice sites. We use the Einstein integration method as explained in Chapter 2 to determine the free energy of a solid. The main difference in the Einstein integration method to compute the free energy of the solid with and without vacancies is the confining potential. While calculating the free energy of a system with vacancies we attach the particles to their nearest lattice site rather than to a specific lattice site. To achieve this Eq. 2.7 in Chapter 2 is modified to

$$\beta U_{\text{Einst}}(\lambda) = \quad \lambda \sum_{i=1}^{N} [(\mathbf{r}_i - \mathbf{r}^0(\mathbf{r}_i))^2 / v_p^{2/3} + (\sin^2 \psi_{ia} + \sin^2 \psi_{ib})], \tag{3.1}$$

where $\mathbf{r}^0(\mathbf{r}_i)$ is the position of the lattice site nearest to the current position $\mathbf{r}_i$ of particle. The dimensionless free energy per particle $f_{\text{Einst}}^{\text{vac}} = \frac{F_{\text{Einst}}^{Vac}}{N k_{\text{B}} T}$ of a non-interacting Einstein

crystal with vacancies is given by:

$$f_{\mathrm{Einst}}^{\mathrm{vac}}(\lambda_{\max}) = f_{\mathrm{Einst}}(\lambda_{\max}) + f_{\mathrm{rot}}(\lambda_{\max}) + f_{\mathrm{comb}}, \tag{3.2}$$

where f_{Einst} and f_{rot} are the translational and rotational free energies of an ideal Einstein crystal, while f_{comb} is the combinatorial entropy associated with placing N particles on N_L lattice sites. All terms read as follows:

$$f_{\mathrm{Einst}}(\lambda_{\max}) = -\frac{3(N-1)}{2N}\log\left(\frac{\pi}{\lambda_{\max}}\right) + \log\left(\frac{\Lambda_t^3\Lambda_r}{v_p}\right), \tag{3.3}$$

$$f_{\mathrm{rot}}(\lambda_{\max}) = -\frac{1}{N}\log\left\{\frac{1}{8\pi^2}\int \mathrm{d}\theta\sin(\theta)\mathrm{d}\phi\mathrm{d}\chi \times \exp\left[-\frac{\lambda_{\max}}{k_BT}(\sin^2\psi_{ia} + \sin^2\psi_{ib})\right]\right\}, \tag{3.4}$$

and

$$f_{\mathrm{comb}} = -\frac{1}{N}\log\left(\frac{N_L!}{N!(N_L-N)!}\right). \tag{3.5}$$

We would like to point out that the free-energy calculations are done without fixing the center of mass of the whole system unlike the traditional Einstein integration method [96]. To account for this change we introduce a Monte Carlo move that collectively displaces the entire system which allows to sample the entire phase space of the center of mass of the system. In addition we have also implemented a Monte Carlo move in which a particle may hop onto an adjacent lattice site in order to equilibrate faster the vacancy distribution in the crystal. Both, the Monte Carlo move to translate the entire system and the particle hopping move are attempted with 50% probability in every Monte Carlo sweep (MCS), where a MCS consist of $N/2$ translational and $N/2$ rotational moves. For more details about the implementation of the free-energy calculations, we refer to the methods section of Ref. [79]. We used $N_L = 15^3 = 3,375$ lattice sites for the free-energy calculations of a simple cubic (SC) crystal phase of truncated hard cubes with shape parameter $s = 0.05$, 0.15, and 0.25 and packing fraction $\phi = 0.56$ and varying vacancy concentrations $\alpha = (N_L - N)/N_L$ as described above.

In Chapter 2, we presented the phase diagram of truncated cubes in Fig. 2.6. In this phase diagram we did not take into account the shift in coexisting densities due to the presence of vacancies in the simple cubic phase. We feel justified in this omission, since the presence of vacancies lead to a minute change in the location of the phase boundaries for the SC-fluid coexistence densities as was already shown for hard cubes by Smallenburg *et al.* [79].

3.3 Results

We have used the above mentioned free-energy method to determine vacancies in the vacancy-rich SC phase for $s \in [0.00, 0.374]$. We define the vacancy concentration α as the fraction of unoccupied sites in the SC crystal lattice. To determine the equilibrium

vacancy concentration, we calculated the dimensionless free energy $f(\alpha)$ as a function of α for $s = 0.05$, $s = 0.15$, and $s = 0.25$, at packing fraction $\phi = 0.56$. The free energy as a function of vacancy concentration α is shown in Fig. 3.1 for several levels of truncation s along with the particle shapes. The $s = 0$ (perfect cubes) data is obtained from Ref. [79]. For each shape we have indicated the equilibrium vacancy concentration with a vertical red dotted line. Fig. 3.1 shows that the minimum in the free energy shifts to higher vacancy concentrations upon increasing the level of truncation s at a fixed packing fraction. This result is surprising and is in contrast to the behavior observed for parallel cuboids [80], which exhibit a constant vacancy concentration at $\phi = 0.5$ and 0.55 with increasing roundness. It is known already from Ref. [79] that the vacancies are delocalized along rows in the crystal lattice, since the particles can easily move with respect to each other and fill up the vacated space.

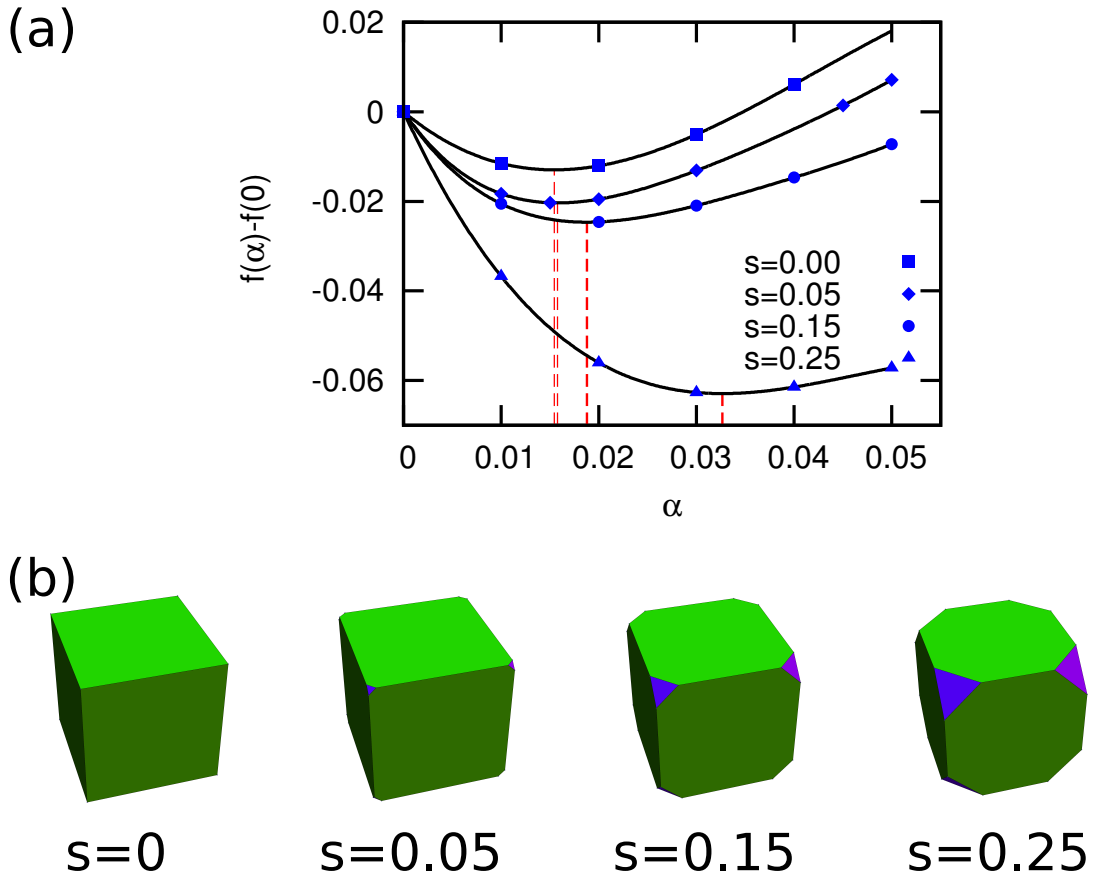

Figure 3.1: (a): Free-energy differences per particle $f(\alpha) - f(0) = \frac{F(\alpha)-F(0)}{Nk_BT}$ between a system with vacancies $f(\alpha)$ and the one without vacancies $f(0)$ as a function of the fraction of vacancies α for truncations $s = 0$, $s = 0.05$, $s = 0.15$, and $s = 0.25$ at packing fraction $\phi = 0.56$. For $s = 0$ we took the results from Ref. [79]. The actual data points are plotted in thick blue, the black line is a polynomial fit to the data. The dashed (red) vertical lines show the location of the minimum in the free energy, *i.e.*, the equilibrium vacancy concentration α. (b): All the particle shapes considered for the free-energy calculations along with their truncation values are shown.

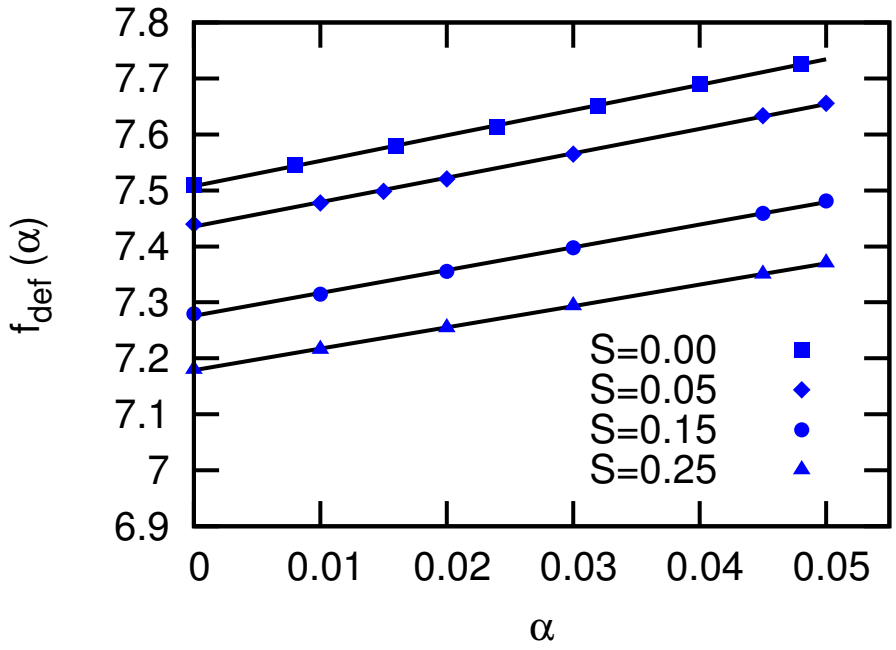

Figure 3.2: The reduced free energy per particle $f_{\rm def}(\alpha)$ as a function of vacancy concentration α for a simple cubic crystal phase of truncated cubes with shape parameter $s = 0$, 0.05, 0.15, and 0.25 and packing fraction $\phi = 0.56$. $f_{\rm def}(\alpha)$ does not account for the combinatorial entropy, *i.e.*, $f_{\rm def}(\alpha) = f\,(\alpha) - f_{\rm comb}(\alpha)$.

In Fig. 3.2, we present the dimensionless free energy per particle $f_{\rm def}$ as a function of α without taking into account the combinatorial entropy, *i.e.*, $f_{\rm def}(\alpha) = f(\alpha) - f_{\rm comb}(\alpha)$. In accordance with the observations of Ref. [79], $f_{\rm def}$ *vs* α in Fig. 3.2 shows a linear behavior suggesting that the vacancies are only weakly interacting. Assuming the vacancies to be non-interacting, which allows one to write the free energy of a crystal phase as

$$f_{\rm def}(\alpha) = f(0) - \alpha f_1 \tag{3.6}$$

where $f(0)$ is the dimensionless free energy per particle of a crystal with no vacancies and f_1 is the reduced free-energy cost to create a single vacancy (without the combinatorial component). Fitting the results as displayed in Fig. 3.2 with Eq. 3.6, we determined f_1 for truncated cubes as a function of shape parameter s. The results are tabulated in Table 3.1. Surprisingly, we find that the free-energy cost to create a vacancy f_1 decreases with increasing s at packing fraction $\phi = 0.56$. Hence, we find that the equilibrium vacancy concentration increases with particle truncation s.

3.4 Cell Theory Calculations

In order to explain our free-energy calculations and observations, we estimate the free-energy cost to create a single vacancy at a specific lattice point using a simple cell

Table 3.1: The dimensionless free energy per particle for a simple cubic crystal of truncated cubes with shape parameter $s = 0$, 0.05, 0.15, and 0.25 and packing fraction $\phi = 0.56$. From left to right we specify the truncation parameter s, the packing fraction of the densest crystal structure ϕ_{cp}, the dimensionless free energy for a system with zero vacancies $f(0)$, the free-energy cost to create a single vacancy f_1 (without the combinatorial contribution) as obtained by Monte Carlo simulations and free-energy calculations, f_1 obtained from cell theory for parallel truncated cubes f_1^{cell}, and as obtained from cell theory for freely rotating cubes $f_1^{\mathrm{cell,or}}$.

		Simulations		Cell theory	
s	ϕ_{cp}	$f(0)$	f_1	f_1^{cell}	$f_1^{\mathrm{cell,or}}$
0.00	1.00000	7.5077	4.52640	4.63638	4.63638
0.05	0.99987	7.4354	4.36892	4.63699	4.48311
0.15	0.99649	7.2762	4.06024	4.65291	4.16535
0.25	0.98370	7.1788	3.81633	4.71465	3.85161

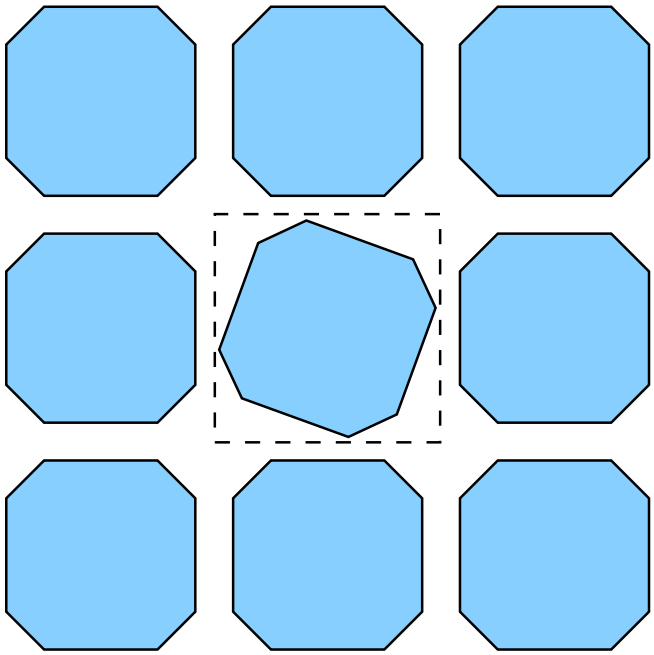

Figure 3.3: Depiction of the insertion in a two-dimensional (2D) simple square lattice of a rotated truncated square. The three dimensional (3D) case of insertion of a truncated cube into a simple cubic crystal is analogous.

theory. We first ignore the orientational degrees of freedom of the cubes and consider N parallel truncated cubes in a simple cubic crystal phase with volume V. In addition, we assume the particles to be confined in Wigner-Seitz (WS) cells centered around the ideal lattice positions. In a simple cubic crystal phase with a lattice constant a, the particles are confined to cubic cells with a volume $v = a^3 = V/N$ as illustrated in Fig. 3.3. At close packing the volume of the cubic cell is given by $v_{\mathrm{cp}} = \sigma^3$ with σ the side length of the outscribed cube of the particle. We will use these results in the following calculation.

To determine the free-energy change of a crystal due to the creation of a vacancy, one can also consider the change in free energy by removing a single vacancy at a specific lattice point using the particle insertion method [95]. To this end, we consider a crystal containing a single vacancy and determine the free volume that is available for the center-of-mass of a particle in the WS cell surrounding that vacancy. It is straightforward to see that the free volume reads

$$v_{\text{free}} = (a - \sigma)^3. \tag{3.7}$$

Using the packing fraction $\phi = v_p N/V$ and the packing fraction at close packing ϕ_{cp}, we find that the reduced free-energy cost f_1 to create a vacancy reads

$$f_1^{\text{cell}} = -\log\left(\frac{v_p}{\Lambda_t^3}\right) - 3\log\left(\frac{1}{\phi^{1/3}} - \frac{1}{\phi_{\text{cp}}^{1/3}}\right), \tag{3.8}$$

where Λ_t is the thermal wavelength of the system. We note that the packing fraction ϕ_{cp} at close-packing decreases upon increasing the truncation parameter s from zero in the (D)SC phase. In Table 3.1, we list this maximum packing fraction ϕ_{cp} as well as the reduced free-energy cost to create a vacancy f_1 as obtained from our cell theory (Eq.3.8). We clearly observe that f_1 as obtained from cell theory for non-rotating cubes increases with truncation in contrast with our free-energy calculations using Monte-Carlo simulations. Our model is therefore oversimplified.

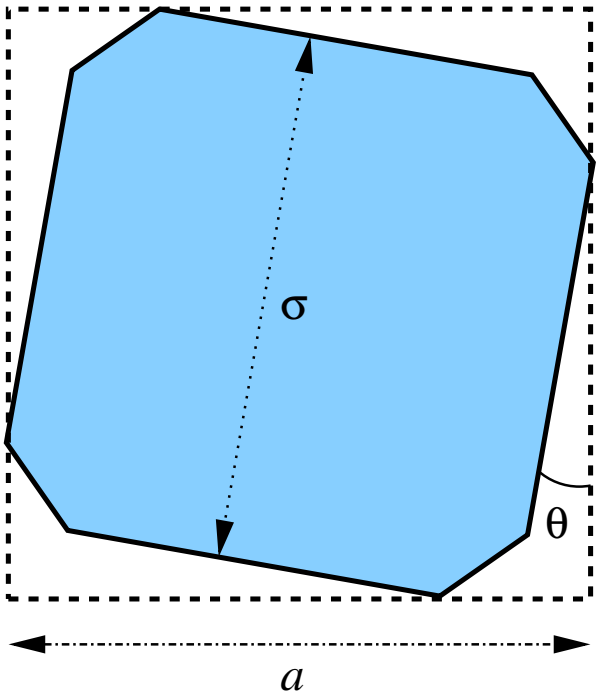

Figure 3.4: The maximal angle θ that a truncated square can rotate in the center of its Wigner-Seitz (WS) cell. The side length of the WS cell is given by a, the diameter of the outscribed square by σ.

Let us now consider truncated cubes that are allowed to rotate. For a visual representation of the cell-theory method we present two-dimensional (2D) schematic pictures

in Figs. 3.3 and 3.4. If we assume the rotations to be small and take only into account rotations around either the x-, y-, or z-axis, the maximal angle $\theta(s)$ that a truncated cube in the center of the WS cell can rotate is approximately

$$\theta(s) = \frac{a - \sigma}{(1 - s)\sigma}. \tag{3.9}$$

This is easily derived with the help of Fig. 3.4. The change in reduced orientational free energy of a truncated cube in a WS cell *w.r.t* that of a cube ($s = 0$) is

$$\Delta f_{\rm or}(s) = \log \left[\frac{\theta(0)}{\theta(s)}\right]^3 \approx 3 \log (1 - s), \tag{3.10}$$

using our model. The reduced free-energy cost f_1 to create a vacancy in a simple cubic crystal of freely rotating truncated cubes with shape parameter s is therefore approximated by

$$f_1^{\rm cell,or}(s) = -\log(\frac{v_p}{\Lambda_t^3 \Lambda_r}) - 3 \log(\frac{1}{\phi^{1/3}} - \frac{1}{\phi_{\rm cp}^{1/3}}) + 3 \log (1 - s). \tag{3.11}$$

Table 3.1 displays the results, which show remarkably good agreement with the 'exact' f_1 that was obtained using Monte Carlo simulations and free-energy calculations. The decrease in the free-energy cost f_1 to create a vacancy with increasing s is therefore due to an increase in orientational entropy, and the increased rotational entropy consequently explains the increase in the vacancy concentration at fixed packing fraction ϕ. More importantly, our results show that a simple cell theory can give accurate predictions for the equilibrium vacancy concentration for truncated cubes, and can perhaps be used as a predictive tool for a wider class of particle shapes. However, one should notice that our cell theory is oversimplified and we caution the reader to extend the results to other systems with care.

3.5 Conclusions

To conclude, we have determined the free energies of truncated cubes as a function of vacancy concentration using a modified Einstein integration method. From our calculations we found that the equilibrium vacancy concentration of truncated cubes increase with increasing truncation at a fixed packing fraction $\phi = 0.56$. Using simple cell theory calculations we have shown that the increase in vacancy concentrations with truncation s is due to the increase in orientational entropy with truncation. It would be interesting to study in more detail the effect of particle shape on the equilibrium vacancy concentration for other colloidal systems which form simple cubic crystal structures.

Finally, we note that the cell theory model is oversimplified. As it is known that the vacancies are delocalized for cubes and truncated cubes one has to take that into account to perform cell theory calculations. Instead of taking one particle in a cell one could take a row of truncated cubes and use insertion moves to determine f_1. These considerations will be implemented in future work.

3.6 Acknowledgments

It is a pleasure to thank Dr. Frank Smallenburg for providing the vacancy concentration data of hard cubes used to create Fig. 3.1 and for useful discussions. I would also like to thank Prof. René van Roij for his cell theory calculations presented in this Chapter.

4

Phase Diagram of Colloidal Hard Superballs: from Cubes via Spheres to Octahedra

The formation of a wide variety of fascinating crystal and liquid-crystal phases is accomplished by entropy alone. A better understanding of these entropy-driven phase transitions of hard anisotropic particles will shed light on the self-assembly of nanoparticles, however, there are still many open questions in this regard. In this work, we use Monte Carlo simulations and free-energy calculations to determine the phase diagram of colloidal hard superballs, of which the shape interpolates between cubes and octahedra via spheres. We found not only a stable face-centered cubic (fcc) plastic-crystal phase for near-spherical particles, but also a stable body-centered cubic (bcc) plastic crystal close to the octahedron shape. Moreover, coexistence of these two plastic crystals is observed with a substantial density gap. The plastic fcc and bcc crystals are, however, both unstable in the cube and octahedron limit, suggesting that the low asphericity ratio of the superballs in combination with local curvature, i.e. rounded corners and curved faces, of superballs play an important role in stabilizing the rotator phases. In addition, we observe a two-step melting phenomenon for hard octahedra, in which the Minkowski crystal melts into a metastable bcc plastic crystal before melting into the fluid phase.

4.1 Introduction

Recent breakthroughs in particle synthesis have resulted in a spectacular variety of anisotropic nanoparticles such as cubes, octapods, tetrapods, octahedra, ice cones, *etc.* [5]. A natural starting point to study the self-assembled structures of these colloidal building blocks is to view them as hard particles [5]. Not only can these hard-particle models be used to predict properties of suitable experimental systems, but such models also provide a stepping stone towards systems where soft interactions play a role [14, 60]. Moreover, the analysis of hard particles is of fundamental relevance and raises problems that influence fields as diverse as (soft) condensed matter, [5, 78, 97, 98] mathematics, [98, 99] and computer science [100]. In this light the concurrent boom in simulation studies of hard anisotropic particles is not surprising [78, 79, 81, 98, 99, 101–107].

The best-known hard-particle system consists of hard spheres, which freeze into close-packed hexagonal (cph) crystal structures, [100] of which the ABC-stacked cph crystal, better known as the face-centered cubic (fcc) crystal phase, is thermodynamically stable [108]. Hard anisotropic particles can form liquid-crystalline equilibrium states if they are sufficiently rod- or disc-like, [104, 107] but particles with shapes that are close-to-sphere tend to order into plastic-crystal phases, also known as rotator phases [105–107]. In fact, simple guidelines were recently proposed to predict the plastic- and liquid-crystal formation only on the basis of rotational symmetry and shape anisotropy of hard polyhedra [78]. In this Chapter we will take a different approach, based on free-energy calculations, and address the question whether and to what extent rounding the corners and faces of polyhedral particles affects the phase behavior. Such curvature effects are of direct relevance to experimental systems, in which sterically and charged stabilized particles can often *not* be considered as perfectly flat-faced and sharp-edged [17]. For instance, recent experiments on nanocube assemblies show a continuous phase transformation between simple cubic and rhombohedral phases by increasing the ligand thickness and hence the particle sphericity [14]. In this work we construct an accurate phase diagram of these colloidal hard superballs between the cube and the octahedra and thereby try to understand the role of curvature in the formation of plastic-crystal phases at intermediate pressures.

A superball is defined by the inequality

$$|x|^{2q} + |y|^{2q} + |z|^{2q} \leq 1, \tag{4.1}$$

where x, y and z are scaled Cartesian coordinates with q the shape parameter, and we use radius a of the particle as our unit of length. In this work we limit $q \in [0.5, \infty)$ where the shape of the superball interpolates smoothly between two Platonic solids, namely the octahedron ($q = 0.5$) and the cube ($q = \infty$) via the sphere ($q = 1$) as shown in Fig. 4.1. To quantify curvature of these particles we use asphericity A which is defined as

$$A = 1 - \frac{\pi^{1/3} \left[6v(q)\right]^{2/3}}{S(q)}, \tag{4.2}$$

where $S(q)$ is the surface area of the particle. The volume of the superball $v(q)$ is given by

$$\begin{aligned} v(q) &= 8a^3 \int_0^1 \int_0^{(1-x^{2q})^{1/2q}} (1 - x^{2q} - y^{2q})^{1/2q} \mathrm{d}\, y \, \mathrm{d}\, x \\ &= \frac{8a^3 \left[\Gamma\left(1 + 1/2q\right)\right]^3}{\Gamma\left(1 + 3/2q\right)}, \end{aligned} \tag{4.3}$$

where $a = 1$ is the radius of the particle. This asphericity definition is similar to the one used in Refs. [109, 110]. According to Eq. 4.2, we have $A = 0$ for a sphere and $A > 0$ for nonspherical objects. For the superball the asphericity increases smoothly and substantially by letting q deviate from $q = 1$. The asphericity of superballs as a function of $1/q$ is shown in Fig. 4.1. By determining the phase diagram of these superballs as a function of q, we discovered a thermodynamically stable body-centered cubic (bcc) plastic-crystal phase for octahedron-like superballs. A bcc rotator phase has also recently been reported in simulations of truncated and perfect octahedra parallel to our work [67] and for truncated cubes in Ref. [49] and Chapter 2. However, the thermodynamic stability of the bcc rotator phase using free-energy calculations has not been examined in Ref. [67]. Moreover, we demonstrate using free-energy calculations that bcc and fcc plastic-crystal phases are unstable for hard octahedra and hard cubes, respectively. Therefore in the case of superballs defined in the interval $q \in [0.5, \infty]$, rounded faces and edges may play an important role in stabilizing rotator phases, while flat faces tend to stabilize crystals.

The remainder of this Chapter is organized as follows: We first briefly discuss the models and the simulation methods. Subsequently, we present the phase behavior of the exact octahedra $q = 0.5$ in detail. We then present the phase diagram of the octahedron-like $q \in [0.5, 1)$ and cube-like superballs $q \in (1, \infty)$. Finally we move on to draw conclusions on the phase behavior of superballs as obtained from our free-energy calculations.

4.2 Model, Methods and Simulations

Following Refs. [72, 101], we first calculate the close-packed structures for systems of hard superballs $q \in [0.5, \infty)$. We use these close-packed structures to perform NPT Monte Carlo simulations with variable box shape at fixed pressure P, number of particles N, and temperature T to determine the equation of state (EOS) of the crystal phase upon expanding the system. At the same time we also compress dilute superball systems using NPT simulations and determine the equations of state upon compression. We then calculate the free energy for the various phases observed in our NPT simulations using the Einstein integration method as explained in Section 2.3.2 of Chapter 2. We then use thermodynamic integration and common-tangent constructions to determine the stability and the phase boundaries for the various phases.

In order to detect the overlaps between superballs we employ the algorithm described in Ref. [77]. This algorithm is unstable for superballs with large curvatures i.e., for $q < 0.7$ and $q > 3$. To avoid the stability problems in the algorithm we simulated perfect faceted octahedra using the separating axis theorem [84]. The phase diagram of hard cubes which is already known is taken from Ref. [79] to construct the complete phase diagram.

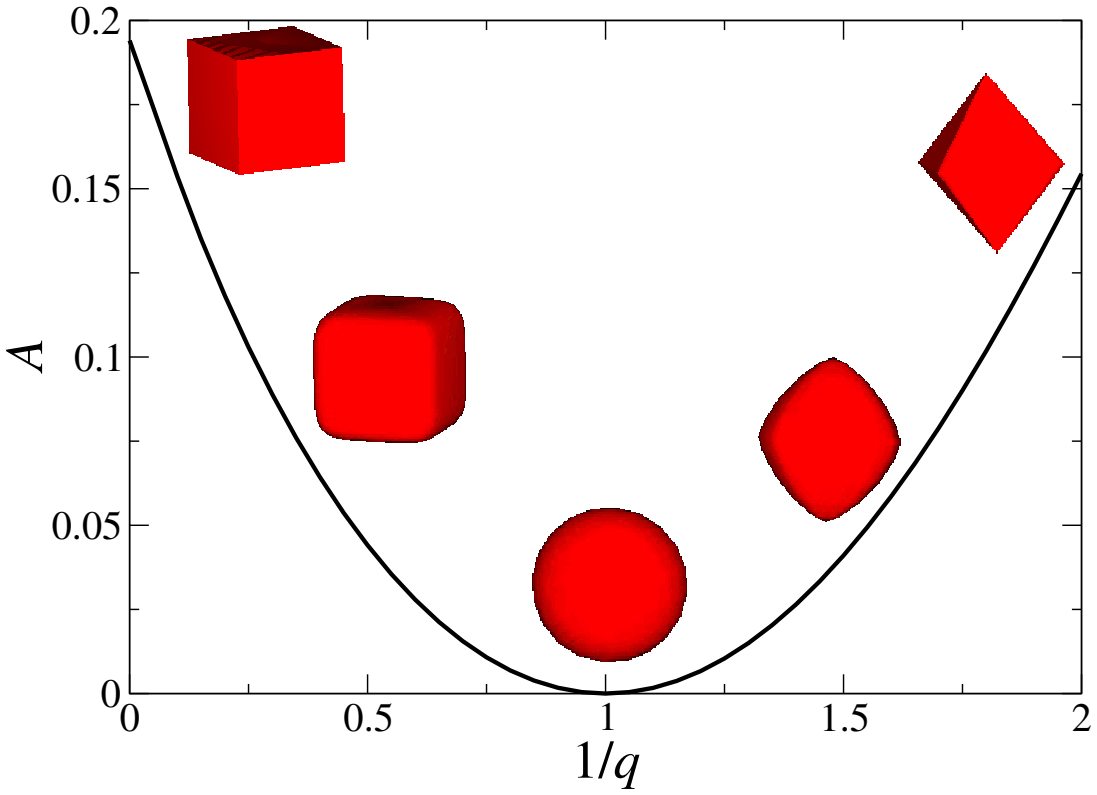

Figure 4.1: The asphericity A as a function of the shape parameter q as defined in Eq. 4.1, where the shape of superballs interpolates between octahedra ($q = 0.5$) and cubes ($q = \infty$) via spheres ($q = 1$).

4.3 Results and Discussion

4.3.1 The Phase Behavior of Hard Octahedra

We first determined the equations of state for octahedra using the floppy box NPT Monte Carlo simulations [72]. When we compressed a system of hard octahedra from a dilute fluid phase, we did not observe the spontaneous formation of a crystal phase in our simulation box within our simulation time. When we expanded the Minkowski crystal, which is the close-packed structure of octahedra [48], in NPT MC simulations by decreasing the pressure quasi-statically, the system melts into a bcc plastic-crystal phase. The equations of state obtained during the compression and expansion runs are shown in Fig. 4.2a. We used $N = 1458$ particles in our NPT MC simulations to obtain the equations of state. These equations of state for various phases are used to determine the free energy as a function of packing fraction (or equivalently density) using thermodynamic integration as explained in Section 2.3.2 in Chapter 2.

Typical simulation snapshots of the fluid, rotator and crystal phases in the NPT Monte Carlo simulations of octahedra are shown in Fig. 4.2 c,d, and e. The fluid and the bcc crystal phase configurations in Fig. 4.2 c,d, respectively, contain $N = 128$ particles while the Minkowski crystal displayed in Fig. 4.2e contains $N = 250$ particles. For the sake of visual clarity we have chosen smaller system sizes to display. The particles in

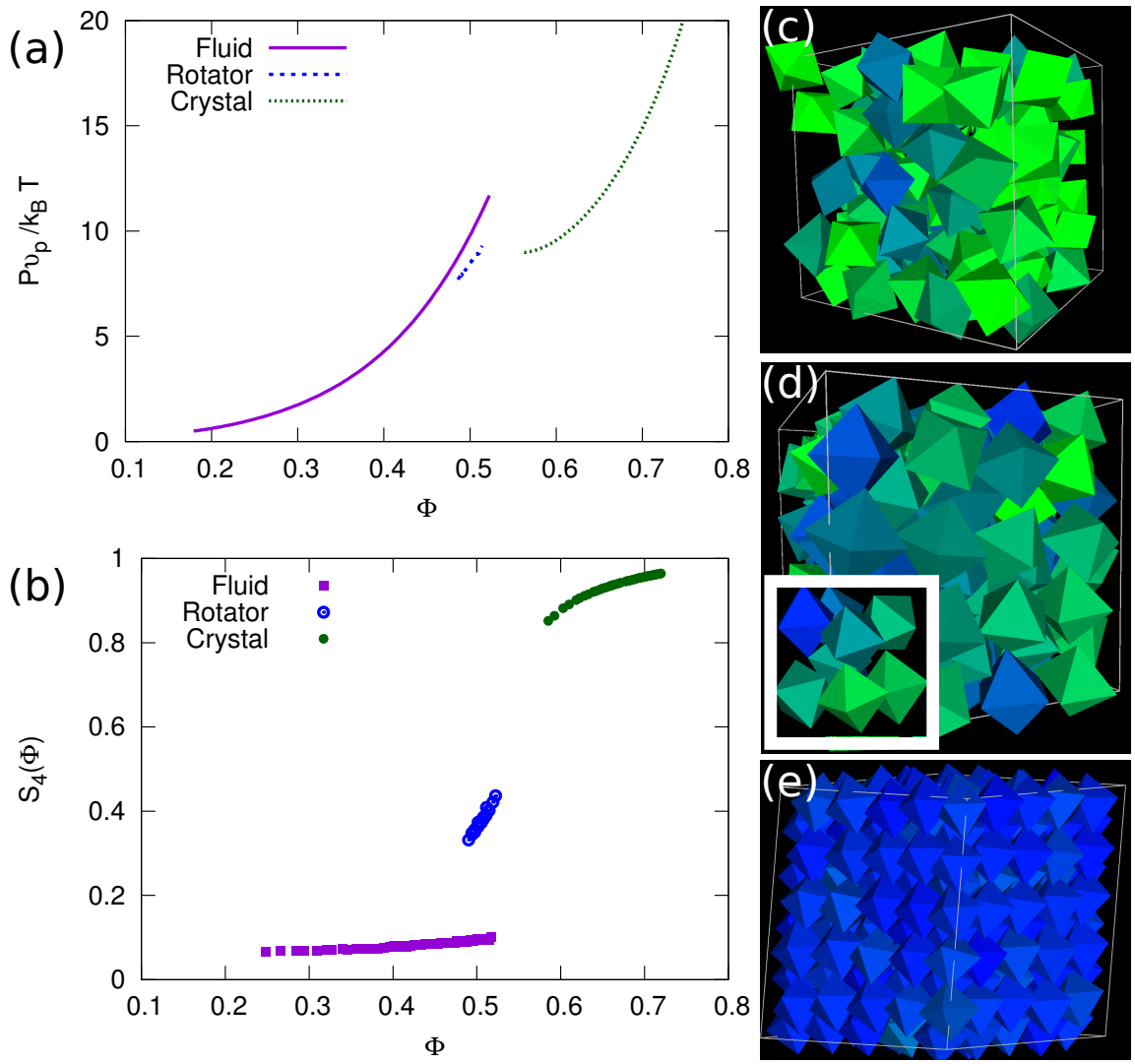

Figure 4.2: (a): The equation of state for hard octahedra obtained from our NPT Monte Carlo simulations. The reduced pressure Pv_p/k_BT is plotted as a function of packing fraction ϕ. Here v_p is the volume of the particle. The equation of state (EOS) for the crystal branch is obtained by melting from an ideal Minkowski lattice, which is the close-packed structure for octahedra. The fluid branch of the EOS is obtained by compressing the dilute fluid. (b): The cubatic order parameter $S_4(\phi)$ is plotted as a function of ϕ. (c,d,e): Typical simulation snapshots of hard octahedra in the three different phases observed in the NPT simulations. (c) fluid, (d) bcc rotator phase and (e) crystal phase. In the inset of (d) we show the unit cell of a bcc rotator phase. The color of the particle is based on their orientation with respect to the particles in the close-packed crystal. Particles in an ideal Minkowski lattice will have dark blue color according to our coloring scheme and green when the orientations deviate significantly from the ideal orientation.

the snapshots are colored depending on their orientation with respect to the particles in the ideal close-packed Minkowski crystal. In the close-packed Minkowski crystal phase all octahedra are colored blue as their orientations are arrested. In the fluid and the bcc

rotator phase one can see that the orientations of the particles are random and so are their colors.

In order to quantify the orientational order as a function of packing fraction $\phi = \frac{Nv_p}{V}$, with v_p the volume of a particle, for different phases, we calculate the cubatic order parameter S_4 defined in Eq. 2.2 of Chapter 2. We plotted $S_4(\phi)$ as a function of ϕ in Fig. 4.2 b. We observe that the orientational order is negligible ($S_4 \leq 0.1$) in the fluid state, but has a finite value in the bcc rotator phase. The $S_4(\phi)$ in the bcc rotator phase increases linearly with increasing ϕ. In the Minkowski crystal the cubatic order $S_4(\phi) \approx 1$ suggesting a fully orientationally ordered system as expected for a crystal phase.

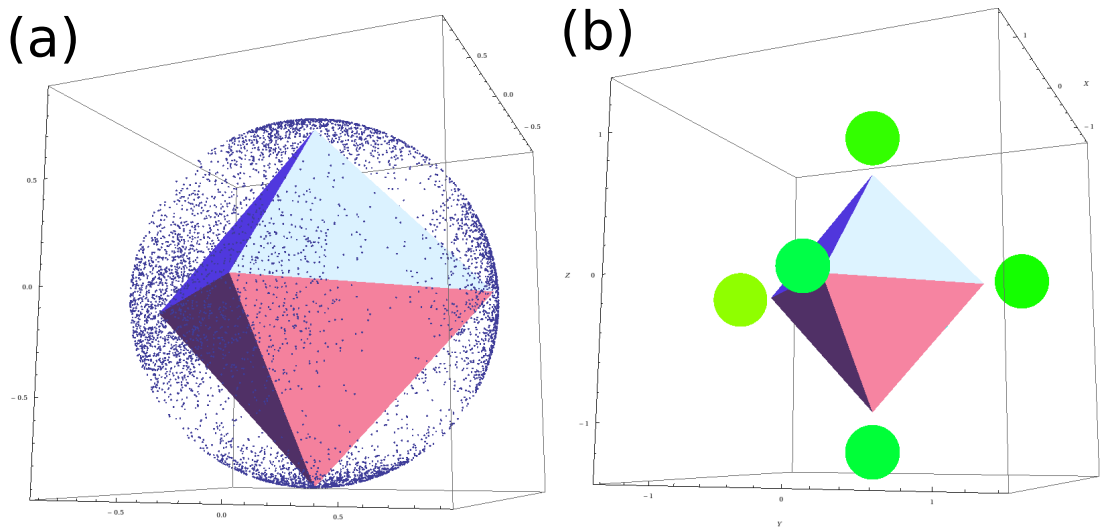

Figure 4.3: Orientations of octahedra in the bcc rotator phase: (a) Orientations of octahedra projected on the surface of a unit sphere in a bcc rotator phase and (b) the orientational distributions are clustered based on their orientations. We have found six most probable directions which are indicated with a colored sphere. The color of the sphere indicates the probability of finding the particle with that orientations. We have used 20 simulation snapshots each containing 250 particles at packing fraction $\phi = 0.526$ to obtain these plots.

In order to study in more detail the orientations of the octahedra in the bcc rotator phase, we present in Fig. 4.3 the orientations of the octahedra in the bcc phase projected onto the surface of a unit sphere. We clearly observe that the orientations of the octahedra are not homogeneous in the plastic-crystal phase and that there are preferred orientations. We used a cluster algorithm in Mathematica to determine the most probable orientations of the octahedra and have shown them in Fig. 4.3 b. The most probable orientations of octahedra in the bcc rotator phase are the symmetry orientations that leave the octahedron invariant under rotation. In other words these orientations indicate the cubatic symmetry of the particle. From these observations we conclude that the octahedra in the plastic-bcc-rotator phase jump from one symmetry orientation to the other rather than that they rotate smoothly around their centers of mass. We also observed that with increasing packing fraction the orientations of the octahedra get more and more arrested and at high enough density the system undergoes a first-order phase transition to a Minkowski crystal phase where particle orientations are largely frozen in.

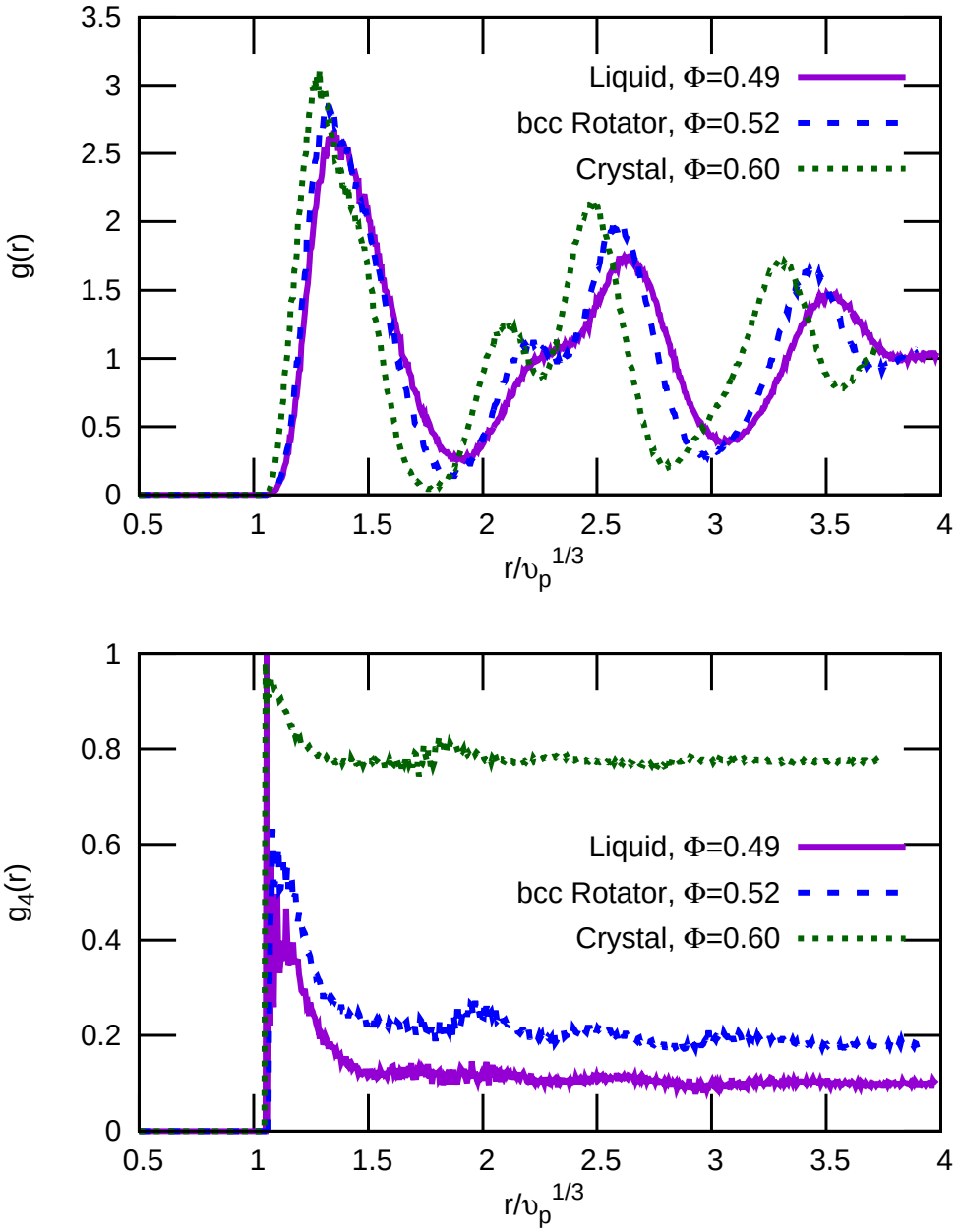

Figure 4.4: Correlation functions for octahedra. (a): Positional correlation functions $g(r)$ for all the three different phases observed for octahedra close to the coexisting densities. (b): Orientational correlation functions $g_4(r)$ for the same densities and phases as in Fig. 4.4a. At large r, $g_4(r) \approx S_4(r)^2$ unlike the $g(r)$ which goes to one. Here r is the radial distance and v_p is the volume of the particle which is set to unity.

We computed positional and orientational correlation functions close to the coexisting densities of the three different phases of the octahedra. The positional correlation function $g(r)$ and the orientational correlation function $g_4(r)$ are shown in Fig 4.4 a and b, respectively. The $g(r)$ calculated for a fluid close to freezing, a rotator bcc phase close to melting and the crystal phase show almost similar behavior in all the three phases. However the orientational correlation function $g_4(r)$ shows some interesting features. The

$g_4(r)$ generally goes to a plateau at large r which is proportional to S_4^2, with S_4 the cubatic orientational order in the bulk. Here $g_4(r)$ shows that the fluid and bcc rotator phase has weak orientational correlations with respect to that of the crystal phase. The orientational correlation functions in the fluid and bcc phase decay rapidly at short distance r, showing that the neighboring particle orientations are not coupled to each other. However the bcc phase exhibit slightly more orientational order compared to the fluid phase at large r. In the crystal phase the orientational correlations appear to be long range, as expected for the system sizes we considered.

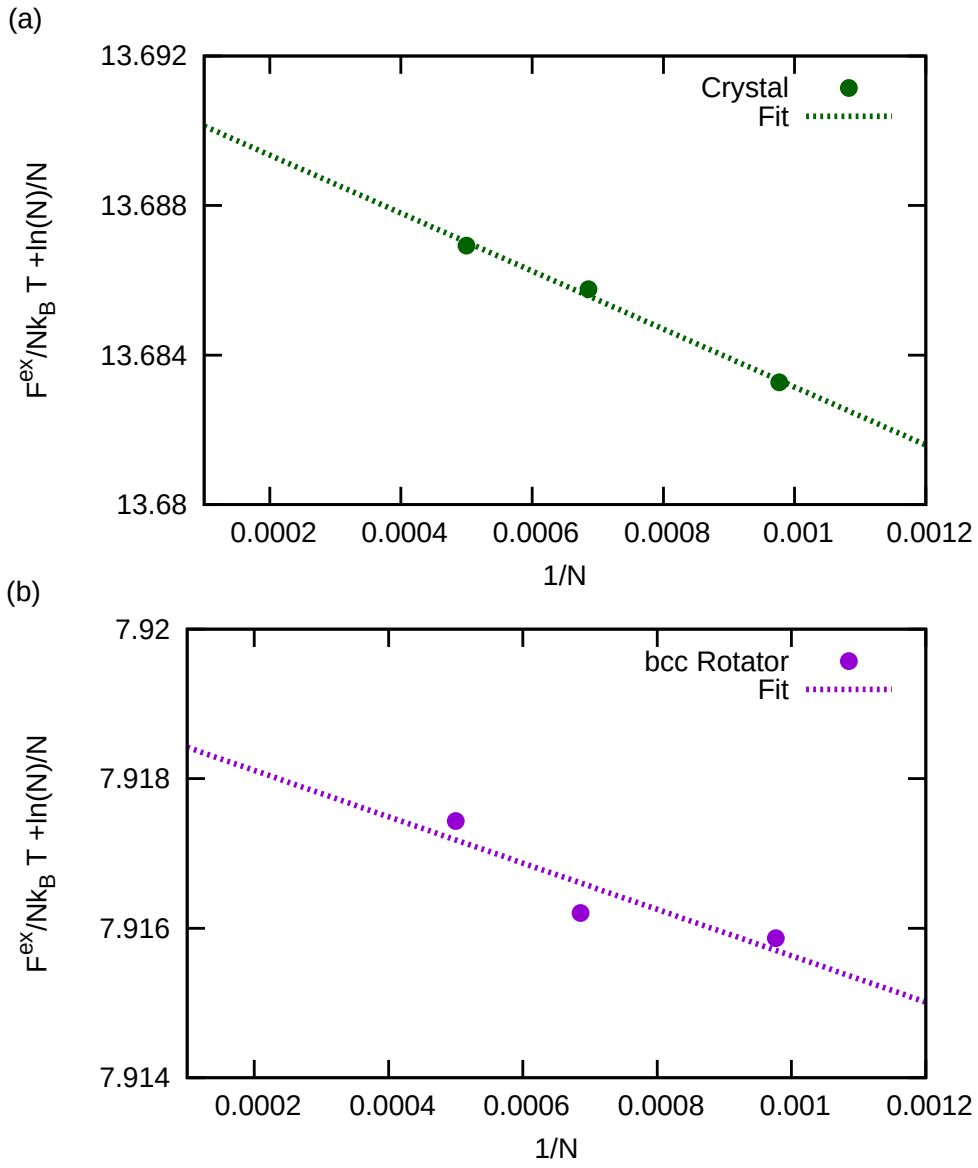

Figure 4.5: $F^{\text{ex}}/Nk_BT + \ln N/N$ as a function of $1/N$ for a system of hard octahedra in a Minkowski crystal (a) and in a bcc plastic-crystal phase (b) at packing fraction $\phi = 0.71052$ and 0.5, respectively.

Finally, we calculated the free energies for all the three phases to determine the phase boundaries for hard octahedra. We used the Einstein integration method to calculate the free energies for the crystal phases and the Widom insertion method [96] for the fluid phase. For more details regarding the methods for calculating free energies for different phases see Section 2.3.2 of Chapter 2. To eliminate the finite-size system effects in the free energies of the crystal and the rotator phases, we computed the free energies for system sizes $N = 1024$, 1458, and 2000 particles and used them to determine the free energy in the limit of $N \to \infty$. We used the finite-size scaling method as proposed by Frenkel *et al.* [96] to determine the free energy for $N \to \infty$.

The excess free-energy density defined as

$$\frac{F_{\text{ex}}}{Nk_BT} = \frac{F}{Nk_BT} - \frac{F_{\text{id}}}{Nk_BT} \tag{4.4}$$

is plotted as a function of $1/N$, for hard octahedra in a Minkowski crystal and in a bcc plastic-crystal phase, in Fig. 4.5. Following the finite-size scaling method in Ref. [96] we have fitted a straight line through the data points and determine the excess Helmholtz free energy per particle in the limit of $N \to \infty$ as shown in Fig. 4.5. The Helmholtz free energy per particle for the Minkowski crystal phase (at $\phi = 0.71052$) and the bcc plastic-crystal phase (at $\phi = 0.5$) are 12.3491 k_BT and 6.2259 k_BT, respectively.

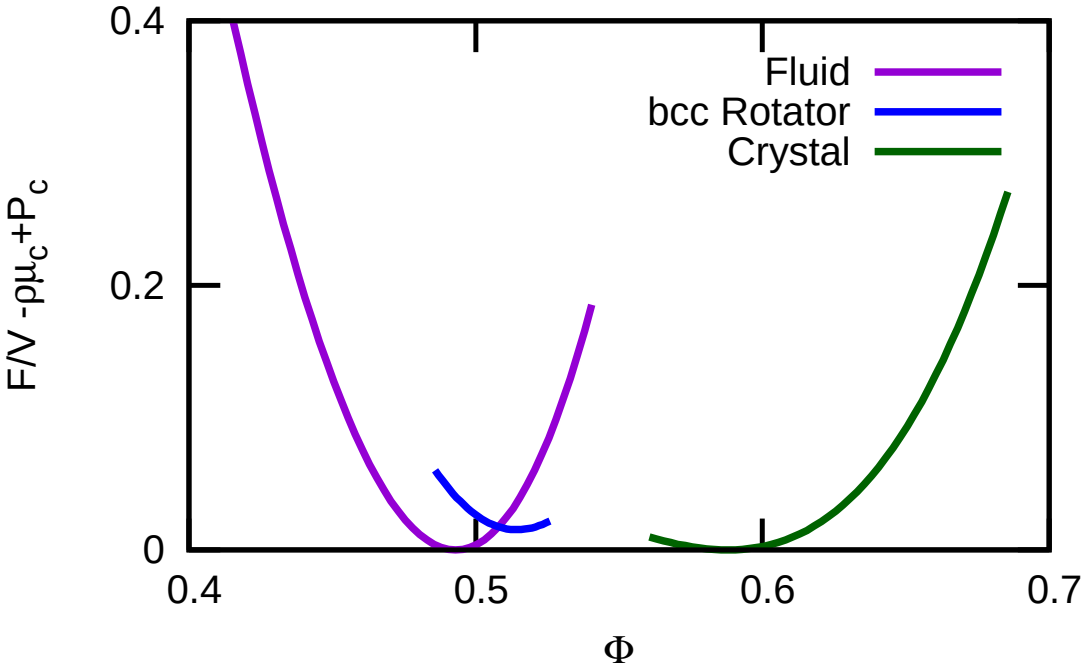

Figure 4.6: Free energy for octahedra: $F/V - \rho\mu_c - P_c$ is plotted as a function of packing fraction ϕ. Here F and V are the Helmholtz free energy and the volume of the system respectively; μ_c and P_c are the chemical potential and pressure at bulk coexistence respectively with ρ the number density of the particles. This plot shows clearly that the bcc rotator phase is metastable with respect to the coexistence between the fluid and the Minkowski crystal phase.

We estimated the statistical errors in the free-energy calculations to be on the order of $10^{-3}k_{\text{B}}T$ per particle. These calculated free energies along with the equations of state are

used to compute the free-energy density as a function of packing fraction using thermodynamic integration [96]. These calculated free-energy densities for all the three phases are shown in Fig. 4.6. Employing common-tangent constructions, we found that there is only phase coexistence between a fluid phase and a Minkowski crystal phase, while the bcc plastic-crystal phase is metastable. From our calculations we determine the coexisting densities of the fluid and Minkowski crystal to be at $\phi_f = 0.493$ and $\phi_m = 0.589$, respectively. We have plotted the scaled free-energy densities in Fig. 4.6 which clearly shows the co-existing densities.

In a similar fashion, we compute the phase boundaries for the remaining particles in the range $q \in [0.5, \infty]$ and map out the phase diagram. The phase diagram can be divided into two broad regions based on their shape, namely (1) octahedron-like and (2) cube-like superballs. We discuss the two parts of the phase diagram below.

4.3.2 Octahedron-like Superballs ($0.5 \leq q < 1$)

We first turn our attention to octahedron-like superballs. We used floppy-box MC simulations with a small number of particles to compress the system to a high pressure state in order to find the best-packed crystal structures. For shape parameter values $0.79248 < q < 1$, we obtained a denser structure than the predicted O_0 lattice of Refs. [102, 103]. For instance, after compressing the system to pressures around $P^* = 10^7$ at $q = 0.85$, we obtained a body-centered-tetragonal (bct) crystal with $\phi = 0.7661$. This is denser than the O_0 crystal, which achieves $\phi = 0.7656$ at $q = 0.85$. Note however that these two crystals are very similar to each other, since O_0 is also a form of a bct lattice. The only difference is that the orientation of the particles in the O_0 crystal is the same as the symmetry of the axes in the crystal lattice, while in our bct crystal there is a small angle between these two orientations in the square plane of the crystal. Furthermore, for $q < 0.79248$, we also found a crystal with denser packing than the predicted O_1 crystal in Refs. [102, 103]. For $q = 0.7$, we also performed floppy-box MC simulations to determine the close-packed structures. We found a deformed bcc (dbcc) crystal shown in Fig. 4.8, which is an intermediate form between the bcc lattice and the Minkowski crystal [111]. The lattice vectors are $\mathbf{e}_1 = 0.912909\mathbf{i} + 0.912403\mathbf{j} - 0.912165\mathbf{k}$, $\mathbf{e}_2 = -0.271668\mathbf{i} + 1.80916\mathbf{j} - 0.288051\mathbf{k}$, and $\mathbf{e}_3 = 0.28834\mathbf{i} - 0.272001\mathbf{j} - 1.80882\mathbf{k}$, where $\mathbf{i}$, $\mathbf{j}$, and $\mathbf{k}$ are the unit vectors along the axes of the particle. Our dbcc crystal is close to the predicted O_1 crystal, whose lattice vectors are $\mathbf{e}_1 = 0.912492\mathbf{i} + 0.912492\mathbf{j} - 0.912492\mathbf{k}$, $\mathbf{e}_2 = -0.2884\mathbf{i} + 1.80629\mathbf{j} - 0.2884\mathbf{k}$, and $\mathbf{e}_3 = 0.2884\mathbf{i} - 0.2884\mathbf{j} - 1.80629\mathbf{k}$. However, it has a packing fraction of $\phi = 0.832839$ which is denser than the predicted O_1 crystal with $\phi = 0.824976$ in Refs. [102, 103] by roughly 1%. In Refs. [102, 103], the O_0 and O_1 phases are found to switch at $q = 0.79248$. We also observed that the bct and dbcc crystals both transform into the bcc phase at $q = 0.79248$.

As shown in Fig. 4.8, when the shape of the superballs is close to spherical, i.e., $0.7 < q < 3$ corresponding to an asphericity $A \lesssim 0.08$ for cube-like and $A \lesssim 0.03$ for octahedron-like superballs, there is always a stable fcc plastic-crystal phase. Surprisingly, when the shape of superballs is octahedron-like, we find a stable bcc plastic-crystal phase. Moreover, around $q = 0.8$ we even find a fairly broad two-phase regime where a low-density fcc plastic crystal coexists with a high-density bcc plastic-crystal phase.

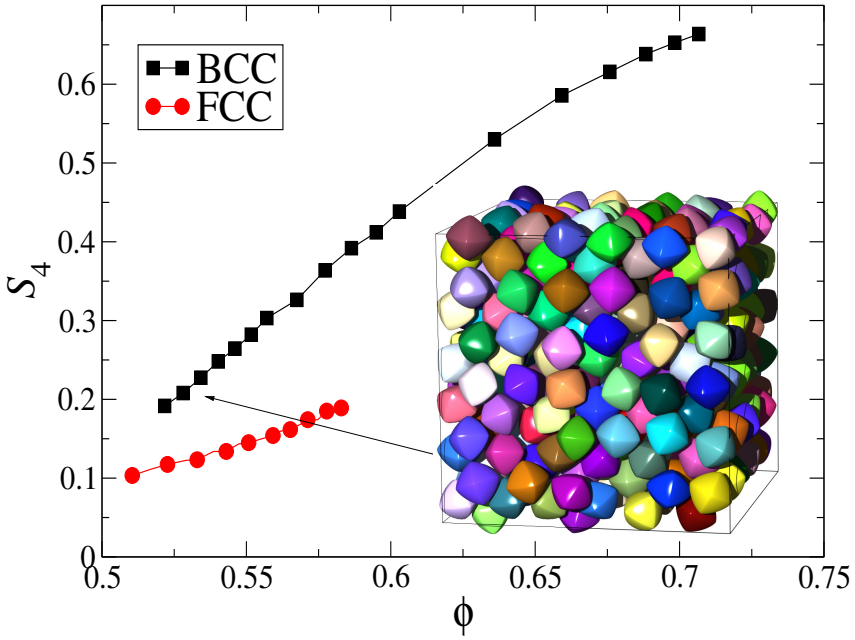

Figure 4.7: Cubatic order parameter S_4 as a function of packing fraction ϕ for a bcc and a (metastable) fcc plastic-crystal phase of hard superballs with $q = 0.7$. The inset shows a typical configuration of a bcc plastic crystal of hard superballs with $q = 0.7$ at $\phi = 0.54$.

In order to quantify the orientational order in the bcc phase we calculate the cubatic order parameter S_4. We show S_4 in Fig. 4.7 as a function of packing fraction ϕ for the bcc plastic-crystal phase of superballs with $q = 0.7$. For comparison, we also show S_4 for the (metastable) fcc plastic-crystal phase for which the cubatic order is always very low $S_4 \lesssim 0.2$. We observe that $S_4 \simeq 0.2$ at low packing fractions, which means that there is a very weak orientational order in the system [112]. With increasing packing fraction, the cubatic order parameter increases monotonically to around 0.65 at a packing fraction of 0.7, which is indicative of a medium-ranged orientationally ordered system. This suggests that the entropic repulsion due to the rotation of the octahedron-like superballs stabilizes the bcc lattice. Moreover, as a bcc-like phase is the best-packed crystal structure for these superballs, the translational entropy gained in the bcc rotator phase outweighs the loss in orientational entropy compared to the fcc rotator phase at the same packing fraction.

4.3.3 Cube-like Superballs ($1 < q < \infty$)

The other part of the phase diagram concerns the cube-like superballs. The best-packed crystal structures are determined in Ref. [113] and are given by C_0 and C_1 crystals. The lattice vectors for C_0 crystals are given by $\mathbf{e}_1 = 2^{1-1/2q}\,\mathbf{i} + 2^{1-1/2q}\,\mathbf{j}$, $\mathbf{e}_2 = 2\,\mathbf{k}$, and $\mathbf{e}_3 = -2s\mathbf{i}+2(s+2^{-1/2q})\mathbf{j}+\mathbf{k}$, where $\mathbf{i}$, $\mathbf{j}$ and $\mathbf{k}$ are the unit vectors along the axes of the particle, and s is the smallest positive root of the equation $(s+2^{-1/2q})^{2q} + s^{2q} + 2^{-2q} - 1 = 0$. The lattice vectors for C_1 crystals are given by $\mathbf{e}_1 = 2^{1-1/2q}\,\mathbf{i}+2^{1-1/2q}\,\mathbf{j}$, $\mathbf{e}_2 = 2^{1-1/2q}\,\mathbf{i}+2^{1-1/2q}\,\mathbf{k}$, $\mathbf{e}_3 = 2(s+2^{-1/2q})\,\mathbf{i} - 2s\,\mathbf{j} - 2s\,\mathbf{k}$, where s is the smallest positive root of the equation $(s+2^{-1/2q})^{2q} + 2s^{2q} - 1 = 0$, and there is only one particle in the unit cell [102, 103]. For instance, in a C_1 crystal of superballs with $q = 2.5$, one finds that $\langle \mathbf{e}_1, \mathbf{e}_2 \rangle = 0.5$,

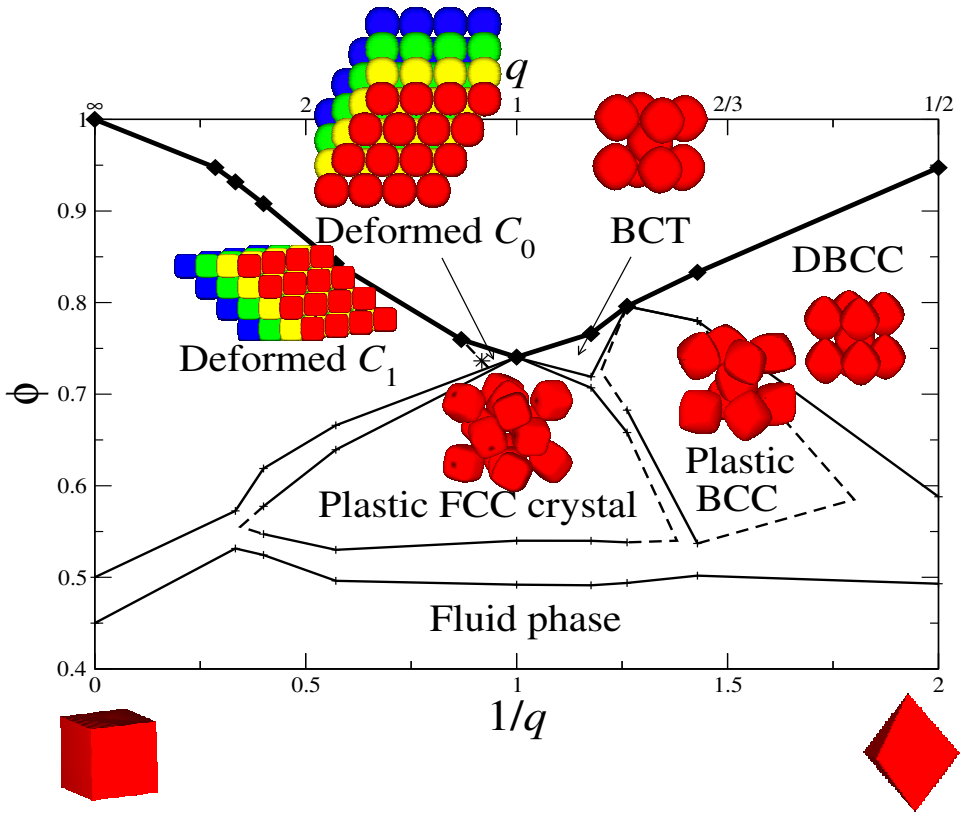

Figure 4.8: Phase diagram for hard superballs in the ϕ (packing fraction) versus $1/q$ (bottom axis) and q (top axis) representation where q is the deformation parameter. Here the C_1 and C_0 crystals are defined in the main text and in Refs. [102, 103], where the particles of the same color are in the same layer of stacking. The solid diamonds indicate the close packing, and the locations of triple points are determined by extrapolation as shown by the dashed lines. The phase boundaries for hard cubes are taken from Ref. [79].

$\langle \mathbf{e}_1, \mathbf{e}_3 \rangle = \langle \mathbf{e}_3, \mathbf{e}_2 \rangle = 0.60552$, $|\mathbf{e}_2| / |\mathbf{e}_1| = 1$, and $|\mathbf{e}_3| / |\mathbf{e}_1| = 0.825737$, where $\langle \mathbf{e}_i, \mathbf{e}_j \rangle$ is the cosine of the angle between $\mathbf{e}_i$ and $\mathbf{e}_j$. Our simulation results show that both the C_0 and the C_1 crystals deform with decreasing density. The calculated angles and the length ratios between lattice vectors as a function of packing fraction ϕ for the cube-like particles with $q = 2.5$ are shown in Fig. 4.9. We find that at packing fractions approaching close packing, the crystal remains in the C_1 phase. With decreasing packing fraction, the crystal lattice deforms towards an fcc structure: $\langle \mathbf{e}_1, \mathbf{e}_2 \rangle = \langle \mathbf{e}_1, \mathbf{e}_3 \rangle = \langle \mathbf{e}_2, \mathbf{e}_3 \rangle = 0.5$ and $|\mathbf{e}_2| / |\mathbf{e}_1| = |\mathbf{e}_3| / |\mathbf{e}_1| = 1$.

Moreover, when $1 < q < 3$, it is found that the deformed C_0 and deformed C_1 crystal melt into an fcc plastic-crystal phase. By Einstein integration, we calculated the Helmholtz free-energy as a function of packing fraction for both the fcc plastic crystal and the deformed C_1/C_0 crystal phases [96]. Combined with the free-energy calculations for the fluid phase done by Widom's particle insertion method, we obtain the phase boundaries in the phase diagram shown in Fig. 4.8. The part of the phase diagram for hard cube-like superballs roughly agrees with the empirical phase diagram by Batten *et*

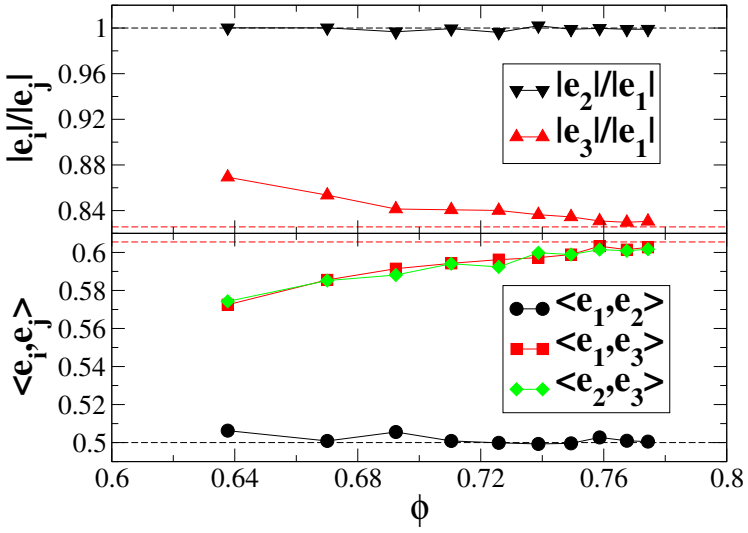

Figure 4.9: The deformation of the crystal unit cell with lattice vectors $\mathbf{e}_i$ as a function of packing fraction ϕ in a system of hard superballs with $q = 2.5$. The dashed lines in the figures indicate the values for the C_1 crystal.

al. [81]. At high packing fractions, there are stable deformed C_0 and C_1 phases. When $q > 1.1509$, the close-packed structure is the C_1 crystal, whereas it is the C_0 crystal whenever $1 < q < 1.1509$ [102, 103]. To determine the location of the transition from the deformed C_0 crystal to the deformed C_1 crystal, we performed two series of NPT MC simulations with increasing value of q for the first series and decreasing q for the second series of simulations at pressure $P^* = Pv_p/k_BT \simeq 250$, with v_p the volume of the particle [104]. The first series started from a C_0 crystal phase, while the second series of simulations started from a C_1 crystal phase. Our simulations show that the phase transition occurred around $q = 1.09$ at packing fraction $\phi = 0.736$ as shown by the asterisk in Fig. 4.8. Moreover, for hard cubes ($q = \infty$) the C_1 crystal is a simple cubic (sc) crystal. Although it was found that for hard cubes there is a significant number of vacancies in the simple cubic crystal, it only shifts the phase boundary by $\sim 2\%$ in packing fraction [79]. In our simulations, we did not observe any vacancies in the crystals of hard superballs with $q \leq 3$, we therefore assume that the possible presence of vacancies would not shift the phase boundary significantly.

4.4 Conclusion

In conclusion, using free-energy calculations we have determined the full phase diagram of hard superballs with shapes interpolating between cubes and octahedra, i.e., $0.5 \leq q < \infty$. In systems of cube-like superballs ($q > 1$), we find a stable deformed C_1 phase at high packing fraction, except close to the sphere-limit ($q = 1$) where a deformed C_0 crystal is stable. For $q < 3$ the crystal phase melts into an fcc plastic crystal before melting into a

fluid phase of cube-like superballs. In systems of octahedron-like superballs ($0.5 < q < 1$), we find a stable bct or a deformed bcc crystal phase upon approaching close packing, with a crossover at $q = 0.79248$. Moreover, a stable fcc plastic crystal appears at intermediate densities for $0.7 < q \leq 1$. Interestingly, for $q < 0.85$, we find a novel stable bcc plastic-crystal phase, which can even coexist with the fcc plastic-crystal phase at around $q = 0.8$. It is worth noting that phase coexistence between a bcc and an fcc plastic-crystal phase have been predicted for particles interacting with soft potentials, e.g., for simple water models [114]. More surprisingly, the bcc and fcc rotator phases are unstable for the flat-faced and sharp-edged hard octahedra and hard cubes, respectively, which suggests that the asphericity A as defined in Eq. 4.2 and the curvature of superballs may play an important role in stabilizing rotator phases. As the asphericity A increases smoothly by deviating from $q = 1$, as shown in Fig. 4.1, it is hard to define a stability criterion for the plastic-crystal phases based on a threshold value of A. However, we find stable rotator phases for the shape parameter range $0.7 < q < 3$, which corresponds to an asphericity $A \lesssim 0.08$ for cube-like and $A \lesssim 0.03$ for octahedron-like superballs. It is important for the particles in the rotator phase to switch from one symmetry direction to the other. This might depend on factors like shape of particle, crystal structure, and packing fraction. Hence, it is hard to make a definite statement that explains the formation of rotator phases. Here we find that particles with low asphericity ratio $A << 1$ tend to form rotator phases.

Finally, it is interesting to compare the present phase diagram to that of hard truncated cubes as described in Chapter 2 and Ref. [49] for which the shape interpolates from cubes to octahedra, but *via* cuboctahedra instead of sphere. Although there are similarities between the two phase diagrams, such as stable plastic crystal phases in the center of the phase diagram, there are also striking differences. (i) The stable plastic crystal regimes are much smaller for polyhedral particles than for superballs. (ii) The phase behavior as a function of shape parameter is much smoother for hard superballs than for truncated cubes. These observations lead to the idea that the more spread-out local curvature of the superball tend to favor the formation of rotator phases and have a smoother phase behavior whereas the polyhedral particles with flat faces and sharp edges prefer to align flat faces to form crystals and have sharp transitions even though the shape parameter s varies smoothly. In conclusion, nanoparticle self-assembly is surprisingly sensitive to particle shape.

Acknowledgments

It is a pleasure to thank Dr. Ran Ni for fruitful collaboration and for calculating the phase diagram for superballs. I also would like to thank Dr. Joost de Graaf for collaborating in computing the phase diagram of hard octahedra and for useful discussions.

5

Self-Assembly of Colloidal Hexagonal Bipyramid- and Bifrustum-Shaped Nanoparticles into Two-Dimensional Superstructures

We present a combined theoretical and simulation study on the self-assembly of colloidal hexagonal bipyramid- and hexagonal bifrustum-shaped nanoparticles in two dimensions. The self-assembled structures as obtained in simulations are in good agreement with those observed in experiments on colloidal nanocrystals. Our work shows that the self-assembly of the hexagonal bipyramid- and bifrustums in experiments is primarily driven by minimization of the interfacial free energies and maximization of the packing density. Also, our study shows that a small truncation of the hexagonal bipyramids is sufficient to change the symmetry of the resulting superlattice from hexagonal to tetragonal, highlighting the crucial importance of precise shape control in the fabrication of functional metamaterials by self-assembly of colloidal (or nano) particles.

5.1 Introduction

Self-assembly of colloidal nanocrystals (NCs) into ordered superlattices (NC solids) is emerging as a versatile approach to design and fabricate novel metamaterials with tailored optoelectronic properties, which are promising for a variety of devices, such as solar cells, LEDs, photodetectors, and lasers [115–124]. The collective properties of NC solids arise from the intrinsic characteristics of the building blocks and the synergistic interactions between them and can thus be engineered by a judicious choice of the colloidal NCs (composition, size, shape, surface), and the stoichiometry and spatial symmetry of the resulting self-assembled superstructure [115–118, 125, 126]. Nevertheless, a comprehensive set of design rules for NC superstructures has yet to emerge, although the concerted efforts of experimentalists and theoreticians worldwide have led to great advances in recent years [49, 115, 116, 127–133].

Single- and multicomponent superlattices of isotropic, nearly spherical NCs have been extensively investigated over the last two decades, producing a remarkable variety of superstructures and greatly advancing the fundamental understanding of the self-assembly process [115, 116, 127–133]. Recent advances in the synthesis of colloidal NCs have dramatically extended the ability to control not only the shape but also the composition of the NC, yielding a wealth of complex anisotropic NCs and hetero-NCs [134]. Moreover, novel theoretical and simulation techniques have been developed in recent years, allowing more complex problems to be solved [49, 135, 136]. This has led to a surge of experimental and simulation interest on superlattices of anisotropic NC building blocks [5, 50, 67, 67, 98, 117, 131, 137–152]. In particular, two-dimensional (2D) superstructures of anisotropic NCs are attracting increasing attention, because their properties may be substantially different from those of three-dimensional (3D) NC superstructures, making them suitable for the fabrication of functional ultrathin films and membranes that take full advantage of the shape-dependent and directional properties of anisotropic NCs. For example, nanorods have been shown to form both 2D superlattices [150, 151] and 3D mesoscopic supercrystals [152]. The formation of 2D and 3D self-assembled superstructures has also been studied for other anisotropic colloidal NCs, such as nanoplates, truncated cubes, octahedra, or octapods, both experimentally and by theory and simulation [131, 142–148]. Although these studies provided valuable insight in the self-assembly behavior of anisotropic colloidal NCs, the driving forces behind the self-organization process are still not fully understood. For instance, the relationship between the NC shape and the symmetry of the self-assembled superlattice has not yet been investigated in detail. This is particularly relevant not only from a fundamental viewpoint, but also as a step towards the development of a framework that allows the design and fabrication of tailored NC superstructures.

Here, we report a simulation study on the self-assembly of hexagonal bipyramid and hexagonal bifrustum-shaped NCs into 2D superlattices (see Fig. 5.5 for a graphical illustration of the shapes). Experimentally, superstructures of these building blocks can be obtained by slow evaporation of the solvent on a dense liquid surface as shown in Fig. 5.1 using a cartoon. To this end, a concentrated NC solution is brought onto a very dense liquid surface. Then the solvent is allowed to evaporate slowly resulting into the formation of 2D superstructures of nanocrystals. We study this self-assembly pro-

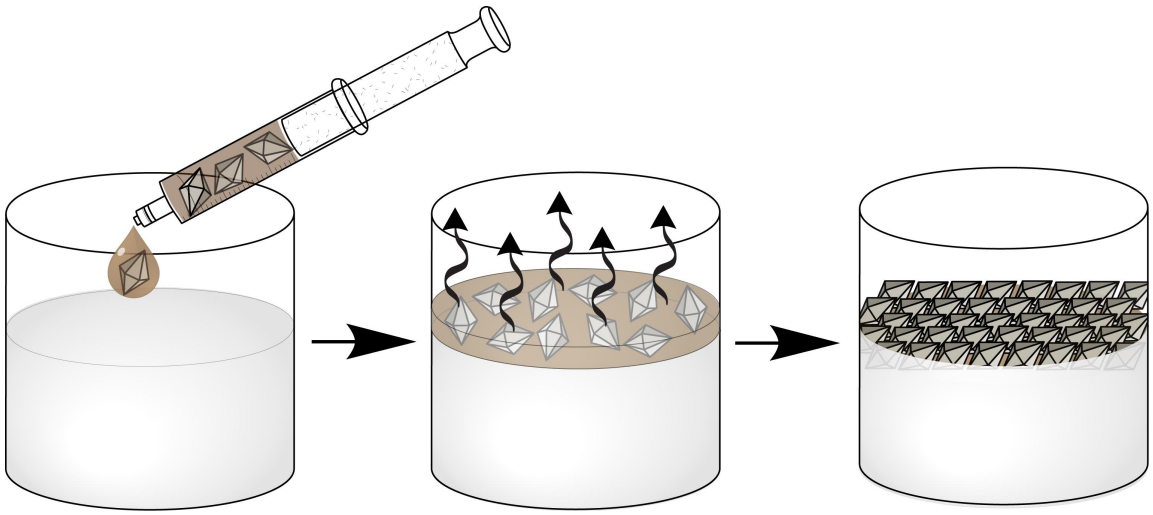

Figure 5.1: Cartoon to describe the experimental procedure to self-assemble NCs at the liquid-air interface. A concentrated NC solution is brought onto a very dense liquid surface. The solvent is allowed to evaporate slowly , resulting in the formation of a continuous membrane at the liquid-air interface.

cess by modeling the NCs as hard anisotropic polyhedral nanoparticles at a planar 2D solvent-air interface. The minimum free-energy configurations (the equilibrium position and orientation) of individual NCs at the interface were theoretically calculated [49, 153] and used in isothermal-isobaric Monte Carlo simulations [49, 71, 72] to determine the phase behavior of the ensemble of NCs. We found that the resulting NC superstructures as obtained from our simulations show good agreement with those observed experimentally. Our results show that the experimental self-assembly process is primarily driven by minimization of the interfacial free energies and maximization of the packing density. Interestingly, the simulations show that the small truncation observed at the tips of the hexagonal bipyramid-shaped NCs has a dramatic impact on the symmetry of the resulting superlattice, changing it from hexagonal to tetragonal. This highlights the pivotal role of precise shape control in the design and fabrication of functional materials by self-assembly of colloidal NCs.

5.2 Interfacial Adsorption

In this section we explain the interfacial free-energy calculations of the nanoparticles at the liquid-air interface. In order to compare out results with the experiments we consider toluene to be the liquid phase. Following Pieranksi [154], we write the interfacial free energy of a nanoparticle with its center of mass at a height z (with respect to the planar air-toluene interface) and with angles ϕ (the polar angle with respect to the interface normal, see Fig. 5.2) and ψ (the internal Euler angle about the long axis of the nanoparticle, see Fig. 5.2), as

$$F(z,\phi,\psi) = \gamma_a S_a(z,\phi,\psi) + \gamma_t S_t(z,\phi,\psi) - \gamma_{at} S_{at}(z,\phi,\psi) + \text{const} \tag{5.1}$$

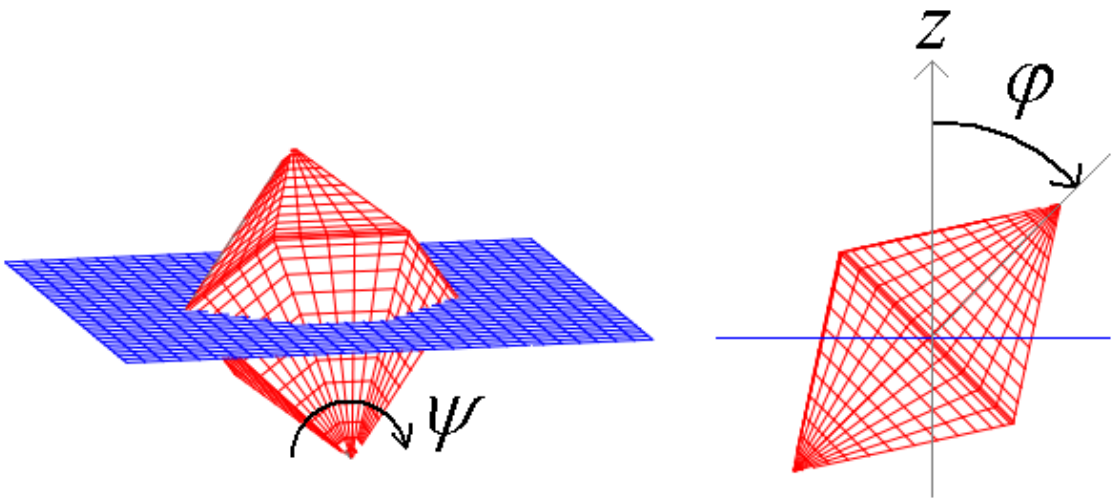

Figure 5.2: Definition of different orientational angles of the hard particles with respect to the interface used in Eq. 5.1.

Here S_a and S_t denote the area of the particle surface that is in contact with air and toluene, respectively, and S_{at} is the surface area taken out from the air-toluene interface by the particle. All three areas S_a, S_t, and S_{at} depend non-trivially on the position and orientation of the particle and need to be calculated numerically. The particle-toluene tension is denoted by γ_t, the particle-air tension by γ_a, and the arbitrary constant in Eq. 5.1 is chosen such that $F = 0$ for a particle that is completely immersed in toluene. The adsorption free energy of Eq. 5.1 ignores capillary deformations and line tension contribution for simplicity. In fact, given that the total particle surface area $S_a + S_t$ is a constant, one easily checks that $F(z, \phi, \psi)$ does not depend on γ_t and γ_a separately but only on their difference through the contact angle θ defined by Young's equation,

$$\cos\theta = (\gamma_a - \gamma_t)/\gamma_{at} = 0.8, \tag{5.2}$$

where the numerical value is an estimate based on the observed favorable (low free-energy) configurations. It should be noted that although ignoring capillary deformations of the toluene-air interface gives rise to a violation of the force balance on the toluene-air-particle contact line, we expect this to have a negligible effect on the optimal configuration since the sharp edges of the flat facet adsorbed to the interface cause a rapid variation of the surface curvature to which the air-toluene interface can adapt without any substantial deformation.

Using a triangular tessellation technique to calculate the surface areas S_a, S_t, and S_{at}, we obtain the equilibrium configuration from minimizing F with respect to the particle configuration. For three nanoparticle shapes of interest, Fig. 5.3 shows these equilibrium configurations, as well as their coordinates and free energies as a function of the polar angle ϕ (minimized with respect to z and the internal angle ψ). The perfect hexagonal bipyramid has minimum free energy when one of its triangular facets is completely adhered to the interface (Fig. 5.3A). For this configuration, a local minimum of $-200\ k_BT$ is found. It is interesting to note that the particle remains completely immersed in the liquid phase, except for the facet that is adhered to the interface (whereas the particle pays a free-energy

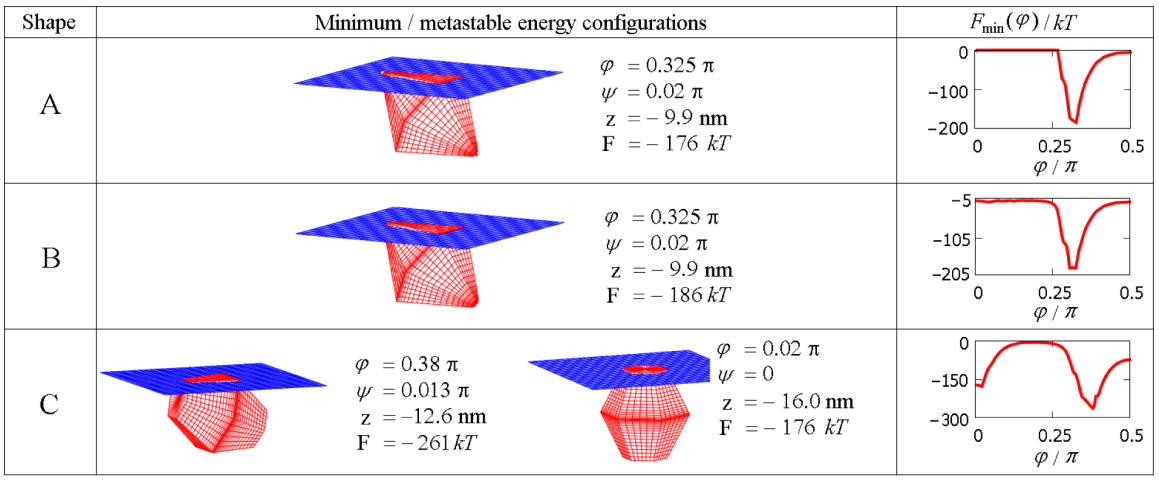

Figure 5.3: Minimum free-energy configurations (and their coordinates and minimal free energy) for three particle shapes in a planar air-toluene interface as obtained from Eq. 5.1 and triangular tessellations of the surfaces, (A) perfect hexagonal bipyramid, (B) slightly truncated hexagonal bipyramid, and (C) hexagonal bifrustums. The right panels give the interfacial free energy of the particle as a function of the polar angle ϕ minimized with respect to the particle height z and the internal Euler angle about the long axis of the nanoparticle, ψ.

penalty of $F \approx 10^4 k_B T$ if it is completely in air). The colloidal NCs used in the self-assembly experiments are, however, not perfect hexagonal bipyramids, but instead have slightly truncated tips (5% of their length). Nevertheless, according to our calculation this small truncation does not affect the single-particle equilibrium configuration at the interface, which remains essentially the same as that of a perfect hexagonal bipyramid (Fig. 5.3B). By contrast, according to our calculations a hexagonal bifrustum nanoparticle has two possible equilibrium configurations in which either 1 of the 12 trapezoidal facets or 1 of the 2 hexagonal facets is adhered to the interface (Fig. 5.3C). Both free-energy minima are sufficiently deep to make the adhesion irreversible (Fig. 5.3C), and consequently the hexagonal bifrustum nanoparticles have multiple options for interfacial adhesion.

5.3 Monte Carlo Simulations

Once the equilibrium adsorption configurations of individual nanoparticles at the air-toluene interface are theoretically determined, we predict the self-assembled structures by using the floppy-box Monte Carlo (FBMC) method [71, 72] in combination with the separating-axis-based overlap algorithm [84]. In the FBMC method, we perform Monte Carlo simulations in the isothermal-isobaric ensemble (NPT) and compress the system from the isotropic fluid phase to the solid phase using a variable shape of the simulation box. The immersion depth z and the polar angle ϕ of the nanoparticle with respect to the air-toluene interface are kept fixed according to the values determined for the equilibrium adsorption configurations, and the particles are only allowed to translate and rotate in the plane of the interface. Because of the symmetry of the hexagonal bifrustums (33 nm in all directions), the orientation of the NC is not important for the overall self-assembly

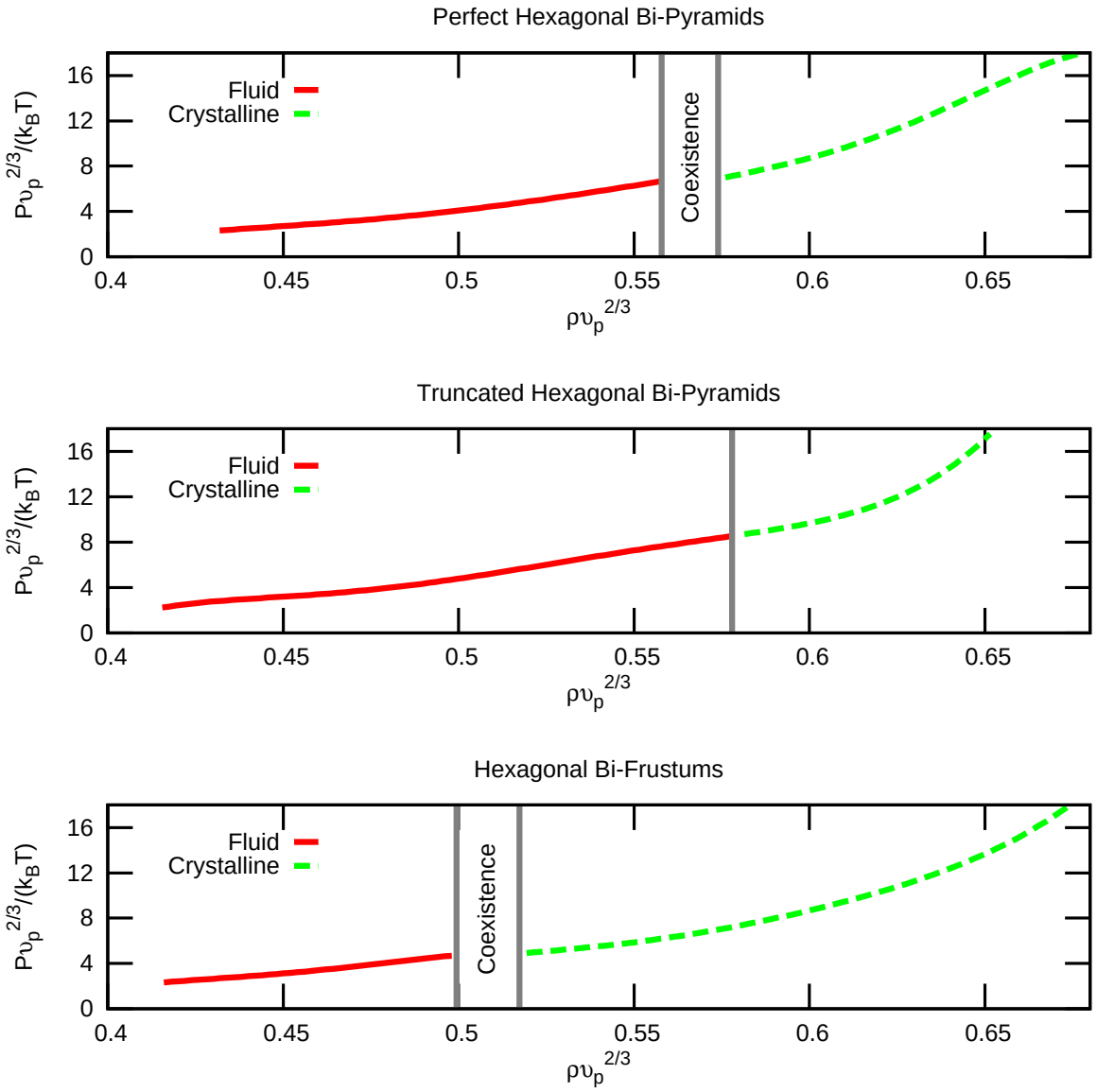

Figure 5.4: Equations of State (EOS), reduced pressure $\frac{P\upsilon_p^{2/3}}{k_BT}$ *versus* scaled number density $\rho^* = \rho\upsilon_p^{2/3}$, obtained using floppy-box Monte Carlo (FBMC) simulations. Perfect hexagonal bipyramids (BPs) undergo a first-order transition with coexisting densities $\rho^* \approx 0.56$ and 0.57 from the isotropic fluid phase to a hexagonal lattice, while slightly truncated hexagonal BPs show a weak first-order transition around $\rho^* \approx 0.58$ from an isotropic phase to a tetragonal lattice. Hexagonal bifrustums (BFs) crystallize *via* a first-order phase transition from the isotropic fluid into a hexagonal lattice with coexisting densities $\rho^* \approx 0.50$ and 0.52.

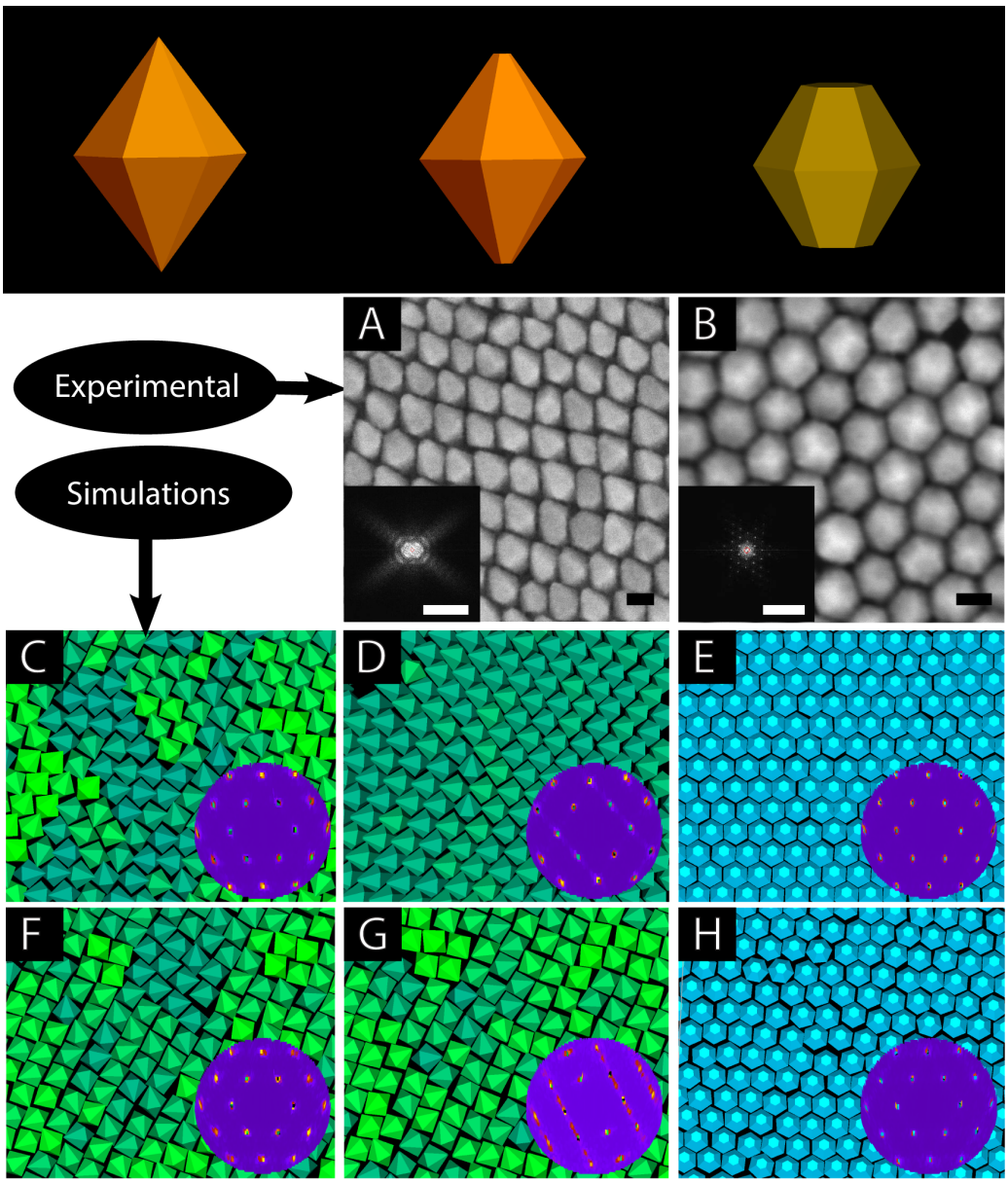

Figure 5.5: Top panel: Schematics of the particle geometries used in the Monte Carlo simulations. From left to right: the perfect hexagonal bipyramid, slightly truncated hexagonal bipyramid, and the hexagonal bifrustum. Second row from top: SEM images of self-assembled superlattices of (A) hexagonal bipyramid-shaped ZnS NCs, and (B) hexagonal bifrustum-shaped ZnS NCs. The insets give the fast Fourier transform patterns of the corresponding experimental images of superlattices . The scale bars correspond to 20 nm (0.2 nm^{-1} in the insets). Bottom two rows. Snapshots of the isothermal-isobaric Monte Carlo simulations showing the various structures that form during the 2D self-assembly of hexagonal bipyramids (C,D,F,G) and hexagonal bifrustums (E,H) adhered to an air-toluene interface. The corresponding reciprocal space patterns of the center of mass of the particles in the simulated NC superlattice are also displayed (bottom right insets). The orientation of the particles with respect to the interface is fixed based on the equilibrium configurations obtained from the interfacial free-energy calculations (see Fig. 5.3). The relative orientation of the particles is color coded. (C-E) Simulation snapshots at a reduced density $\rho^* = \rho \upsilon_p^{2/3} = 0.69$ with υ_p the particle volume. (F-H) Simulation snapshots at $\rho^* = 0.65$.

behavior, because the NC can occupy a hexagonal site in the array regardless of whether a trapezoidal or hexagonal facet is adsorbed to the interface. Therefore, for simplicity only the hexagonal adhered surface is considered in the FBMC simulations. The volume of the nanoparticles υ_p is set to unity in all cases.

Subsequently, we use the predicted orientations of the particles from interfacial adsorption calculations in Monte Carlo simulations to determine the phase behavior of an ensemble of nanoparticles. To this end, we calculate the equations of state (EOS) in Monte Carlo simulations by compressing a dilute fluid state to very high pressures, which we show in Fig. 5.4. The simulations show that perfect hexagonal bipyramids crystallize via a first-order phase transition with coexisting densities $\rho^* \approx 0.56$ and 0.57 into a hexagonal superlattice (Fig. 5.5C). Hexagonal bifrustums also crystallize via a first-order transition from the isotropic fluid into a hexagonal lattice with coexisting densities $\rho^* \approx 0.50$ and 0.52 (Fig. 5.5E). In contrast, slightly truncated bipyramids show a weak first-order transition from the isotropic phase to a tetragonal phase around $\rho^* \approx 0.58$ (Fig. 5.5D). This is remarkable because the equilibrium configuration of the single NC adhered to the air-toluene interface was not significantly affected by the truncation (see above, Fig. 5.3). This can be rationalized by considering that the truncation allows the NCs to come in closer proximity, thereby leading to a higher packing density, and hence a tetragonal rather than hexagonal lattice. The crystal structures can be determined from the reciprocal space pattern of the center of mass of the particles in the simulated NC superstructure. Fig. 5.5 shows the reciprocal space patterns and the real space configurations of the NC superlattices formed during the FBMC simulations at two different reduced densities $\rho^* = \rho\upsilon_p^{2/3} = 0.65$ and 0.69 with υ_p as the particle volume, $\rho = N/A$ is the areal number density, N is the number of particles, and A is the surface area of the interface. The experimentally observed NC superlattices are also included for comparison (Fig. 5.5A-B).

5.4 Conclusions

In conclusion, our work shows that the experimentally observed self-assembly behavior of hexagonal bipyramid- and bifrustum- shaped nanocrystals at a liquid-air interface is well described by a combination of theoretical adsorption free-energy calculations and Monte Carlo simulations. Our results show that the superlattice formation is driven primarily by minimization of the interfacial free energies and maximization of the packing densities. Moreover, our results show that truncation of the tips of hexagonal bipyramids by as little as 5% is sufficient to change the symmetry of the resulting superlattice from hexagonal to tetragonal. This demonstrates that precise shape control is of crucial importance in the fabrication of functional materials by self-assembly of colloidal NCs. Also, it is very comfortable to note that the relatively simple Pieranski potential of Eq. 5.1 combined with Monte Carlo simulations actually has quantitative predictive power, which may be further exploited in the study of other particle shapes and material parameters.

5.5 Acknowledgements

It is a pleasure to thank Ward van der Stam, Quinten A Akkerman, and Prof. dr. Celso de Mello Donega of the Condensed Matter and Interfaces group, Utrecht University, where the self-assembly study of the hexagonal bipyramid- and bifrustum- shaped nanocrystals at a liquid-air interface was initiated and all experiments were performed, for the fruitful collaboration on this project. I also would like to thank to Giuseppe Soligno and Prof. dr. René van Roij of The Institute for Theoretical Physics, Utrecht University, for performing the theoretical adsorption free-energy calculations and for the fruitful collaboration on this project.

6

Phase Diagram of 2D Hard Triangles: A Novel Chiral Phase with Chiral Holes

We determine the phase diagram of hard equilateral and right-angled isosceles colloidal triangles in two dimensions using Monte Carlo simulations. Simple hard equilateral triangles undergo a continuous isotropic-triatic liquid crystalline phase transition at area fraction $\phi = 0.70$. Similarly, hard right-angled isosceles triangles exhibit a first-order phase transition from an isotropic fluid phase to a rhombic liquid crystalline phase with $\phi_c = [0.733, 0.782]$. These liquid crystal phases of the triangular systems undergo a continuous phase transition to their respective close-packed crystal structure at high pressures. Although the particles and their close-packed crystals are both achiral, the solid phases of equilateral and right-angled triangles exhibit spontaneous chiral symmetry-breaking at sufficiently high area fractions. The colloidal triangles spontaneously rotate either in clockwise or anti-clockwise direction with respect to one of the lattice vectors for area packing fractions higher than ϕ_χ. As a consequence, these triangles arrange themselves in such a way that they form a regular lattice of chiral holes surrounded with six triangles for equilateral triangles and four or eight triangles for right-angled triangles. These chiral holes are either right- or left-handed. Moreover, our simulations show a spontaneous entropy-driven demixing transition of the right- and left-handed chiral phases.

6.1 Introduction

Chirality plays an important role in nature, chemistry, and materials science. An object is chiral if it is not identical to its mirror image. The most well-known example of a chiral object is the human hand, where the left hand cannot be superimposed on its mirror image, the right hand. Also many biologically active molecules are chiral, e.g., amino acids are left-handed, whereas sugars are right-handed. The microscopic chirality of the constituent particles may subsequently lead to a macroscopic chirality of the self-assembled higher-ordered structures, e.g., left-handed amino acids form right-handed helical protein structures, and right-handed sugars lead to right-handed DNA double helices. Additionally, chirality is present in so-called cholesteric phases, which are nematic liquid crystals with a helical structure of the director field and which are frequently used in optoelectronic applications, such as liquid crystal displays of laptop computers, cell phones, and flat screen televisions. Recently, chiral nanostructured materials have also received much attention due to their intriguing optical properties such as a huge optical activity, strong circular dichroism, photonic band gaps, and negative refractive indices [155–157]. However, despite the huge amount of work devoted to chirality, the underlying microscopic features of the building blocks responsible for the formation of chiral self-assembled structures is extremely subtle and not well-understood.

Even the most basic question if particle shape alone can lead to macroscopic chiral structures is still unknown. For instance, it has been theoretically demonstrated that an entropy-driven isotropic-cholesteric phase transition exist for hard helical particles, but these predictions have never been verified experimentally or by computer simulations [158–160]. A more intriguing question would be whether or not achiral particles can self-assemble into chiral structures. Very recent experiments by Mason *et al.* on equilateral triangular colloidal platelets show an entropy-driven phase transition from the isotropic liquid to a triatic liquid crystal phase that displays three-fold symmetric orientational order [11]. Surprisingly, at sufficiently high densities, small domains of chiral dimer pairs that are laterally shifted in one or the opposite direction, appear spontaneously in the triatic phase. The authors conjectured that the spontaneous local chiral symmetry breaking is due to an increase in rotational entropy and may be explained by a simple rotational cage model [11, 161]. However, a recent simulation study explained the emergent chirality observed in these experiments by the rounded corners of the particles which lead trivially to two degenerate crystal lattices of chiral dimer pairs at close-packing, thereby casting doubts on the role of rotational entropy on the chiral symmetry breaking [162]. In addition, these simulations showed that the chiral symmetry breaking is absent for perfect triangles, i.e., no particle corner rounding, which is to be expected as the close-packed structure of perfect triangles is an *achiral* triangular lattice. These findings are also consistent with a previous simulation study on perfect equilateral triangles, which shows only a simple transition from the isotropic to a liquid crystal phase at area fraction $\phi = Na_p/A = 0.57$ with N the number of particles, A the area, and a_p the particle area [163].

In this chapter, we reexamine the phase behavior of hard equilateral triangles by extensive Monte Carlo simulations. We find the spontaneous formation of a novel chiral crystal phase, where the individual particles spontaneously undergo either a clockwise or

anti-clockwise twist with respect to one of the lattice vectors which gives rise to a regular lattice of anti-clockwise or clockwise chiral holes. A sketch of the positive and negative chiral holes is shown in Fig. 6.7a. We find a similar chiral crystal phase in a system of right-angled triangles. More surprisingly, we also observe a spontaneous entropy-driven demixing transition of the "enantiomers" into left-handed and right-handed chiral phases.

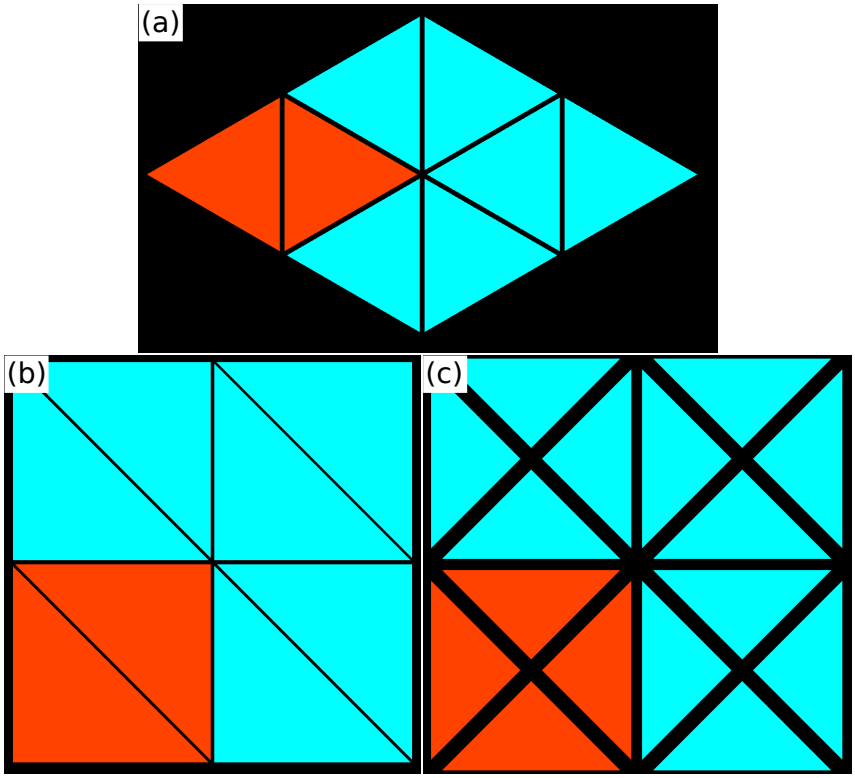

Figure 6.1: Candidate close-packed structures: (a) Equilateral triangles with two particles in the unit cell forming a hexagonal dimer lattice or a triatic crystal. Right-angled triangles with a rhombic lattice with two and four particles in the unit cell in (b) and (c), respectively. We show four unit cells for all the candidate close-packed structures particles and we used red color to indicate a single unit cell.

6.2 Methods

Hard equilateral and right-angled isosceles triangles tile the space in infinitely many ways as the rows and the columns of these triangles can be shifted without effecting their maximum packing density. However under finite pressures hard equilateral triangles form a triangular lattice with two particles in the unit cell as shown in Fig. 6.1a. For the right-angled triangles we employ a rhombic lattice with either two or four particles in the unit cell, which are shown in Fig. 6.1b and Fig. 6.1c, respectively. Here, we determine the phase behavior of hard equilateral and right-angled triangles using Monte Carlo (MC) simulations and free-energy calculations. We perform simulations of $N = 3000 - 13000$

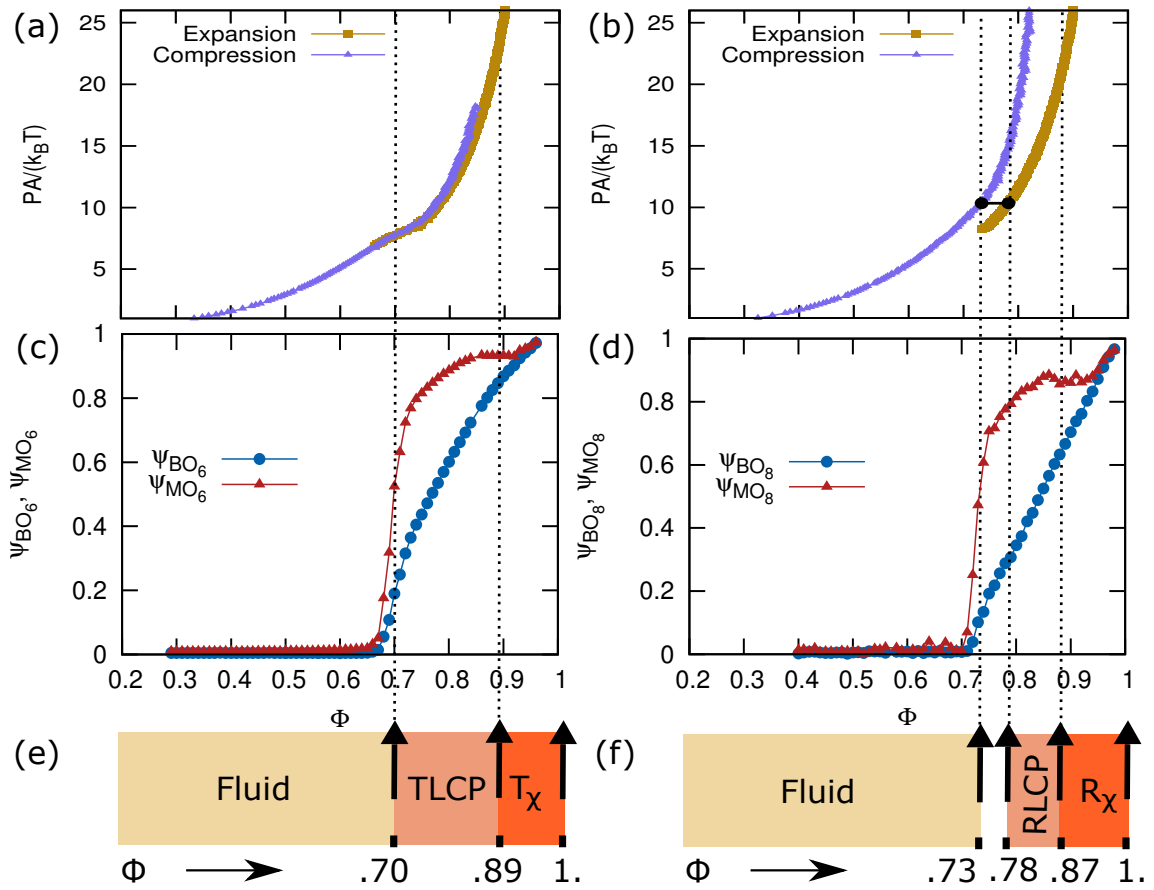

Figure 6.2: (a,b): Equations of state for hard equilateral and right-angled triangles, respectively. Both compression and expansion runs are obtained for a system size of $N = 3200$ particles for equilateral triangles and $N = 1600$ particles for right-angled triangles using rectangular box NPT simulations. (c): Six-fold bond-orientational (ψ_{BO_6}) and molecular orientational (ψ_{MO_6}) order parameters as a function of area fraction ϕ for a system of hard equilateral triangles. Both the order parameters show a transition around $\phi = 0.7$ indicating a phase transition between the liquid and triangular crystal phase. (d): Eight-fold bond-orientational ψ_{BO_8} and molecular orientational ψ_{MO_8} order parameters as a function of area packing fraction ϕ for right-angled triangles. The coexisting densities calculated using free energies for the right-angled triangles are $\phi = 0.733$ and 0.782, and are indicated by the dotted vertical lines. We have used NVT simulations with $N = 12800$ to compute the order parameters for both equilateral and right-angled triangles. Figures (e,f) show the symbolic phase diagram for the two particle shapes using different colors as indicated. TLCP and RLCP represent the triatic and rhombic liquid crystal phase while T_χ and R_χ represent their chiral triangular and rhombic crystal structures, respectively. The white region between the fluid and the RLCP in Fig.6.2(f) indicates the coexistence region.

particles and use the separating axis theorem to detect particle overlaps [84]. We use the candidate close-packed crystal structures in Fig. 6.1 as initial configurations for variable-rectangular-box isothermal-isobaric (NPT) Monte Carlo simulations to determine the equations of state (EOS) from expansion runs. Similarly, we also obtain the EOS by compressing an isotropic fluid at low density.

In order to determine the positional and orientational order at different packing fractions ϕ we measure the n-fold bond-orientational and molecular orientational order parameters. The n-fold bond-orientational order parameter is given by

$$\psi_n = \left| \left\langle \frac{1}{N} \sum_{i=1}^{N} \sum_{j=1}^{nn} \exp\left(\mathbf{i} n \theta_{ij}\right) \right\rangle \right|, \tag{6.1}$$

where θ_{ij} is the angle between the vector, connecting particle i and its nearest neighbor j, and an arbitrary reference axis. Here $nn = 3$, is the number of nearest neighbors. The n-fold molecular orientational order reads

$$\phi_n = \left| \left\langle \frac{1}{N} \sum_{i=1}^{N} \exp\left(\mathbf{i} n \theta_{i}\right) \right\rangle \right|, \tag{6.2}$$

where θ_i is the angle between particles i and the fixed reference axis, here we use the x-axis as the reference axis. Depending on the local symmetry of neighboring particles around a single particle in their corresponding close-packed structures we have chosen $n = 6$ for equilateral triangles and $n = 8$ for right-angled triangles. We calculated these order parameters at different packing fractions using NVT simulations of $N = 12800$ triangles.

We used the Einstein integration method to determine the free energy of the crystal and the Widom insertion technique to determine the free energy of the isotropic fluid. We obtained the free energy per particle f as a function of packing fraction ϕ for the entire density range by thermodynamic integration [70] and used them to determine the coexisting densities . For more details regarding the confining potentials and implementation, see Ref. [164] and Chapter 2.

6.3 Results

In Fig. 6.2, we show the equations of state (EOS) and order parameters for pure equilateral and right-angled triangles. Fig. 6.2(a,b) displays both the compression and expansion EOS. For the equilateral triangles we observed that the system undergoes a continuous phase transition from isotropic (I) to a triatic or triangular liquid crystal phase (TLCP) under compression without showing any hysteresis. With further compressing the triangles we find that the equilateral triangles go to their close-packed triangular crystal structure *via* a continuous phase transition. The right-angled triangles exhibit hysteresis during our NPT compression runs and within our simulation times they never crystallized. However, we find small crystal domains with either two particles and four particles in the unit cell, which are shown in Fig. 6.1(c,d). Before doing the NPT expansion runs we computed free energies as described in Chapter 2 at area packing fraction $\phi = 0.91$ for the right-angled triangles to determine the stable thermodynamic phase among the two candidate crystal structures. We show the excess free energy f_{ex} as a function of number of particles N in Fig. 6.3 for both the candidate crystal structures. We observe that the rhombic lattice with four particles in the unit cell has a lower free energy for all the system sizes we considered and also for the projected free energy of the system in the thermodynamic limit ($N \to \infty$). Using the thermodynamically stable rhombic crystal phase with

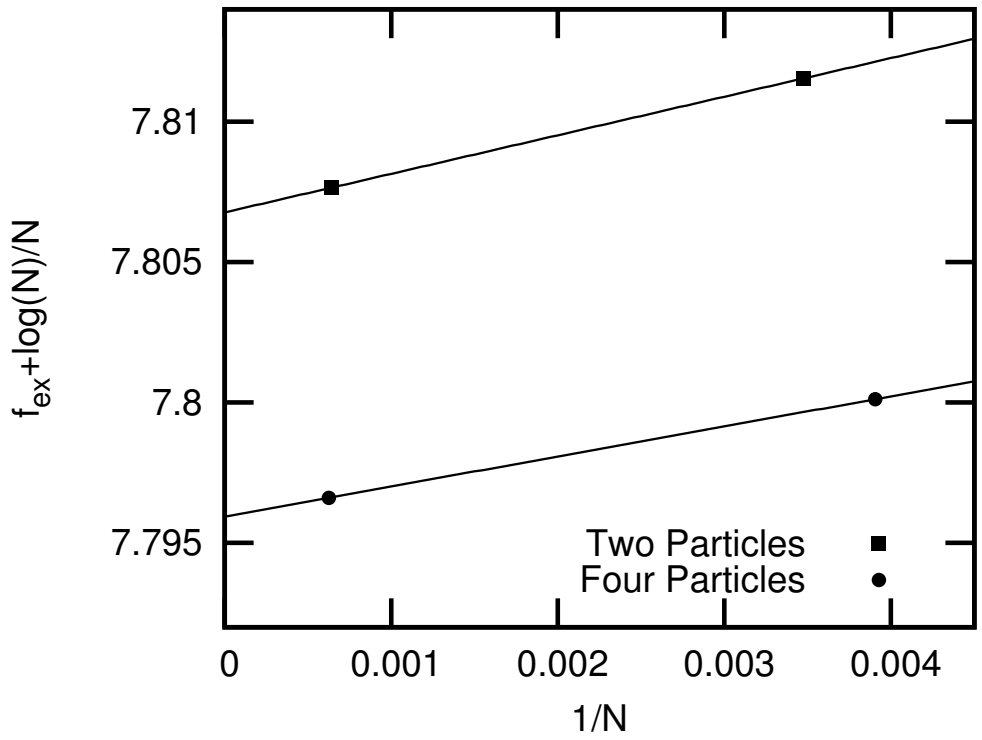

Figure 6.3: Excess free energies $f_{ex} = f - f_{id}$ of the two candidate crystal structures for right-angled triangles as a function of system size at area packing fraction $\phi = 0.91$. Here f is the free energy per particle and f_{id} free energy of the ideal gas at the same packing fraction. We observed that the rhombic lattice with four particles in the unit cell has lower free energy compared to the rhombic lattice with two particles in the unit cell.

four particles in the unit cell we computed the expansion EOS for right-angled triangles shown in Fig. 6.2b. We observed that the rhombic crystal phase with four particles in the unit cell melts continuously into rhombic liquid crystal phase (RLCP), which in turn undergoes a first order phase transition to isotropic fluid phase at lower pressures.

In addition, we also computed the free energies for equilateral triangles at packing fraction $\phi = 0.91$. We used Widom particle insertion technique to determine chemical potential and hence the free energy of the isotropic phase for both the shapes at fixed density. Using thermodynamic integration Eq.2.5 we computed the free energy per particle f as a function of packing fraction and used it to determine the coexisting densities. We first computed the chemical potentials (μ) of both the systems from the free energies and plotted it as a function of scaled pressure as shown in Fig. 6.4. The equilateral triangles does not exhibit any crossover in the chemical potentials as they undergo a continuous phase transition. For the right-angled triangles we find a crossover of the chemical potentials and we find the coexisting packing fractions $\phi_c = [0.733, 0.782]$. We have indicated the coexisting densities for the right-angled triangles in Fig. 6.2b using black points connected by a black line.

The $n-$fold bond-orientational order parameters ψ_{BO_n} and molecular orientational order parameters ψ_{MO_n} as a function of packing fraction obtained from our NVT simulations for both the triangular systems are shown in Fig. 6.2(c,d). For the remainder

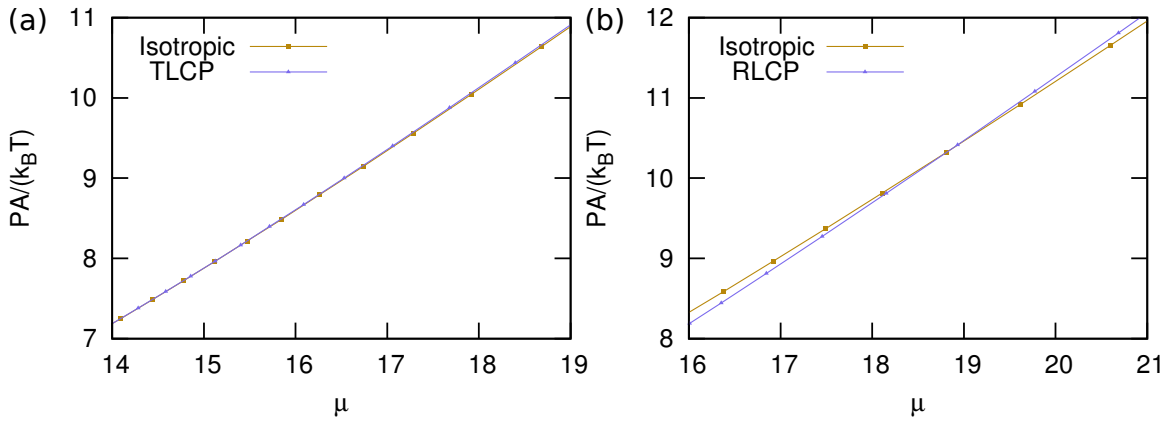

Figure 6.4: We show the chemical potentials (μ) as a function scaled pressure (PA/k_BT) for both the equilateral with two particles in unit cell and right-angled triangles with four particles in the unit cell in (a) and (b), respectively. Here A is the area of the system, k_B is Boltzmann constant and T is the temperature. The chemical potential of the isotropic phase are shown using blue triangles while the triatic liquid crystalline phase (TLCP) and the rhombic liquid crystalline phase (RLCP) are shown using red squares. The chemical potentials crossover for right-angled triangles indicating a first-order phase transition, however equilateral triangles does not show any crossover within the numerical precision of our data.

of the Chapter we have used $n = 6$ and $n = 8$ for equilateral triangles and right-angled triangles, respectively. The bond order in both systems decays faster than the molecular orientational order. The order parameters ψ_{BO_6} and ψ_{MO_6} for the equilateral triangles show that the systems develop bond-orientational and molecular orientational order for $\phi > 0.7$ indicating the isotropic-triatic crystal phase transition. For the right-angles triangles we compute ψ_{BO_8} and ψ_{MO_8} and are shown in Fig. 6.2 (right column). The order parameters ψ_{BO_8} and ψ_{MO_8} for the right-angled triangles show that the system develops bond-orientational and molecular-orientational order for $\phi > 0.73$, which is in agreement with the coexisting packing fraction obtained from free-energy calculations. We indicate different transitions using dotted vertical lines as a guide to the eye across different graphs. In Fig. 6.2(e,f) we summarized the phase behavior using different colors. The T_χ and R_χ represent the chiral triatic phase and the chiral rhombic phases respectively. We will come back to the chiral phases later, we first describe the correlation functions for the triangular systems around their isotropic and crystalline phase transition points.

Correlation functions for translational, bond-orientational and molecular orientational order for various packing fractions around the isotropic-liquid crystal phase transition for both the equilateral triangles and right-angled triangles are shown in Fig. 6.5. All the plots are in log-log scale. The radial distribution function $g(r)$ which indicates the correlations in the translational order decay rapidly in both the isotropic and solid phase. Next we turn to $n-$fold bond-orientational $g_n^{\mathrm{BO}}(r)$ and $n-$fold molecular orientational $g_n^{\mathrm{MO}}(r)$ correlation functions. The bond order and molecular orientational order correlations for area packing fractions above the isotropic-crystal phase transition go to a constant value confirming the emergence of a long-range orientational order within the system sizes we used. The presence of long-range or quasi-long range bond order and molecular orientational correlations in these systems and the absence of long-range order in the

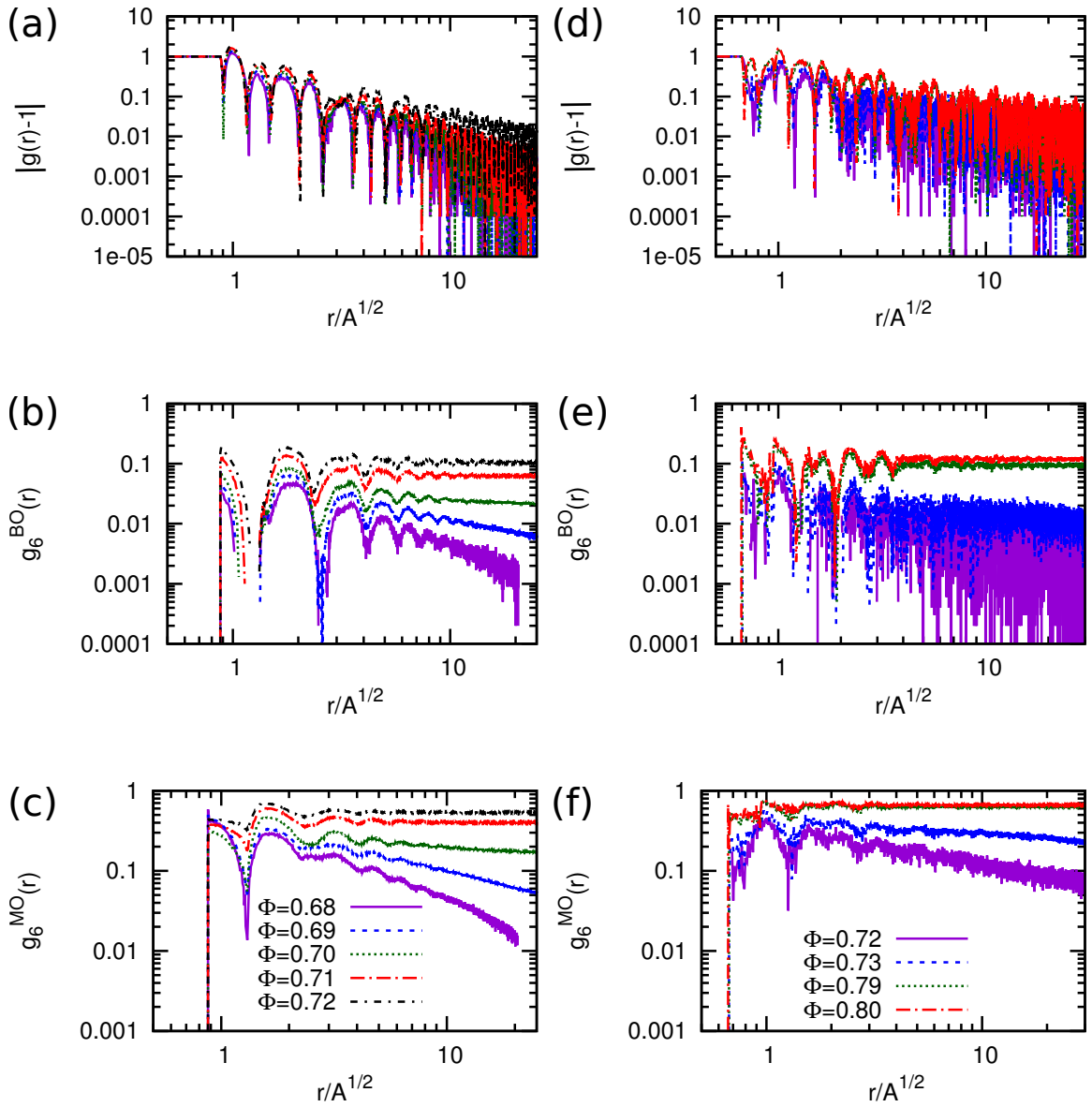

Figure 6.5: Translational, bond-orientational and molecular orientational correlation functions for different packing fractions around $I-LCP$ transition for both the triangular systems. The left column contains the correlation functions for equilateral triangles and the right column is for right-angled isosceles triangles. All the plots are in log-log scale. (a,d): radial distribution function $g(r)-1$ decays algebraically for all the packing fractions.(b,e): $n-$fold bond-orientational order correlation functions where $n=6$ and $n=8$ for equilateral and right-angled triangles respectively. (c,f) $n-$ fold molecular orientational order correlations with similar values for n's as above. Both the bond orders and molecular order show long range correlations for packing fractions greater than $I-LCP$ transition.

translational correlations are characteristic of liquid crystalline phases [11]. However these liquid crystal phases continuously go to a crystalline phase at higher packing fraction without showing any discontinuities in the first derivative of the free energy within the system sizes we used. This allow us to conclude that the triatic and rhombic crystal

phases of equilateral and right-angled triangles, respectively, melt into their respective liquid crystal phases before melting into an isotropic fluid as observed in experiments [11]. All these correlations are computed for a system size $N > 5000$ and $N < 12000$ in an NVT ensemble.

We show the projections of the center of mass of the equilateral triangles in Fig. 6.6 at $\phi = 0.91$ (in the crystal regime), at which we computed the free energies, taken from 20 equilibrated NVT configurations each separated by 100 Monte Carlo sweeps (MCS). Here one MCS contains N translational or rotational Monte Carlo moves. This projection of center of mass of the equilateral triangles from different equilibrated configurations shows that equilateral triangular systems exhibit crystalline phase behavior at $\phi = 0.91$ allowing us to use the Frenkel-Ladd method [70] to compute the free energies.

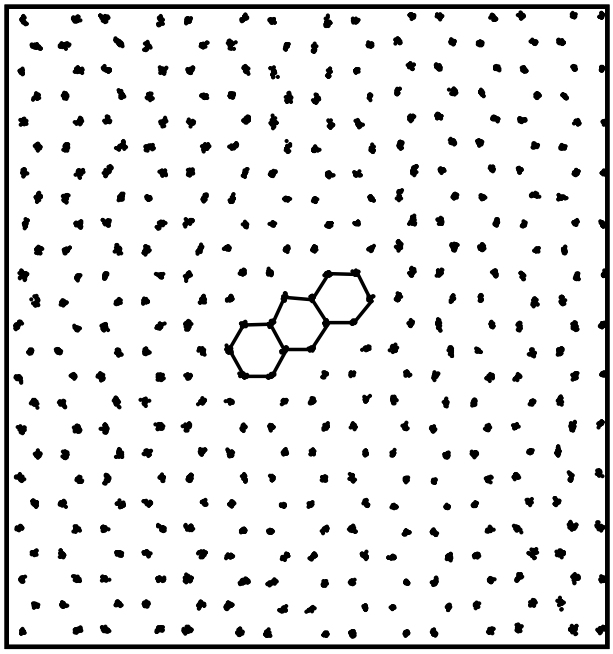

Figure 6.6: Projection of the center of mass of the equilateral triangles taken from 20 different equilibrium configurations at $\phi = 0.91$. The hexagons are drawn to guide the eye to see the inherent hexagonal lattice. We have carved this small picture from a larger system of $N = 5000$ for visual clarity.

The isotropic-to-liquid-crystal phase transition point in equilateral triangles as determined in experiments and simulations [11, 163] are 15% off from our simulation results. Additionally, the EOS shown in Fig. 1 of Ref. [163] does not match with our EOS obtained from isotensic NPT Monte Carlo simulations. We attribute this discrepancy with earlier simulation results [163] to the fact that these molecular dynamics simulations were performed with a fixed box shape, which may lead to non-zero stress. We verified this by Monte Carlo simulations of hard triangles in a fixed box shape, which indeed shows that the isotropic-to-liquid-crystal phase transition happens at lower packing fraction compared to simulations with a variable box shape. The mismatch with the experimental [11] isotropic-liquid-crystal phase transition point is due to the fact that the pair interactions between triangles are much more complex than simple hard particles. The experimental

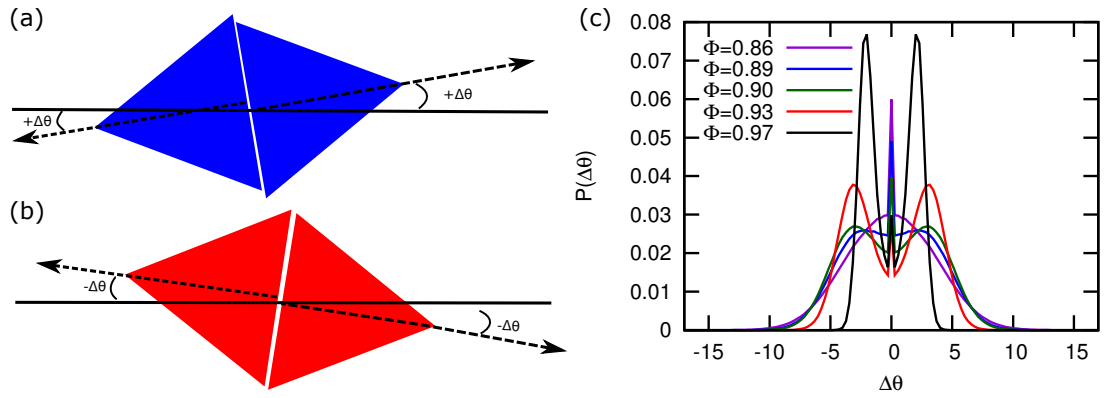

Figure 6.7: Chiral crystal phases. (a,b): Sign notation for anti-clockwise and clockwise orientational displacements $\Delta\theta$ of the molecules around the nematic axis. The nematic axis is indicated with thick black line. The orientation vectors of the triangles are indicated by a dashed line followed by a arrow ahead at the end. The particles which have anti-clockwise orientational displacement are colored blue (+ve sign) and the particles with clockwise orientational displacement are colored red (−ve sign). (b): Probability distribution of the $\Delta\theta$ of the colloidal equilateral hard triangles for $\phi > 0.85$. For $\phi >= 0.89$, we find the distribution developing a tri-modal distribution. Different peaks are explained in the text.

self-assembly of triangles [11] suffer from depletants, charges on the particles and polydispersity. For a detailed discussion see Ref. [165].

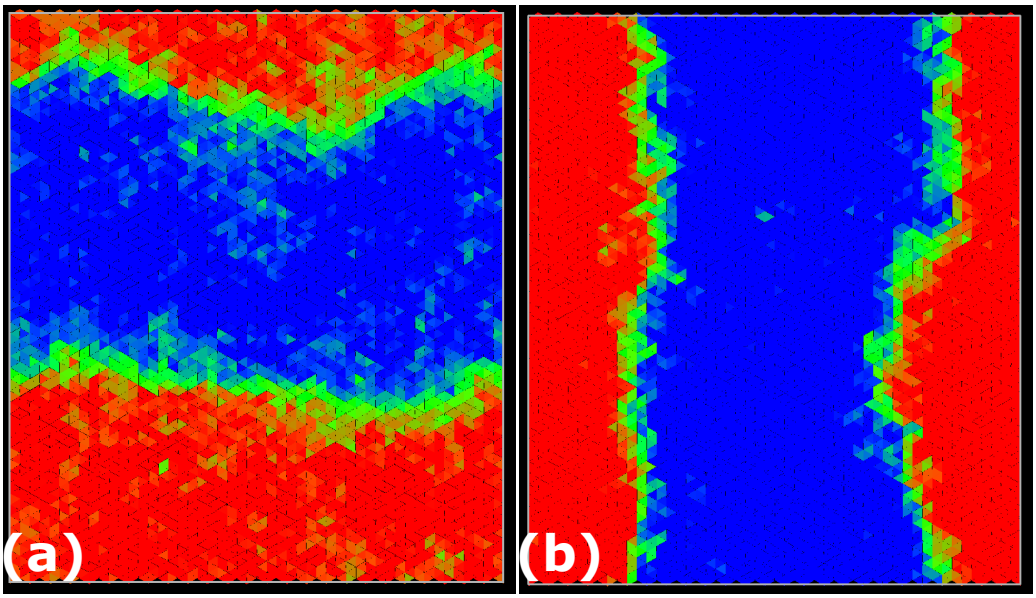

Figure 6.8: Color coded configuration at $\phi = 0.97$ and $\phi = 0.98$ in (a) and (b) respectively for equilateral triangles. The coloring of the individual particles is same as above. Left-handed enantiomers are colored blue while right-handed enantiomers are colored red. The remaining particles are colored green. A clear phase boundary can be seen separating the two enantiomers rich regions.

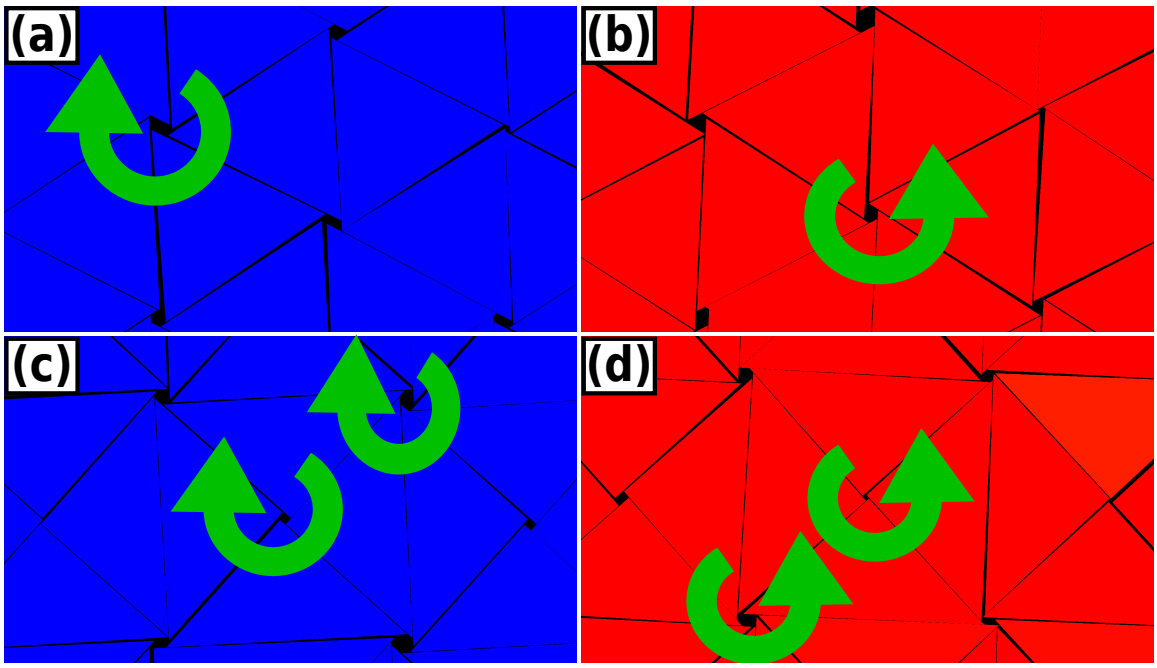

Figure 6.9: Close-up of the chiral enantiomers. The snap shots are taken at $\phi = 0.97$. Top panel shows typical left-handed and right-handed chiral phases from equilateral triangles and the bottom panel contains the same for right-hand triangles. Left-handed enantiomer are colored blue while the right-handed enantiomer are colored red.

Now that we have established the phase behavior of hard equilateral and right-angled triangles at area packing fractions below $\phi < 0.8$, we will turn our attention to the high density phases. We calculate the orientational distribution function of the triangles with respect to a fixed axis (x-axis) as shown in Fig. 6.7a at high density to investigate the local chiral symmetry breaking observed in experiments [11]. In our calculations, the anti-clockwise $\Delta\theta$ are given a positive sign (blue color) while the clockwise orientational displacements around the one of the lattice vectors are given a negative sign (red color) as shown in Fig. 6.7(a,b). The computed probability distributions $p(\Delta\theta)$ are shown in Fig. 6.7(c). Since $p(\Delta\theta) = p(-\Delta\theta)$ we averaged the distribution over the negative and positive side of $\Delta\theta$ to get smooth probability distributions. From Fig. 6.7 it can be noticed that the unimodal distributions splits in to three distinct peaks at $\phi = 0.89$ for equilateral triangles. The central peak corresponds to particles orienting along the lattice vector while the remaining two peaks correspond to a particle which have either anti-clockwise or clockwise orientational displacements. These particle rotations in the entire system gives to a regular lattice of chiral holes as shown in Fig.6.9.

In our NVT simulations with $N = 5000$ and $N <= 12000$ we found that the entire system can have anti-clockwise (positive) or clockwise (negative) twist with equal probabilities. We attribute this phase separation only for some simulations to the large auto correlation times present in simulating the hard particle systems at such a high packing fraction. Typical phase separated configurations are shown in figures 6.8. Similar behavior is observed in right-angled triangles as well. The transition for the right-angled triangles from an achiral to a chiral phase happens at $\phi = 0.87$. A close-up look of

these chiral configurations for both the equilateral and right-angled triangles is shown in Fig. 6.9. We used curved arrows to indicate clockwise and anti-clockwise holes in Fig. 6.9. It is worth mentioning that for long simulation times the system should display either a pure left-handed or right-handed chiral phase, as it costs interfacial free energy to have a phase-separated configuration. Due to the long equilibration times the phase separated system can remain in that state for times greater than our Monte Carlo runs.

In addition, we also computed the lateral shifts between the neighboring triangles at high densities computed by the authors of Ref.[11, 162]. Our results are in agreement with the earlier simulation results of Ref. [162] that there is no split in the probability distributions of these lateral shifts. However, in this work we show that equilateral triangles and right-angled triangles exhibit a regular lattice of chiral holes with either a clockwise twist or anti-clockwise twist at high packing fractions. We also show that at large enough densities the chiral holes can phase separate and coexist. At the same time we would like to remind the reader that the phase separation could be due to the large auto-correlation times of the hard triangles at high packing fractions.

6.4 Conclusions and Summary

In summary, we have computed the phase diagram of hard equilateral and right-handed triangles using large-scale Monte Carlo simulations in combination with free-energy calculations. Using our simulations we show that hard equilateral triangles and hard right-angled triangles undergo a phase transition from an isotropic phase to a triatic and rhombic liquid-crystal phases, respectively. With increasing pressures these liquid crystal phases continuously go to their respective close-packed crystal structures. These close-packed crystalline phases at high enough packing fractions give rise to a regular lattice of chiral holes. The observed chiral enantiomers in both the systems exhibit entropic demixing at large enough densities. It is tempting to say that the observed phase separation is similar to phase separation in 2D Ising model, where the two phases form stripes to minimize the interfacial free energy. Formation of such chiral phases and their phase separation from achiral building blocks in simulations is observed for the first time.

6.5 Acknowledgments

It is a pleasure to thank Dr. Weikai Qi for providing codes to calculate the bond-orientational and molecular orientational order parameters and also for the interesting discussions we had on 2D colloidal systems.

7

Dispersion Relations for Colloidal Crystals with Diffusion

Real crystals exhibit point defects and interstitials. The presence of these defects leads to diffusion in the system, which affect the mechanical properties of solids. Elastic coefficients and dispersion relations of crystals are computed generally using a microscopic approach which needs the displacements of the particles around their mean position as input. However, this method fails if there is diffusion in the solid. Using a recently developed theoretical technique based on the Fourier space components of the density fluctuations near a lattice point, we compute the dispersion relations of colloidal crystals which exhibit diffusion. We compare our results with density functional theory and find agreement with those results. Our results suggest that the new approach based on density fluctuations is a robust method to compute dispersion relations for real crystals.

7.1 Introduction

Studying the mechanical properties of colloidal systems is important to understand the stability of colloidal systems. Recent developments in confocal microscopy techniques have enabled experimentalists to image colloidal systems with high precision both in time and space. Simultaneously, single-particle tracking algorithms are developed to track various anisotropic particles [90]. Combining these two, one can track single-particle motion in a colloidal solid. Using the displacement information of individual particles in a colloidal crystal one can compute the dispersion relations, normal modes and elastic coefficients. Experimental works which have combined these two developments have successfully determined the thermal and mechanical properties of colloidal systems [166–169].

Point defects and interstitials are quite common in colloidal solids. For the well-studied hard-particle crystals, the defect density of vacancies and interstitials is as low as 10^{-4} and 10^{-8}, respectively [94]. With increasing polydispersity the density of interstitials can increase to 0.02 in hard-sphere crystals [95]. Interstitials in hard-sphere crystals are found to be quite mobile leading to diffusion in these colloidal crystals. In addition, recent simulation studies of hard cubes and truncated cubes have shown that cube-like particles exhibit large defect densities as high as 0.064 close to coexistence [49, 79, 80]. These colloidal crystals with high defect concentrations exhibit diffusion. Similarly, colloidal particles with soft repulsive potentials like super-Gaussian core particles exhibit diffusion in their multiple-occupancy crystal phases [170–173]. The presence of diffusion in these colloidal crystals affect their thermal and mechanical properties and also makes it difficult to compute the dispersion relations using the classical microscopic theory which needs the particles confined to their local cages. To overcome this limitation of the classical microscopic theory, we employ here a recently developed theoretical technique [174] to compute the dispersion relations for crystals even in the presence of diffusion. We use two test systems to compute the phonon dispersion relations using both the methods and show that the new technique is impervious to diffusion.

The rest of this chapter is organized as follows. First we describe the two microscopic approaches to compute the dispersion relations. Later we use these methods to compute the dispersion relations for hard-sphere systems and for the Gaussian-core model (GCM). We then discuss the results and compare our results with those obtained from a density functional theory. We will not discuss the density functional theory as it is beyond the scope of this thesis but refer the interested reader to Ref. [175].

7.2 Theory and Methods

To compute the dispersion relations for a system we first need to determine the dynamical matrix $\mathscr{D}$. The eigenvalues $\lambda(\mathbf{q})$ of the dynamical matrix as a function of the wave vector $\mathbf{q}$ are called dispersion relations. The dynamical matrix $\mathscr{D}$ is inversely proportional to the correlations in the displacement field $\mathbf{u}$. The two different methods we use in this Chapter to compute the dispersion relations differ in the definition of the displacement field. We describe both the methods below:

7.2.1 Method 1

According to the traditional microscopic approach [169], the dynamical matrix reads

$$\mathscr{D}(\mathbf{q}) = \frac{k_{\mathrm{B}}T}{\langle \mathbf{u_q}^* \mathbf{u_q} \rangle}, \tag{7.1}$$

where the angular bracket $\langle . \rangle$ indicate the canonical ensemble average, k_{B} is the Boltzmann constant, T is the temperature, $\mathbf{q}$ is the wave vector and

$$\mathbf{u_q}(t) = \frac{1}{\sqrt{N}} \sum_{i=1}^{N} \exp[i\mathbf{q}.\bar{\mathbf{r}}_i]\mathbf{u}_i(t), \tag{7.2}$$

is the Fourier transform of

$$\mathbf{u}_i\,(t) = \mathbf{r}_i\,(t) - \bar{\mathbf{r}}_i, \tag{7.3}$$

is the displacement vector of the i^{th} particle from its mean position $\bar{\mathbf{r}}_i$ at a given time t, $\mathbf{r}_i\,(t)$ is the current position of the particle and N is the number of particles. To have meaningful results, this method demands to have fixed and non-diverging $\bar{\mathbf{r}}_i$ which in turn needs the particle displacements $\mathbf{u}_i\,(t)$ confined to a cage as can be seen from Eq. 7.2.

7.2.2 Method 2

To overcome the problem of diffusing particles in a crystal while computing the dispersion relations a new theory based on density fluctuations is proposed by Fuchs *et al.* [176, 177]. According to this theory the dynamical matrix is given as follows:

$$\mathscr{D}(\mathbf{q}) = \frac{k_{\mathrm{B}}T}{\langle \delta\mathbf{u_q}^* \delta\mathbf{u_q} \rangle}, \tag{7.4}$$

where the displacement field $\mathbf{u_q} = \delta\mathbf{u_q} - \langle \mathbf{u_q} \rangle$, in equilibrium the ensemble average of the displacements $\langle \mathbf{u_q} \rangle = 0$. The displacement field

$$\mathbf{u_q}(t) = i\mathscr{N}^{-1} \sum_{\mathbf{g}} n^*_{\mathbf{g}} \mathbf{g} \delta\rho_{\mathbf{g}}(\mathbf{q}, t)/\sqrt{V}, \tag{7.5}$$

where V is the volume of the system and $\mathscr{N} = \sum_{\mathbf{g}} |n_{\mathbf{g}}|^2 \, \mathbf{gg}$ is a normalization matrix and $n_{\mathbf{g}}$ are the Debye waller factors given as

$$n_{\mathbf{g}} = \frac{1}{V} \sum_{i=1}^{N} \langle \exp\left(-i\mathbf{g}.\mathbf{r}_i\right) \rangle\,, \tag{7.6}$$

and

$$\delta\rho_{\mathbf{g}} = \rho(\mathbf{g} + \mathbf{q}, t) - n_{\mathbf{g}} V \delta_{\mathbf{q},0}, \tag{7.7}$$

is the Fourier transform of the spatial fluctuations in density ρ close to the reciprocal lattice vector $\mathbf{g}$. The Fourier transform of the density reads

$$\rho\,(\mathbf{k}, t) = \int d^3\mathbf{r}\; e^{-i\mathbf{k}.\mathbf{r}} \rho(\mathbf{r}, t), \tag{7.8}$$

and the density is given as

$$\rho(\mathbf{r},t)=\sum_{i}^{N}\delta(\mathbf{r}-\mathbf{r}_i(t)). \tag{7.9}$$

Here, the general wave vector $\mathbf{k}$ is divided up into the reciprocal lattice vector $\mathbf{g}$ and wave vector $\mathbf{q}$, which lies within the first Brillouin zone.

For more details about the theory see Ref. [177].

Unlike Method 1, Method 2 does not depend on the mean position of a particle. For this method we only need the density fluctuations in Fourier space close to the reciprocal lattice vectors. In the presence of local defects or in the case of particles diffusing from one lattice site to another only the magnitudes of $n_{\mathbf{g}}$ and $\delta\rho(\mathbf{g})$ will be affected. As a result this method is useful to compute the dispersion relations for real crystals which exhibit diffusion either in the presence of vacancies or interstitials.

The aim of this project is to compute the dispersion relations for crystals using both the methods explained above and compare them with respect to each other. For this purpose we use two different test systems, namely the hard-sphere model and the Gaussian core model. Pure hard spheres exhibit no diffusion in the crystalline phase, while the Gaussian core model exhibit tremendous amount of diffusion in the multiple occupancy crystal phase [170–173, 178]. Finally, we also compare our results obtained for Gaussian core model with those calculated by a time-dependent density functional theory.

7.3 Results

To compute the dispersion relations we first need to compute the displacement fields defined in Eq. 7.2 and Eq. 7.5 and then later calculate the ensemble average of the displacement correlations $\langle \mathbf{u_q}^{*}\mathbf{u_q}\rangle$. Here we determine $\langle \mathbf{u_q}^{*}\mathbf{u}_q\rangle$ using Monte Carlo simulations. We generate an ensemble of equilibrium configurations of the systems under consideration using standard NVT Monte Carlo simulations (where N is the number of particles, V is the volume of the system and T is the temperature). These configurations are then used to compute the ensemble average of the displacement correlations. We have taken care to avoid correlated configurations by taking configurations which are separated by 100 Monte Carlo sweeps, where one Monte Carlo sweep contains N particle translational moves.

More detailedly, in the case of Method 1 we first compute the mean position of particles $\bar{\mathbf{r}}_i$. Later, we compute the displacements of individual particles $\mathbf{u}_i$ using Eq. 7.3 and substitute it into Eq. 7.2 to compute the Fourier transform of displacement field $\mathbf{u_q}$ for one configuration. Now using this displacement field $\mathbf{u_q}$ for all the equilibrium configurations we compute $\langle \mathbf{u_q}^{*}\mathbf{u_q}\rangle$ and substitute it into Eq. 7.1 to compute the dynamical matrix $\mathscr{D}(q)$. We diagonalize the dynamical matrix $\mathscr{D}(\mathbf{q})$ and determine the eigenvalues $\lambda(\mathbf{q})$, which are the dispersion relations.

For Method 2, we initially calculate the Debye waller factors $n_{\mathbf{g}}$ and the density fluctuations directly in Fourier space $\delta\rho_{\mathbf{g}}$ using Eq. 7.6 and Eq. 7.8, respectively, where we use 27 reciprocal lattice vectors $\mathbf{g}$ which lie with in the first Brillouin zone and $\mathbf{q}$ is the directional wave vector of interest. By substituting these two quantities into Eq. 7.5 we obtain the displacement field $\mathbf{u_q}$ for each configuration separately. Using the displacement fields

for all the equilibrium configurations we compute the ensemble average of the displacement fields $\langle \mathbf{u_q}^* \mathbf{u_q} \rangle$ (here $\delta \mathbf{u_q} = \mathbf{u_q}$, since $\langle \mathbf{u_q} \rangle = 0$ in equilibrium) and then substitute it into Eq. 7.4 to compute $\mathscr{D}(\mathbf{q})$ and determine the dispersion relations as mentioned above.

7.3.1 Hard Spheres

Hard-sphere systems are well studied and serve as a perfect model systems to test new methods in statistical physics. Here we use hard spheres as the first test system to compute dispersion relations. We first generate an ensemble of configurations using NVT Monte Carlo simulations and then use the configurations to compute the displacement fields according to Eq. 7.2 and 7.5. We have used 1500 equilibrated configurations to reduce the statistical error in computing the displacement field. Later, we compute the dynamical matrix $\mathscr{D}$ according to the two methods as described above and then calculate their respective eigenvalues $\lambda(\mathbf{q})$.

We show the dispersion relations for a hard-sphere system in Fig. 7.1 at a packing fraction $\phi = 0.57$ and $N = 4000$. We show $\omega_j a = \sqrt{\lambda_j} a$ as a function of wave vector qa in Fig.7.1, where ω_j is the frequency with the subscript j indicating the polarization and a is the lattice constant of the face centered crystal (fcc) structure of hard spheres. Our results in Fig. 7.1 show that the dispersion relations computed using both methods agree with each other for all the directions. We used system sizes $N = 4000$ and $32,000$ to compute the dispersion relations and found no finite-size effects in the dispersion relation calculations.

7.3.2 Gaussian-Core Particles

The next system we use is the Gaussian-core model. The pair potential between two Gaussian-core particles is given by

$$U(r) = \epsilon \exp\left[-(r/\sigma)^n\right], \tag{7.10}$$

where ϵ and σ set the energy and length scale in the system. Here we set both of them to unity while $n = 4$ in our studies. Simulations and theoretical phase behavior studies of Gaussian-core particles can be found in Refs. [170–173, 178].

Gaussian-core particles exhibit rich phase behavior like stable multiple occupancy crystal phases, *i.e.,* more than one particle at a lattice site, face centered and body centered cubic crystals [171]. Here we calculate the phonon dispersion relations for the multiple occupancy face centered cubic crystal of Gaussian-core particles using the methods described above. In a multiple occupancy crystal of Gaussian-core particles appreciable diffusion is present, which makes this a perfect test system for Method 2 to compute the dispersion relations.

We have generated an ensemble of configurations for the Gaussian-core particles at temperature $k_{\mathrm{B}}T/\epsilon = 0.01$, density $\rho\sigma^3 = 0.5$ and the average density of particles per lattice site is $\rho_l \sigma^3 = 1.01407$ using NVT Monte Carlo simulations. We have used $N = 4056$ particles on $N_L = 4000$ lattice points for these simulations. As simulating Gaussian-core particles is computationally expensive we have restricted ourselves to small system sizes. We show in Fig. 7.2 the dispersion relations for the Gaussian-core particles using

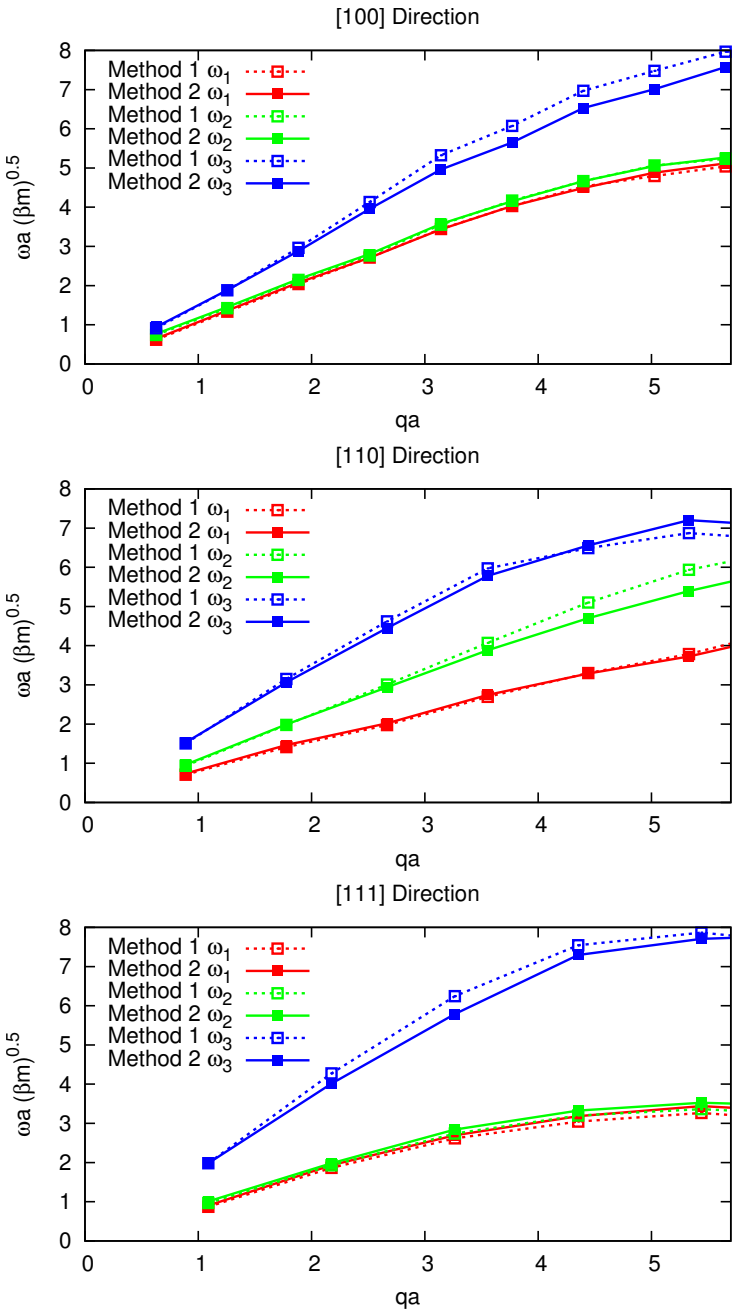

Figure 7.1: Dispersion relations for a defect-free face centered cubic crystal phases of hard spheres at packing fraction $\phi = 0.57$ using the two methods as described in the main text. Different direction vectors for which we computed the dispersion relations are indicated on the top of each plot. We indicate different frequencies by different colors as indicated in the legend. The open squares denote the results obtained using Method 1 and the filled squares correspond to Method 2. We have rescaled the dispersion relations with $(\beta m)^{0.5}$ to make them dimensionless, where $m = 1$ is the mass of the particle, $\beta = 1/k_{\mathrm{B}}T$. Here k_{B} is Boltzmann's constant and T is the temperature and β is set to unity in our simulations.

both methods. Method 1 fails to calculate physically meaningful dispersion relations.

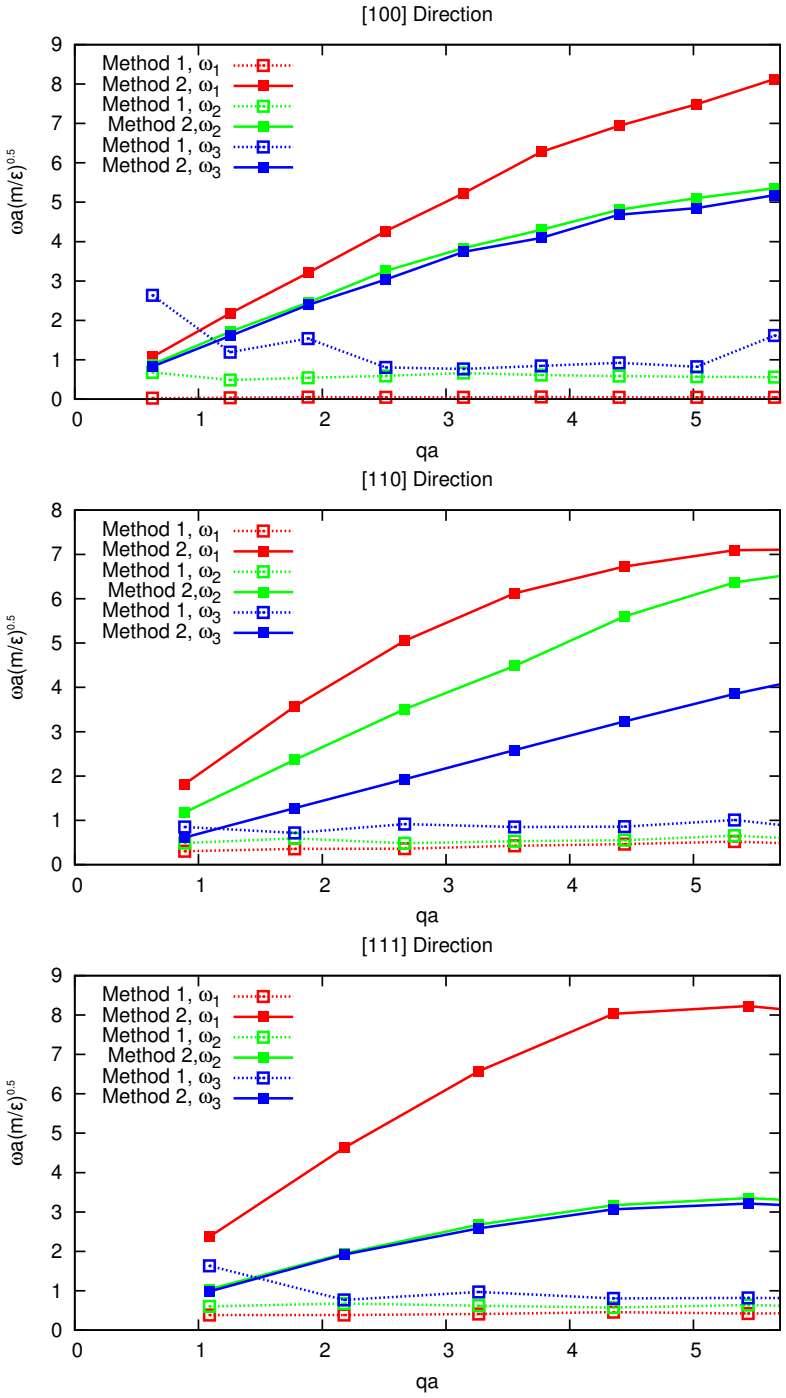

Figure 7.2: Dispersion relations for a multiple occupancy face centered cubic crystal phases of Gaussian-core particles using the two methods as described in the main text. Here the density $\rho\sigma^3 = 0.5$, the average density at a lattice site $\rho_l\sigma^3 = 1.01407$, temperature $k_{\mathrm{B}}T/\epsilon = 0.01$, number of particles $N = 4056$ distributed over $N_L = 4000$ lattice sites. The real space method fails to calculate the dispersion relations while the reciprocal space method successfully computes the dispersion relations even in the presence of diffusion. Different polarizations are indicated on the top of each plot.

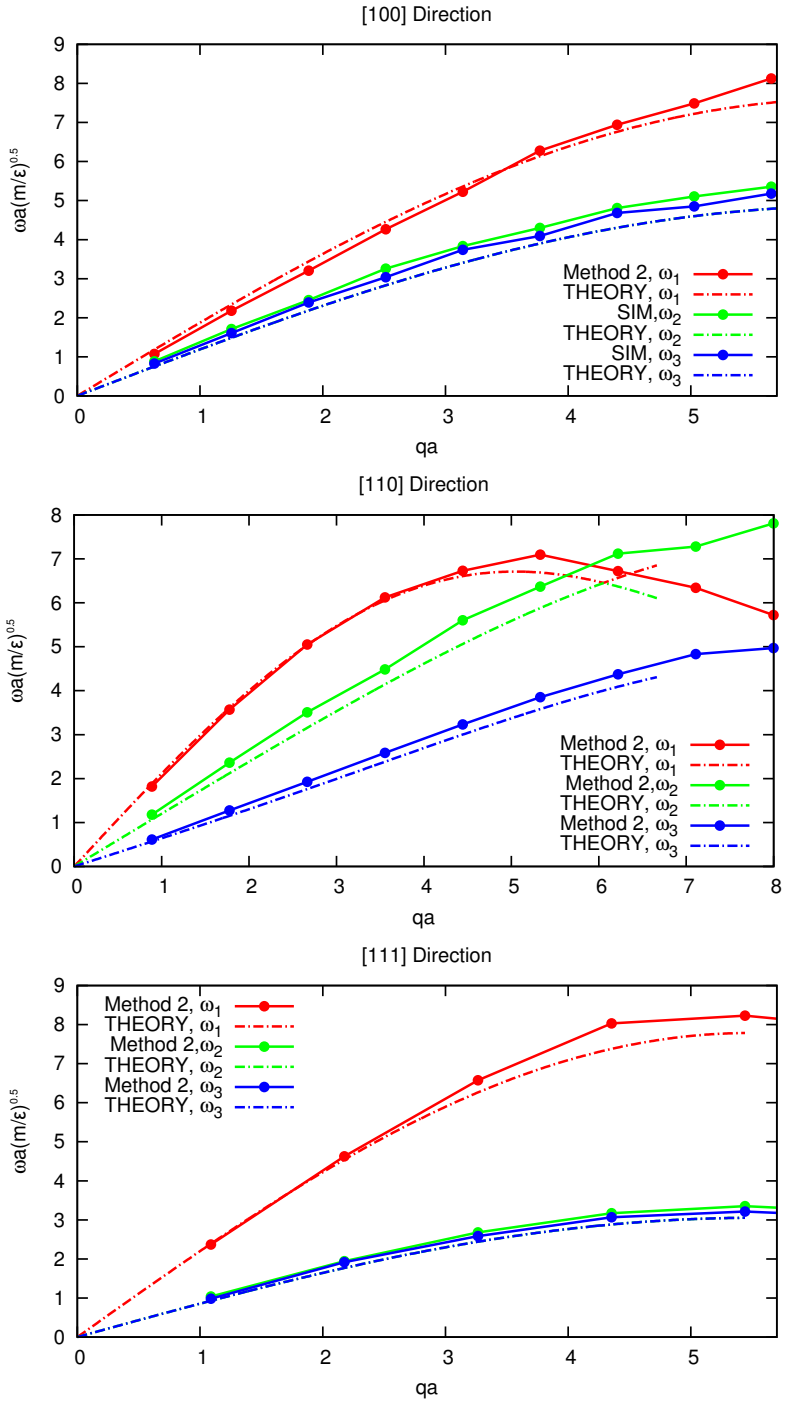

Figure 7.3: Dispersion relations for a multiple occupancy face centered cubic crystal of Gaussian-core particles from simulations using Method 2 and density functional theory [175]. Here the density $\rho\sigma^3 = 0.5$, the average density at a lattice site $\rho_l\sigma^3 = 1.01407$, temperature $k_{\mathrm{B}}T/\epsilon = 0.01$, number of particles $N = 4056$ distributed over $N_L = 4000$ lattice sites. Both the simulation results and density functional theory results are shown as explained in legend. Different polarizations are indicated on the top of each plot.

However Method 2 succeeds in calculating dispersion relations even in the presence of diffusion.

In the multiple occupancy crystal, the number of particles sitting at a given lattice site fluctuates even though the global density is fixed. These particles move from one lattice site to the other by hopping. Because of this diffusion the average position of the particle $\bar{\mathbf{r}}_i$ diverges. The average position $\bar{\mathbf{r}}_i$ needs to be a conserved quantity in Eq. 7.2, to calculate accurately the displacement field $\mathbf{u_q}$ in Eq. 7.2 for Method 1. Because of this reason the dispersion relations computed by Method 1 failed, while the second method is impervious to the diffusion and depends only on the density fluctuations at each lattice site. Method 2 is hence successful in computing the dispersion relations as shown in Fig. 7.2.

In addition, we also compare our results for Gaussian-core particles obtained using Method 2 with those obtained from a density functional theory [175] in Fig. 7.3. Our results are in good agreement with the theoretical results. More details about the density functional theory can be found in Ref. [175]. We will not discuss the density functional theory here as it is out of scope for this thesis.

7.4 Conclusions

Using a recently developed theory to compute dispersion relations [176] and Monte Carlo simulations we have computed the dispersion relations for colloidal crystals with diffusion. We compared this method with the traditional microscopic approach and showed that the traditional approach fails in computing the dispersion relations if there is diffusion in the crystals under investigation. Our results are in agreement with the result obtained using a density functional theory. This new method can be used in confocal microscopy to compute the elastic coefficients and the dispersion relations for colloidal crystals without worrying about the diffusion of the particles. In addition, the computer codes written to compute the dispersion relations can be used to obtain the dispersion relations for experimental data sets very easily.

7.5 Acknowledgments

It is a pleasure to thank Tadeus Ras, Johannes Haering, and Prof. dr. Matthias Fuchs for their collaboration on this project and for the long discussions on the theoretical methods we used in this Chapter.

.

References

[1] A. D. McNaught. *IUPAC compendium of chemical terminology.* Blackwell Science Inc. (Hoboken), 2nd edition, 1997.

[2] A. Einstein, *Über die von der molekularkinetischen theorie der wärme geforderte bewegung von in ruhenden flüssigkeiten suspendierten teilchen.* Ann. Phys. (Leipz.), 17:549, 1905.

[3] J. Perrin, *Mouvement Brownien et réalité moléculaire.* Ann. Chim. Phys., 18:5, 1909.

[4] J. Perrin. *Les atomes.* Alacan (Paris), 1st edition, 1913.

[5] S. C. Glotzer and M. J. Solomon, *Anisotropy of building blocks and their assembly into complex structures.* Nature Mater., 6:557, 2007.

[6] M. Ozaki, S. Kratohvil, and E. Matijevic, *Formation of mondispersed spindle-type hematite particles.* J. Colloid Interface Sci., 102:146, 1984.

[7] F. M. van der Kooij, K. Kassapidou, and H. N. W. Lekkerkerker, *Liquid crystal phase transitions in suspensions of polydisperse plate-like particles.* Nature, 406:868, 2000.

[8] A. Kuijk, A. van Blaaderen, and A. Imhof, *Synthesis of monodisperse, rodlike silica colloids with tunable aspect ratio.* J. Am. Chem. Soc., 133:2346, 2011.

[9] P. A. Buining, C. Pathmamanoharan, J. B. H. Jansen, and H. N. W. Lekkerkerker, *Preparation of colloidal boehmite needles by hydrothermal treatment of aluminum alkoxide precursors.* J. Am. Chem. Soc., 74:1303, 1991.

[10] N. Malikova, I. Pastoriza-Santos, M. Schierhorn, N. A. Kotov, and L. M. Liz-Marzán, *Layer-by-layer assembled mixed spherical and planar gold nanoparticles: Control of interparticle interactions.* Langmuir, 18:3694, 2002.

[11] K. Zhao, R. Bruinsma, and T. G. Mason, *Local chiral symmetry breaking in triatic liquid crystals.* Nat Commun, 3:801, 2012.

[12] K. Zhao, R. Bruinsma, and T. G. Mason, *Entropic crystal-crystal transitions of brownian squares.* Proceedings of the National Academy of Sciences, 108:2684, 2011.

[13] Y. Sun and Y. Xia, *Shape-controlled synthesis of gold and silver nanoparticles.* Science, 298:2176, 2002.

[14] Y. Zhang, F. Lu, D. van der Lelie, and O. Gang. Phys. Rev. Lett., 107:135701, 2011.

[15] E. C. Greyson, J. E. Barton, and T. W. Odom, *Tetrahedral zinc blende tin sulfide nano- and microcrystals.* Small, 2:368, 2006.

[16] J. Henzie, M. Grünwald, A. Widmer-Cooper, P. L. Geissler, and P. Yang, *Self-assembly of uniform polyhedral silver nanocrystals into densest packings and exotic superlattices.* Nature Mater., 11:131, 2012.

[17] L. Rossi, S. Sacanna, W. T. M. Irvine, P. M. Chaikin, D. J. Pine, and A. P. Philipse, *Cubic crystals from cubic colloids.* Soft Matter, 7:4139, 2011.

[18] W. van der Stam, A. P. Gantapara, Q. A. Akkerman, G. Soligno, J. D. Meeldijk, R. van Roij, M. Dijkstra, and C. de Mello Donega, *Self-assembly of colloidal hexagonal bipyramid- and bifrustum-shaped ZnS nanocrystals into two-dimensional superstructures.* Nano Letters, 14:1032, 2014.

[19] T. S. Ahmadi, Z. L. Wang, T. C. Green, A. Henglein, and M. El-Sayed, *Shape-controlled synthesis of colloidal platinum nanoparticles.* Science, 272:1924, 1996.

[20] L. Manna, D. J. Milliron, A. Meisel, E. C. Scher, and A. P. Alivisatos, *Controlled growth of tetrapod-branched inorganic nanocrystals.* Nature Mater., 2:382, 2003.

[21] G. Zhou, M. Lü, Z. Xiu, S. Wang, H. Zhang, Y. Zhou, and S. Wang, *Controlled synthesis of high-quality PbS star-shaped dendrites, multipods, truncated nanocubes, and nanocubes and their shape evolution process.* J. Phys. Chem. B, 110:6543, 2006.

[22] N. Zhao and L. M. Qi, *Low-temperature synthesis of star-shaped PbS nanocrystals in aqueous solutions of mixed cationic/anionic surfactants.* Adv. Mater., 18:359, 2006.

[23] T. Huang, Q. A. Zhao, J. Y. Xiao, and L. M. Qi, *Controllable self-assembly of PbS nanostars into ordered structures: Close-packed arrays and patterned arrays.* ACS Nano, 4:4707, 2010.

[24] G. A. DeVries, M. Brunnbauer, Y. Hu, A. M. Jackson, B. Long, B. T. Neltner, O. Uzun, B. H. Wunsch, and F. Stellacci, *Divalent metal nanoparticles.* Science, 315:358, 2007.

[25] K.-H. Roh, D. C. Martin, and J. Lahann, *Biphasic janus particles with nanoscale anisotropy.* Nat. Mater., 4:759, 2005.

[26] B. G. P. van Ravensteijn, M. Kamp, A. van Blaaderen, and W. K. Kegel, *General route toward chemically anisotropic colloids.* Chemistry of Materials, 25:4348, 2013.

[27] E. Matijevic, *Monodispersed metal (hydrous) oxides - a fascinating field of colloid science.* Acc. Chem. Res., 14:22, 1981.

[28] X. Xia and Y. Xia, *Symmetry breaking during seeded growth of nanocrystals.* Nano Lett., 12:6038, 2012.

[29] Y. Xia, B. Gates, and Z. Li, *Self-assembly approaches to three-dimensional photonic crystals.* Adv. Mater., 13:109, 2001.

[30] Y. Wang, Y. Zheng, C. Z. Huang, and Y. Xia, *Synthesis of ag nanocubes 18âĂŞ32 nm in edge length: The effects of polyol on reduction kinetics, size control, and reproducibility.* Journal of the American Chemical Society, 135:1941, 2013.

[31] J. Zeng, C. Zhu, J. Tao, M. Jin, H. Zhang, Z.-Y. Li, Y. Zhu, and Y. Xia, *Controlling the nucleation and growth of silver on palladium nanocubes by manipulating the reaction kinetics.* Angewandte Chemie International Edition, 51:2354, 2012.

[32] A. S. Barnard, X. M. Lin, and L. A. Curtiss, *Equilibrium morphology of face-centered cubic gold nanoparticles >3 nm and the shape changes induced by temperature.* J. Phys. Chem. B, 109:24465, 2005.

[33] X. Zhang, C. Dong, J. Zapien, S. Ismathullakhan, Z. Kang, J. Jie, X. Zhang, J. Chang, C.-S. Lee, and S.-T. Lee, *Polyhedral organic microcrystals: From cubes to rhombic dodecahedra.* Angew. Chem. Int. Ed., 48:9121, 2009.

[34] H.-L. Wu, C.-H. Kuo, and M. H. Huang, *Seed-mediated synthesis of gold nanocrystals with systematic shape evolution from cubic to trisoctahedral and rhombic dodecahedral structures.* Langmuir, 26:12307, 2010.

[35] W. H. Evers, B. Goris, S. Bals, M. Casavola, J. de Graaf, R. v. Roij, M. Dijkstra, and D. Vanmaekelbergh, *Low-dimensional semiconductor superlattices formed by geometric control over nanocrystal attachment.* Nano Letters, 13:2317, 2013.

[36] Y. Ma, W. Li, E. C. Cho, Z. Li, T. Yu, J. Zeng, Z. Xie, and Y. Xia, *Au@Ag core-shell nanocubes with finely tuned and well-controlled sizes, shell thicknesses, and optical properties.* ACS Nano, 4:6725, 2010.

[37] L. Rossi, S. Sacanna, W. T. M. Irvine, P. M. Chaikin, D. J. Pine, and A. P. Philipse, *Cubic crystals from cubic colloids.* Soft Matter, 7:4139, 2011.

[38] Y. Bai, T. Yang, Q. Gu, G. Cheng, and R. Zheng, *Shape control mechanism of cuprous oxide nanoparticles in aqueous colloidal solutions.* Powder Technol., 227:35, 2012.

[39] J. Zhang, Z. Luo, B. Martens, Z. Quan, A. Kumbhar, N. Porter, Y. Wang, D.-M. Smilgies, and J. Fang, *Reversible kirkwoodâĂŞalder transition observed in pt3cu2 nanoctahedron assemblies under controlled solvent annealing/drying conditions.* J. Am. Chem. Soc., 134:14043, 2012.

[40] M. Eguchi, D. Mitsui, H.-L. Wu, R. Sato, and T. Teranishi, *Simple reductant concentration-dependent shape control of polyhedral gold nanoparticles and their plasmonic properties.* Langmuir, 28:9021, 2012.

[41] Z. Quan, W. Siu Loc, C. Lin, Z. Luo, K. Yang, Y. Wang, H. Wang, Z. Wang, and J. Fang, *Tilted face-centered-cubic supercrystals of pbs nanocubes.* Nano Lett., 12:4409, 2012.

[42] J. J. Choi, K. Bian, W. J. Baumgardner, D.-M. Smilgies, and T. Hanrath, *Interface-induced nucleation, orientational alignment and symmetry transformations in nanocube superlattices.* Nano Lett., 12:4791, 2012.

[43] Y. Zhang, F. Lu, D. van der Lelie, and O. Gang, *Continuous phase transformation in nanocube assemblies.* Phys. Rev. Lett., 107:135701, 2011.

[44] S. Torquato and Y. Jiao, *Dense packings of the Platonic and Archimedian solids.* Nature Lett., 460:876, 2009.

[45] J. de Graaf, R. van Roij, and M. Dijkstra, *Dense regular packings of irregular nonconvex particles.* Phys. Rev. Lett., 107:155501, 2011.

[46] U. Betke and M. Henk, *Densest lattice packings of 3-polytopes.* Comput. Geom., 16:157, 2000.

[47] C. B. Murray, C. R. Kagan, and M. G. Bawendi, *Synthesis and characterization of monodisperse nanocrystals and close-packed nanocrystal assemblies.* Annu. Rev. Mater. Sci., 30:545, 2000.

[48] H. Minkowski, *Dichteste gitterförmige lagerung kongruenter körper.* Nachr. K. Ges. Wiss. Göttingen, 11:311, 1904.

[49] A. P. Gantapara, J. de Graaf, R. van Roij, and M. Dijkstra, *Phase diagram and structural diversity of a family of truncated cubes: Degenerate close-packed structures and vacancy-rich states.* Phys. Rev. Lett., 111:015501, 2013.

[50] P. F. Damasceno, M. Engel, and S. C. Glotzer, *Predictive self-assembly of polyhedra into complex structures.* Science, 337:453, 2012.

[51] J. Burnet. *Greek Philosophy, Part 1: Thales to Plato.* Macmillan (London), 1st edition, 1914.

[52] J. V. Field, *Rediscovering the archimedean polyhedra: Piero della francesca, luca pacioli, leonardo da vinci, albrecht dürer, daniele barbaro, and johannes kepler.* Arch. Hist. Exact. Sci., 50:241, 1997.

[53] W. H. Evers, H. Friedrich, L. Filion, M. Dijkstra, and D. Vanmaekelbergh, *Observation of a ternary nanocrystal superlattice and its structural characterization by electron tomography.* Angew. Chem. Int. Ed., 48:9655, 2009.

[54] W. H. Evers, B. de Nijs, L. Filion, S. Castillo, M. Dijkstra, and D. Vanmaekelbergh, *Entropy-driven formation of binary semiconductor-nanocrystal superlattices.* Nano Lett., 10:4235, 2010.

[55] X. Ye, J. A. Millan, M. Engel, J. Chen, B. T. Diroll, S. C. Glotzer, and C. B. Murray, *Shape alloys of nanorods and nanospheres from self-assembly.* Nano Letters, 13:4980, 2013.

[56] J. Hansen and I. McDonald. *Theory of Simple Liquids.* Academic Press, London, 1986.

[57] M. Dijkstra, R. van Roij, and R. Evans, *Phase diagram of highly asymmetric binary hard-sphere mixtures.* Phys. Rev. E, 59:5744, 1999.

[58] M. Dijkstra, R. van Roij, and R. Evans, *Direct simulation of the phase behavior of binary hard-sphere mixtures: test of the depletion potential description.* Phys. Rev. Lett., 82:117, 1999.

[59] A. P. Hynninen, L. Filion, and M. Dijkstra, *Stability of ls and ls2 crystal structures in binary mixtures of hard and charged spheres.* J. Chem. Phys., 131:064902, 2009.

[60] A. Yethiraj and A. van Blaaderen, *A colloidal model system with an interaction tunable from hard sphere to soft and dipolar.* Nature, 421:513, 2003.

[61] L. Onsager, *The effects of shape on the interaction of colloidal particles.* Annals of the New York Academy of Sciences, 51:627, 1949.

[62] A. Gast and W. Russel, *Simple ordering in complex fluids.* Physics Today, 51:24, 1998.

[63] B. Alder and T. Wainwright, *Phase transition for a hard sphere system.* J. Chem. Phys., 27:1208, 1957.

[64] W. Wood and J. D. Jacobson, *Preliminary results from a recalculation of the monte carlo equation of state of hard spheres.* J. Chem. Phys., 27:1207, 1957.

[65] B. Alder, W. Hoover, and D. Young, *Studies in molecular dynamics. v. high-density equation of state and entropy for hard disks and spheres.* J. Chem. Phys., 49:3688, 1968.

[66] D. Frenkel, H. Lekkerkerker, and A. Stroobans, *Thermodynamic stability of a smectic phase in a system of hard rods.* Nature, 332:822, 1988.

[67] P. F. Damasceno, M. Engel, and S. C. Glotzer, *Crystalline assemblies and densest packings of a family of truncated tetrahedra and the role of directional entropic forces.* ACS Nano, 6:609, 2012.

[68] M. Marechal, A. Cuetos, B. Martinez-Haya, and M. Dijkstra, *Phase behavior of hard colloidal platelets using free energy calculations.* J. Chem. Phys., 134:094501, 2011.

[69] M. Marechal and M. Dijkstra, *Phase behavior and structure of colloidal bowl-shaped particles: Simulations.* Phys. Rev. E, 82:031405, 2010.

[70] D. Frenkel and B. Smit. *Understanding Molecular Simulation.* Academic Press, Inc., Orlando, FL, USA, 2nd edition, 2001.

[71] J. de Graaf, L. Filion, M. Marechal, R. Roij, and M. Dijkstra, *Crystal-structure prediction via the floppy-box monte carlo algorithm: Method and application to hard (non)convex particles.* J. Chem. Phys., 137:214101, 2012.

[72] L. Filion, M. Marechal, B. van Oorschot, D. Pelt, F. Smallenburg, and M. Dijkstra, *Efficient method for predicting crystal structures at finite temperature: Variable box shape simulations.* Phys. Rev. Lett., 103:188302, 2009.

[73] D. Frenkel and A. J. C. Ladd, *New monte carlo method to compute the free energy of arbitrary solids. application to the fcc and hcp phases of hard spheres.* J. Chem. Phys., 81:3188, 1984.

[74] E. G. Noya, C. Vega, J. P. K. Doye, and A. A. Louis, *Phase diagram of model anisotropic particles with octahedral symmetry.* J. Chem. Phys., 127:054501, 2007.

[75] B. Widom, *Some topics in the theory of fluids.* J. Chem. Phys., 39:2808, 1963.

[76] R. D. Batten, F. H. Stillinger, and S. Torquato, *Phase behavior of colloidal superballs: Shape interpolation from spheres to cubes.* Phys. Rev. E, 81:061105, 2010.

[77] R. Ni, A. P. Gantapara, J. de Graaf, R. van Roij, and M. Dijkstra, *Phase diagram of colloidal hard superballs: from cubes via spheres to octahedra.* Soft Matter, 8:8826, 2012.

[78] U. Agarwal and F. A. Escobedo, *Mesophase behaviour of polyhedral particles.* Nature Mater., 10:230, 2011.

[79] F. Smallenburg, L. Filion, M. Marechal, and M. Dijkstra, *Vacancy-stabilized crystalline order in hard cubes.* Proc. Natl. Acad. Sci. USA, 109:17886, 2012.

[80] M. Marechal, U. Zimmermann, and H. Löwen, *Freezing of parallel hard cubes with rounded edges.* J. Chem. Phys., 136:144506, 2012.

[81] R. D. Batten, F. H. Stillinger, and S. Torquato, *Phase behavior of colloidal superballs: Shape interpolation from spheres to cubes.* Phys. Rev. E, 81:061105, 2010.

[82] A. Fortini, M. Dijkstra, M. Schmidt, and P. P. F. Wessels, *Wall-fluid and liquid-gas interfaces of model colloid-polymer mixtures by simulation and theory.* Phys. Rev. E, 71:051403, 2005.

[83] A. Donev. *Jammed Packings of Hard Particles.* PhD thesis, Princeton University, 2006.

[84] D. Eberly. *Intersection of convex objects: The method of separating axes.* `http://www.geometrictools.com/`, 2008.

[85] D. Gottwald, G. Kahl, and C. N. Likos, *Predicting equilibrium structures in freezing processes.* J. Chem. Phys., 122:204503, 2005.

[86] L. Filion and M. Dijkstra, *Prediction of binary hard-sphere crystal structures.* Phys. Rev. E, 79:046714, 2009.

[87] H. T. Stokes, D. M. Hatch, and B. J. Campbell. *FindSym software package.* `http://stokes.byu.edu/isotropy.html`, 2007.

[88] C. for Computational Materials Science. *Database of molecular prototypes corresponding to the 230 existing space groups.* `http://cst-www.nrl.navy.mil/lattice/index.html`, 2008.

[89] V. Thapar and F. A. Escobedo, *Localized orientational order chaperones the nucleation of rotator phases in hard polyhedral particles.* Phys. Rev. Lett., 112:048301, 2014.

[90] B. Liu, T. H. Besseling, M. Hermes, A. F. Demirörs, A. Imhof, and A. van Blaaderen, *Switching plastic crystals of colloidal rods with electric fields.* Nat Commun, 5(3092), 2014.

[91] J. Timmermans, *Plastic crystals: a historical review.* J. Phys. Chem. Solids, 18:1, 1961.

[92] J. Sherwood. *The Plastically Crystalline State: Orientationally Disordered Crystals.* 1979.

[93] B. Mirtich, *Fast and accurate computation of polyhedral mass properties.* Journal of Graphics Tools, 1:31, 1996.

[94] S. Pronk and D. Frenkel, *Point defects in hard-sphere crystals.* The Journal of Physical Chemistry B, 105:6722, 2001.

[95] S. Pronk and D. Frenkel, *Large effect of polydispersity on defect concentrations in colloidal crystals.* J. Chem. Phys., 120:6764, 2004.

[96] D. Frenkel and B. Smit. *Understanding Molecular Simulation: From Algorithms to Applications.* Academic Press, 2002.

[97] A.-P. Hynninen, J. H. J. Thijssen, E. C. M. Vermolen, M. Dijkstra, and A. van Blaaderen, *Self-assembly route for photonic crystals with a bandgap in the visible region.* Nature Mater., 6:202, 2007.

[98] A. Haji-Akbari, M. Engel, A. S. Keys, X. Zheng, R. G. Petschek, P. Palffy-Muhoray, and S. C. Glotzer, *Disordered, quasicrystalline and crystalline phases of densely packed tetrahedra.* Nature (London), 462:773, 2009.

[99] S. Torquato and Y. Jiao, *Dense packings of the platonic and archimedean solids.* Nature (London), 460:876, 2009.

[100] T. C. Hales and S. P. Ferguson, *The Kepler conjecture.* Discrete Comput. Geom., 36:5, 2006.

[101] J. de Graaf, R. van Roij, and M. Dijkstra, *Dense regular packings of irregular nonconvex particles.* Phys. Rev. Lett., 107:155501, 2011.

[102] Y. Jiao, F. H. Stillinger, and S. Torquato, *Optimal packings of superballs.* Phys. Rev. E, 79:041309, 2009.

[103] Y. Jiao, F. H. Stillinger, and S. Torquato, *Erratum: Optimal packings of superballs [Phys. Rev. E 79, 041309 (2009)].* Phys. Rev. E, 84:069902, 2011.

[104] M. Marechal, A. Cuetos, B. Martínez-Haya, and M. Dijkstra, *Phase behavior of hard colloidal platelets using free energy calculations.* J. Chem. Phys., 134:094501, 2011.

[105] C. Vega and P. A. Monson, *Plastic crystal phases of hard dumbbells and hard spherocylinders.* J. Chem. Phys., 107:2696, 1997.

[106] M. Marechal and M. Dijkstra, *Stability of orientationally disordered crystal structures of colloidal hard dumbbells.* Phys. Rev. E, 77:061405, 2008.

[107] P. Bolhuis and D. Frenkel, *Tracing the phase boundaries of hard spherocylinders.* J. Chem. Phys., 106:666, 1997.

[108] P. G. Bolhuis, D. Frenkel, S.-C. Mau, and D. A. Huse, *Entropy difference between crystal phases.* Nature, 388:235, 1997.

[109] W. L. Miller and A. Cacciuto, *On the phase behavior of hard aspherical particles.* J. Chem. Phys., 133:234903, 2010.

[110] W. L. Miller, B. Bozorgui, and A. Cacciuto, *Crystallization of hard aspherical particles.* J. Chem. Phys., 132:134901, 2010.

[111] H. Minkowski, *Dichteste gitterförmige lagerung kongruenter körper.* Nachr. K. Ges. Wiss. Göttingen, 11:311, 1904.

[112] See Supplemental Material of Ni *et al.* (Soft Matter 8:8826, 2012) for the movie of plastic bcc crystal formed by superballs with $q = 0.7$ at packing fraction $\phi = 0.54$..

[113] Y. Jiao, F. H. Stillinger, and S. Torquato, *Optimal packings of superballs.* Phys. Rev. E, 79:041309, 2009.

[114] J. L. Aragones and C. Vega, *Plastic crystal phases of simple water models.* J. Chem. Phys., 130:244504, 2009.

[115] D. Talapin, J.-S. Lee, M. Kovalenko, and E. Shevchenko, *Prospects of colloidal nanocrystals for electronic and optoelectronic applications.* Chemical Reviews, 110:389, 2010.

[116] D. Vanmaekelbergh, *Self-assembly of colloidal nanocrystals as route to novel classes of nanostructured materials.* Nano Today, 6:419, 2011.

[117] T. Paik and C. Murray, *Shape-directed binary assembly of anisotropic nanoplates: A nanocrystal puzzle with shape-complementary building blocks.* Nano Letters, 13:2952, 2013.

[118] Z. Nie, A. Petukhova, and E. Kumacheva, *Properties and emerging applications of self-assembled structures made from inorganic nanoparticles.* Nature Nanotechnology, 5:15, 2010.

[119] Y. Shirasaki, G. Supran, M. Bawendi, and V. BuloviÄĞ, *Emergence of colloidal quantum-dot light-emitting technologies.* Nature Photonics, 7:13, 2013.

[120] L. Sun, J. Choi, D. Stachnik, A. Bartnik, B.-R. Hyun, G. Malliaras, T. Hanrath, and F. Wise, *Bright infrared quantum-dot light-emitting diodes through inter-dot spacing control.* Nature Nanotechnology, 7:369, 2012.

[121] F. Pisanello, L. Martiradonna, P. Spinicelli, A. Fiore, J. Hermier, L. Manna, R. Cingolani, E. Giacobino, M. De Vittorio, and A. Bramati, *Dots in rods as polarized single photon sources.* Superlattices and Microstructures, 47:165, 2010.

[122] E. Talgorn, Y. Gao, M. Aerts, L. Kunneman, J. Schins, T. Savenije, M. Van Huis, H. Van Der Zant, A. Houtepen, and L. Siebbeles, *Unity quantum yield of photogenerated charges and band-like transport in quantum-dot solids.* Nature Nanotechnology, 6:733, 2011.

[123] J. Tang, K. Kemp, S. Hoogland, K. Jeong, H. Liu, L. Levina, M. Furukawa, X. Wang, R. Debnath, D. Cha, K. Chou, A. Fischer, A. Amassian, J. Asbury, and E. Sargent, *Colloidal-quantum-dot photovoltaics using atomic-ligand passivation.* Nature Materials, 10:765, 2011.

[124] A. Ip, S. Thon, S. Hoogland, O. Voznyy, D. Zhitomirsky, R. Debnath, L. Levina, L. Rollny, G. Carey, A. Fischer, K. Kemp, I. Kramer, Z. Ning, A. Labelle, K. Chou, A. Amassian, and E. Sargent, *Hybrid passivated colloidal quantum dot solids.* Nature Nanotechnology, 7:577, 2012.

[125] R. Wang, J. Feser, J.-S. Lee, D. Talapin, R. Segalman, and A. Majumdar, *Enhanced thermopower in pbse nanocrystal quantum dot superlattices.* Nano Letters, 8:2283, 2008.

[126] Y. Kang, X. Ye, J. Chen, L. Qi, R. Diaz, V. Doan-Nguyen, G. Xing, C. Kagan, J. Li, R. Gorte, E. Stach, and C. Murray, *Engineering catalytic contacts and thermal stability: Gold/iron oxide binary nanocrystal superlattices for co oxidation.* Journal of the American Chemical Society, 135:1499, 2013.

[127] J. Urban, D. Talapin, E. Shevchenko, C. Kagan, and C. Murray, *Synergism in binary nanocrystal superlattices leads to enhanced p-type conductivity in self-assembled pbte/ag2te thin films.* Nature Materials, 6:115, 2007.

[128] E. Shevchenko, D. Talapin, N. Kotov, S. O'Brien, and C. Murray, *Structural diversity in binary nanoparticle superlattices.* Nature, 439:55, 2006.

[129] J. Heath, *Materials science: Synergy in a superlattice.* Nature, 445:492, 2007.

[130] M. Boneschanscher, W. Evers, W. Qi, J. Meeldijk, M. Dijkstra, and D. Vanmaekelbergh, *Electron tomography resolves a novel crystal structure in a binary nanocrystal superlattice.* Nano Letters, 13:1312, 2013.

[131] W. Evers, B. Goris, S. Bals, M. Casavola, J. De Graaf, R. Roij, M. Dijkstra, and D. Vanmaekelbergh, *Low-dimensional semiconductor superlattices formed by geometric control over nanocrystal attachment.* Nano Letters, 13:2317, 2013.

[132] Z. Chen and S. O'Brien, *Structure direction of ii-vi semiconductor quantum dot binary nanoparticle superlattices by tuning radius ratio.* ACS Nano, 2:1219, 2008.

[133] M. Grzelczak, J. Vermant, E. Furst, and L. Liz-MarzÃąn, *Directed self-assembly of nanoparticles.* ACS Nano, 4:3591, 2010.

[134] C. Donegá, *Synthesis and properties of colloidal heteronanocrystals.* Chemical Society Reviews, 40:1512, 2011.

[135] S. Torquato and Y. Jiao, *Dense packings of the platonic and archimedean solids.* Nature, 460:876, 2009.

[136] T. Nguyen, E. Jankowski, and S. Glotzer, *Self-assembly and reconfigurability of shape-shifting particles.* ACS Nano, 5:8892, 2011.

[137] Z. Quan and J. Fang, *Superlattices with non-spherical building blocks.* Nano Today, 5:390, 2010.

[138] E. R. Chen, M. Engel, and S. C. Glotzer, *Dense crystalline dimer packings of regular tetrahedra.* Discrete Comput. Geom., 44:253, 2010.

[139] A. Haji-Akbari, M. Engel, and S. C. Glotzer, *Phase diagram of hard tetrahedra.* J. Chem. Phys., 135:194101, 2011.

[140] E. R. Chen, D. Klotsa, M. Engel, P. F. Damasceno, and S. C. Glotzer, *Complexity in surfaces of densest packings for families of polyhedra.* Phys. Rev. X, 4:011024, 2014.

[141] G. van Anders, N. K. Ahmed, R. Smith, M. Engel, and S. C. Glotzer, *Entropically patchy particles: Engineering valence through shape entropy.* ACS Nano, 8:931, 2014.

[142] D. Reifsnyder, X. Ye, T. Gordon, C. Song, and C. Murray, *Three-dimensional self-assembly of chalcopyrite copper indium diselenide nanocrystals into oriented films.* ACS Nano, 7:4307, 2013.

[143] T. Gordon, T. Paik, D. Klein, G. Naik, H. Caglayan, A. Boltasseva, and C. Murray, *Shape-dependent plasmonic response and directed self-assembly in a new semiconductor building block, indium-doped cadmium oxide (ico).* Nano Letters, 13:2857, 2013.

[144] W. Qi, J. de Graaf, F. Qiao, S. Marras, L. Manna, and M. Dijkstra, *Ordered two-dimensional superstructures of colloidal octapod-shaped nanocrystals on flat substrates.* Nano Letters, 12:5299, 2012.

[145] K. Miszta, J. De Graaf, G. Bertoni, D. Dorfs, R. Brescia, S. Marras, L. Ceseracciu, R. Cingolani, R. Van Roij, M. Dijkstra, and L. Manna, *Hierarchical self-assembly*

of suspended branched colloidal nanocrystals into superlattice structures. Nature Materials, 10:872, 2011.

[146] W. Du, X. Qian, M. Xiaodong, Q. Gong, H. Cao, and J. Yin, *Shape-controlled synthesis and self-assembly of hexagonal covellite (cus) nanoplatelets.* Chemistry - A European Journal, 13:32417, 2007.

[147] W. Baumgardner, K. Whitham, and T. Hanrath, *Confined-but-connected quantum solids via controlled ligand displacement.* Nano Letters, 13:3225, 2013.

[148] X. Ye, J. Chen, M. Engel, J. Millan, W. Li, L. Qi, G. Xing, J. Collins, C. Kagan, J. Li, S. Glotzer, and C. Murray, *Competition of shape and interaction patchiness for self-assembling nanoplates.* Nature Chemistry, 5:466, 2013.

[149] F. Pietra, F. Rabouw, W. Evers, D. Byelov, A. Petukhov, C. De Mello DonegÃą, and D. Vanmaekelbergh, *Semiconductor nanorod self-assembly at the liquid/air interface studied by in situ gisaxs and ex situ tem.* Nano Letters, 12:5515, 2012.

[150] L. Carbone, C. Nobile, M. De Giorgi, F. Della Sala, G. Morello, P. Pompa, M. Hytch, E. Snoeck, A. Fiore, I. Franchini, M. Nadasan, A. Silvestre, L. Chiodo, S. Kudera, R. Cingolani, R. Krahne, and L. Manna, *Synthesis and micrometer-scale assembly of colloidal cdse/cds nanorods prepared by a seeded growth approach.* Nano Letters, 7:2942, 2007.

[151] J. Rivest, S. Swisher, L.-K. Fong, H. Zheng, and A. Paul Alivisatos, *Assembled monolayer nanorod heterojunctions.* ACS Nano, 5:3811, 2011.

[152] T. Wang, J. Zhuang, J. Lynch, O. Chen, Z. Wang, X. Wang, D. LaMontagne, H. Wu, Z. Wang, and Y. Cao, *Self-assembled colloidal superparticles from nanorods.* Science, 338:358, 2012.

[153] J. de Graaf, M. Dijkstra, and R. van Roij, *Adsorption trajectories and free-energy separatrices for colloidal particles in contact with a liquid-liquid interface.* J. Chem. Phys., 132:164902, 2010.

[154] P. Pieranski, *Two-dimensional interfacial colloidal crystals.* Physical Review Letters, 45:569, 1980.

[155] E. Plum, J. Zhou, J. Dong, V. A. Fedotov, T. Koschny, C. M. Soukoulis, and N. I. Zheludev. Phys. Rev. B, 79:035407, 2009.

[156] J. B. Pendry, *A chiral route to negative refraction.* Science, 306:1353, 2004.

[157] A. Chutinan and S. Noda, *Spiral three-dimensional photonic-band-gap structure.* Phys. Rev. B, 57:R2006, 1998.

[158] J. P. Straley, *Frank elastic constants of the hard-rod liquid crystal.* Phys. Rev. A, 8:2181, 1973.

[159] T. Odijk, *Pitch of a polymer cholesteric.* J. Phys. Chem., 91:6060, 1987.

[160] S. Belli, S. Dussi, M. Dijkstra, and R. van Roij, *Density functional theory for chiral nematic liquid crystals.* Phys. Rev. E., 90:020503, 2014.

[161] K. Zhao and T. G. Mason, *Twinning of rhombic colloidal crystals.* J. Am. Chem. Soc., 134:18125, 2012.

[162] S. P. Carmichael and M. S. Shell, *A simple mechanism for emergent chirality in achiral hard particle assembly.* J. Chem. Phys., 139, 2013.

[163] M. Benedict and J. F. Maguire, *Molecular dynamics simulation of nanomaterials using an artificial neural net.* Phys. Rev. B, 70:174112, 2004.

[164] W. Qi, J. de Graaf, F. Qiao, S. Marras, L. Manna, and M. Dijkstra, *Phase diagram of octapod-shaped nanocrystals in a quasi-two-dimensional planar geometry.* J. Chem. Phys., 138:154504, 2013.

[165] K. Mayoral and T. G. Mason, *Entropic chiral symmetry breaking in self-organized two-dimensional colloidal crystals.* Soft Matter, 10:4471, 2014.

[166] A. Ghosh, V. K. Chikkadi, P. Schall, J. Kurchan, and D. Bonn, *Density of states of colloidal glasses.* Phys. Rev. Lett., 104:248305, 2010.

[167] A. Ghosh, R. Mari, V. Chikkadi, P. Schall, J. Kurchan, and D. Bonn, *Density of states of colloidal glasses and supercooled liquids.* Soft Matter, 6:3082, 2010.

[168] D. Kaya, N. L. Green, C. E. Maloney, and M. F. Islam, *Normal modes and density of states of disordered colloidal solids.* Science, 329:656, 2010.

[169] C. L. Klix, F. Ebert, F. Weysser, M. Fuchs, G. Maret, and P. Keim, *Glass elasticity from particle trajectories.* Phys. Rev. Lett., 109:178301, 2012.

[170] B. M. Mladek, P. Charbonneau, and D. Frenkel, *Phase coexistence of cluster crystals: Beyond the gibbs phase rule.* Phys. Rev. Lett., 99:235702, 2007.

[171] B. M. Mladek, P. Charbonneau, C. N. Likos, D. Frenkel, and G. Kahl, *Multiple occupancy crystals formed by purely repulsive soft particles.* Journal of Physics: Condensed Matter, 20:494245, 2008.

[172] B. M. Mladek, G. Kahl, and C. N. Likos, *Computer assembly of cluster-forming amphiphilic dendrimers.* Phys. Rev. Lett., 100:028301, 2008.

[173] B. M. Mladek, D. Gottwald, G. Kahl, M. Neumann, and C. N. Likos, *Formation of polymorphic cluster phases for a class of models of purely repulsive soft spheres.* Phys. Rev. Lett., 96:045701, 2006.

[174] C. Walz and M. Fuchs, *Displacement field and elastic constants in nonideal crystals.* Phys. Rev. B, 81:134110, 2010.

[175] J. Haering and M. Fuchs, *Density functional theory.* Private Communication, 2014.

[176] M. F. Christof Walz, Grzegorz Szamel, *On the coarse-grained density and compressibility of a non-ideal crystal.* arXiv, page 1206.6183.

[177] M. Fuchs, *Elastic properties of colloidal solids with disorder.* arXiv, page 1209.0389, 2012.

[178] K. Zhang, P. Charbonneau, and B. M. Mladek, *Reentrant and isostructural transitions in a cluster-crystal former.* Phys. Rev. Lett., 105:245701, 2010.

[179] W. Qi, A. P. Gantapara, and M. Dijkstra, *Two-stage melting induced by dislocations and grain boundaries in monolayers of hard spheres.* Soft Matter, 10:5449, 2014.

Summary

A colloidal dispersion consists of insoluble microscopic particles that are suspended in a solvent. Typically, a colloid is a particle for which at least one of its dimension is within the size range of a nanometer to a micron. Due to collisions with much smaller solvent molecules, colloids perform Brownian motion, which allows them to explore all possible configurations available to them. Colloidal particles suspended in a fluid interact with each other in addition to the background interaction with the solvent atoms/molecules. As a result colloids can exhibit rich phase behavior similar to that of atomic and molecular systems. For example, colloids can self-assemble, not only into gas, liquid, solid phases, but also nematic, smectic, biaxial, hexatic phases. The type of phases that can emerge in a colloidal system depends not only on the interaction potential between the colloidal particles but also on the shape of the colloidal particle itself.

In this thesis we study the effect of colloid shape on its phase behavior. In particular, we investigate the phase behavior of experimentally available polyhedral particles using Monte Carlo simulations and free-energy calculations both in bulk and at an interface.

In Chapter 2, we present our study on the thermodynamic phase behavior of a family of truncated hard cubes, where the shape evolves smoothly from a cube *via* a cuboctahedron to an octahedron. We use Monte Carlo simulations and free-energy calculations to establish the full phase diagram. Surprisingly, this phase diagram exhibits a remarkable diversity of non-close-packed and close-packed crystal structures, including a fully degenerate crystal structure and vacancy-stabilized crystal phase, all depending sensitively on the precise particle shape. In addition, we examine the nature of the plastic-crystal phases that appear for intermediate densities and levels of truncation. Our results show that the orientational distribution function of plastic crystals of hard anisotropic particles can be highly anisotropic and can be strongly peaked for specific orientations. These orientational directions depend not only on the crystal structure of the particle but also on the shape of the particle. Our results show that the nature of plastic crystals of hard particles is different from that of plastic crystals formed of particles with long-range interactions. Our results allowed us to probe the relation between phase behavior and building-block shape and to further the understanding of rotator phases.

In addition to the phase behavior, we also study and compute the equilibrium vacancy concentration of these truncated cubes in Chapter 3. We determine the free energies of truncated cubes as a function of vacancy concentration using a modified Einstein integration method. From our calculations we find that the equilibrium vacancy concentration of truncated cubes increases with increasing truncation at a fixed packing fraction $\phi = 0.56$. Using simple cell theory calculations we show that the increase in vacancy concentrations with truncation is due to the increase in orientational entropy with truncation.

We study the phase behavior of rounded truncated cubes, namely superballs, in Chapter 4. In this Chapter, we use Monte Carlo simulations and free-energy calculations to determine the phase diagram of colloidal hard superballs, of which the shape interpolates between cubes and octahedra via spheres. We found not only a stable face-centered cubic (fcc) plastic-crystal phase for near-spherical particles, but also a stable body-centered

cubic (bcc) plastic crystal close to the octahedron shape. Moreover, coexistence of these two plastic crystals is observed with a substantial density gap. The plastic fcc and bcc crystals are, however, both unstable in the cube and octahedron limit, suggesting that the low asphericity ratio of the superballs in combination with local curvature, i.e. rounded corners and curved faces, of superballs plays an important role in stabilizing the rotator phases. In addition, we observe a two-step melting phenomenon for hard octahedra, in which a Minkowski crystal melts into a metastable bcc plastic crystal before melting into the fluid phase.

In Chapter 5, we present a combined theoretical and simulation study on the self-assembly of colloidal hexagonal bipyramid- and hexagonal bifrustum-shaped nanoparticles in two dimensions. The self-assembled structures as obtained in simulations are in good agreement with those observed in experiments on colloidal nanocrystals. Our results show that the superlattice formation is driven primarily by minimization of the interfacial free energies and maximization of the packing densities. Moreover, our results show that truncation of the tips of hexagonal bipyramids by as little as 5% is sufficient to change the symmetry of the resulting superlattice from hexagonal to tetragonal. This demonstrates that precise shape control is of crucial importance in the fabrication of functional materials by self-assembly of colloidal nanocrystals.

In Chapter 6, we determine the phase diagram of hard equilateral and right-angled isosceles colloidal triangles in two dimensions using Monte Carlo simulations and free-energy calculations. Using our simulations we show that hard equilateral triangles and hard right-angled triangles undergo a phase transition from an isotropic phase to a triatic and rhombic liquid-crystal phase, respectively. With increasing pressures these liquid crystal phases continuously go to their respective close-packed crystal structures. These close-packed crystalline phases at high enough packing fractions give rise to a regular lattice of chiral holes. The observed enantiomers in both systems exhibit entropic demixing at large enough densities. The observed phase separation is similar to phase separation in the 2D Ising model, where the two phases form stripes to minimize the interfacial free energy. This chapter thus describes the first observation of the formation of such chiral phases and their phase separation in simulations of achiral hard particles.

Computing dispersion relations for colloidal crystals with diffusion, like truncated cubes in Chapter 2, is a challenging problem as the traditional method is developed for ideal systems where particles are always localized. In Chapter 7, we compute dispersion relations for colloidal crystal with diffusion using a recently developed theory in combination with Monte Carlo simulations. We compare the new theoretical method with the traditional microscopic approach and show that the traditional approach fails in computing the dispersion relations if there is diffusion in the crystals under investigation. Our results are in agreement with the result obtained using a density functional theory. The new method can be used in confocal microscopy to compute the elasticity coefficients and the dispersion relations for colloidal crystals without worrying about the diffusion of the particles. In addition, the computer codes written to compute the dispersion relations can be used to obtain the dispersion relations for experimental data sets very easily.

Samenvatting

Een colloïdale dispersie bestaat uit onoplosbare microscopische deeltjes die in een oplosmiddel gesuspendeerd zijn. Doorgaans wordt met de term "colloïde" een deeltje aangeduid waarvan tenminste één dimensie binnen het groottebereik van een nanometer tot een micrometer valt. Als gevolg van botsingen met veel kleinere oplosmiddelmoleculen vertonen colloïden Brownse beweging, hetgeen hen toestaat alle voor hen mogelijke beschikbare configuraties te verkennen. Behalve deze achtergrondwisselwerking met de atomen of moleculen van het oplosmiddel, wisselwerken in een fluïdum gesuspendeerde colloïden ook met elkaar. Als gevolg daarvan kunnen colloïden een rijk fasegedrag vertonen gelijksoortig aan dat van atomaire en moleculaire systemen. Colloïden kunnen bijvoorbeeld zelfassembleren tot niet alleen gas-, vloeistof- en vastestoffasen, maar ook tot nematische, smectische, biaxiale en hexatische fasen. Het soort fasen dat zich kan voordoen in een colloïdaal systeem hangt niet alleen af van de interactiepotentiaal tussen de colloïdale deeltjes maar ook van de vorm van het colloïdale deeltje zelf.

In dit proefschrift bestuderen we het effect dat de colloïdevorm heeft op zijn fasegedrag. In het bijzonder onderzoeken we het fasegedrag van experimenteel verkrijgbare veelvlakkige deeltjes met behulp van Monte-Carlosimulaties en vrije-energieberekeningen, zowel in de bulk als aan een oppervlak.

In Hoofdstuk 2 presenteren we ons onderzoek naar het thermodynamische fasegedrag van een familie afgeknotte harde kubussen waarvan de vorm geleidelijk overgaat van een kubus via een kuboctaëder tot een octaëder. We gebruiken Monte-Carlosimulaties en vrije-energieberekeningen om een volledig fasediagram vast te stellen. Verrassend genoeg vertoont dit fasediagram een opmerkelijke diversiteit aan niet-dichtgestapelde en dichtgestapelde structuren, inclusief een volledig ontaarde kristalstructuur en een kristalfase gestabiliseerd door vacatures; dit alles fijngevoelig afhankelijk van de precieze deeltjesvorm. Daarnaast onderzoeken we de aard van de plastische kristalfases die zich voordoen voor middelhoge dichtheden en maten van afknotting. Onze resultaten laten zien dat de oriëntationele distributiefunctie van plastische kristallen van harde anisotropische deeltjes zeer anisotroop kan zijn, en zeer sterk gepiekt voor bepaalde oriëntaties. Deze oriëntaties hangen niet alleen af van de kristalstructuur van het deeltje maar ook van de vorm van het deeltje. Onze resultaten laten zien dat de aard van plastische kristallen van harde deeltjes anders is dan die van plastische kristallen gevormd uit deeltjes met langedrachtswisselwerkingen. Onze resultaten maakten het mogelijk voor ons om het verband tussen fasegedrag en bouwblokvorm te onderzoeken en om het inzicht in rotatorfasen te verbeteren.

Behalve het fasegedrag bestuderen en berekenen we, in Hoofdstuk 3, ook de evenwichtsdichtheid van vacatures voor deze afgeknotte kubussen. Met behulp van een aangepaste Einsteinintegratiemethode bepalen we de vrije energieën van afgeknotte kubussen als functie van vacaturedichtheid. Uit onze berekeningen blijkt dat de evenwichtsdichtheid van vacatures van afgeknotte kubussen toeneemt met toenemende mate van afknotting bij een vaste pakkingsfactor van $\phi = 0.56$. Met behulp van eenvoudige celtheoretische berekenin-

gen laten we zien dat de toename van vacaturedichtheid met de mate van afknotting komt doordat de oriëntationele entropie toeneemt met toenemende mate van afknotting.

We bestuderen het fasegedrag van afgeronde afgeknotte kubussen, ook wel superballen genoemd, in Hoofdstuk 4. In dit Hoofdstuk gebruiken we Monte-Carlosimulaties en vrije-energieberekeningen om het fasegedrag te bepalen van colloïdale harde superballen waarvan de vorm interpoleert tussen kubussen en octaëders via bollen. We vonden niet alleen een stabiel vlakgecentreerd kubisch (fcc) plastisch kristal voor bijna-bolvormige deeltjes, maar ook een stabiel ruimtelijk gecentreerd kubisch (bcc) plastisch kristal dichtbij de octaëdervorm. Bovendien zagen we ook coëxistentie van deze twee plastische kristallen, met een aanzienlijk dichtheidsverschil. De plastische fcc- en bcc-kristallen zijn echter beide instabiel in de kubus- en octaëderlimiet, hetgeen suggereert dat de lage asfericiteitsverhouding van de superballen in combinatie met lokale kromming (afgeronde hoeken en gekromde vlakken) van de superballen een belangrijke rol speelt in het stabiliseren van de rotatorfase. Bovendien vonden we een tweestappig smeltfenomeen voor harde octaëders, waarbij een Minkowskikristal smelt tot een metastabiel plastisch bcc-kristal alvorens te smelten tot de fluïde toestand.

In Hoofdstuk 5 presenteren we een gecombineerde theoretische en simulationele studie in twee dimensies naar de zelfassemblage van colloïdale nanodeeltjes die de vorm hebben van hexagonale bipiramiden en hexagonale dubbele afgeknotte piramiden. De zelfgeassembleerde structuren die we verkrijgen uit de simulaties zijn in goede overeenstemming met de structuren die in experimenten met colloïdale nanokristallen zijn gezien. Onze resultaten laten zien dat de superroosterformatie vooral gedreven wordt door een minimalisatie van de vrije energieën van de grensvlakken en de maximalisatie van de stapelingsdichtheden. Daarnaast lieten onze resultaten zien dat een afknotting van de toppen van de bipiramiden van slechts 5% genoeg is om de symmetrie van het resulterende superrooster te veranderen van hexagonaal tot tetragonaal. Dit toont aan dat een precieze beheersing van de vorm van cruciaal belang is voor de vervaardiging van functionele materialen door zelfassemblage van colloïdale nanokristallen.

In Hoofdstuk 6 bepalen we het fasediagram van harde gelijkzijdige en rechthoekige gelijkbenige colloïdale driehoeken in twee dimensies met behulp van Monte-Carlosimulaties en vrije-energieberekeningen. Met behulp van onze simulaties laten we zien dat harde gelijkzijdige driehoeken en harde rechthoekige driehoeken een faseovergang ondergaan van een isotrope fase naar respectievelijk een triatisch en een ruitvormig vloeibaar kristal. Met toenemende druk gaan deze kristalfasen op continue wijze over naar hun dichtgestapelde kristalstructuren. Bij voldoende hoge pakkingsfactor brengen deze dichtgestapelde kristalfasen een regulier rooster teweeg van chirale gaten. De gevonden enantiomeren in beide systemen vertonen entropische ontmenging bij voldoende hoge dichtheden. Deze gevonden fasescheiding is gelijksoortig aan fasescheiding in het tweedimensionaal Isingmodel, waar de twee fasen strepen vormen om de vrije energie van de grensvlakken te minimaliseren. Dit Hoofdstuk beschrijft dus de eerste observatie van de vorming van chirale fasen en hun fasescheiding in simulaties van achirale harde deeltjes.

Het uitrekenen van dispersierelaties voor colloïdale kristallen waarin diffusie plaatsvindt, zoals bij de afgeknotte kubussen in Hoofdstuk 2, is een uitdagend probleem omdat de gebruikelijke methode ontwikkeld is voor ideale systemen waarin deeltjes altijd op hun plaats blijven. In Hoofdstuk 7 rekenen we dispersierelaties uit voor colloïdale kristallen

met diffusie, met behulp van een onlangs ontwikkelde theorie in combinatie met Monte-Carlosimulaties. We vergelijken de nieuwe theoretische methode met de gebruikelijke microscopische aanpak en laten zien dat de gebruikelijke aanpak te kort schiet bij het berekenen van de dispersierelaties als zich diffusie voordoet in het desbetreffende kristal. Onze resultaten zijn in overeenkomst met het resultaat verkregen uit een dichtheidsfunctionaaltheorie. Deze nieuwe methode kan gebruikt worden in confocale microscopie om de elasticiteitscoëfficiënten en de dispersierelaties uit te rekenen zonder zich zorgen te hoeven maken over de diffusie van de deeltjes. Daarbij kunnen de computercodes om de dispersierelaties te berekenen gemakkelijk gebruikt worden om ook de dispersierelaties voor experimentele datasets te verkrijgen.

Acknowledgments

To obtain a doctorate in physics has been a life time goal and I couldn't have realized this dream without the help and support of many people. I would like to take this opportunity to thank all those.

First and foremost, I would like to express my sincere gratitude towards Marjolein Dijkstra, my supervisor. Marjolein, the past three odd years have been a great learning experience and I could not have wished for a better supervisor. Thanks for always being kind and patient with me. I also appreciate the fact that you keep the door always open, to discuss the progress of my work. I have learned many scientific, social and management skills from you, which will help me succeed in my future career.

I would like to thank Alfons van Blaaderen, René van Roij, Arnout Imhof, Marijn van Huis, and Laura Filion for creating an excellent atmosphere to work in a multi-cultured and interdisciplinary environment. In particular, I thank Alfons and René for your enthusiasm and curious questions on my work during the combined work discussions, this always motivated me to present often and conduct effective research. I like to thank Krassimir Velikov and Patrick Baesjou for organizing industrial lab tours and for useful discussions. In addition, I also like to thank all the other staff, Peter, Judith, Thea and Marion for a lot of help and support both technically and at the administrative level.

This thesis wouldn't have been possible without the contributions from my collaborators. I am truly grateful to Joost de Graaf, for the successful collaboration on the truncated cubes project and his numerous suggestions about writing scientific documents; Ran Ni, for fruitful collaboration in constructing the phase diagram of superballs and sharing many insights about research in soft matter; Celso de Mello Donega and Ward van der Stam for letting me work on the self-assembly of hexagonal bipyramids and bifrustums; Giuseppe Soligno and René van Roij for collaborating in calculating the equilibrium orientation of anisotropic colloids at an interface; Matthias Fuchs, Johannes Häring and Tadeus Ras for hosting me in Konstanz and introducing to me new methods to compute dispersion relations for colloidal systems. Especially, I thank Tadeus Ras for not only being a great host but for also spending a lot of time explaining the intricacies of different theoretical approaches. Last, but not the least I would like to thank Weikai Qi for introducing me to the exciting statistical physics hidden in 2D colloidal systems.

Further, I would like to thank my students Jan-Willem Buurlage, Gerhard Burger and Nick Tasios. I have learned more programming skills from you than I learned on my own. Working with all of you was both a pleasure and a great learning experience in many dimensions.

Next, I like to thank Bob Evans for "interesting education" in the pubs during his visits to Utrecht. A special thanks goes to Frank Smallenburg for many useful discussions and for his help during my first few days in the SCM group. Moreover, I want to thank all of my lovely officemates, Frank Smallenburg, Ran Ni, Simone Dussi and John Edison. Thank you all for many dinners, pub nights and lively discussions on various topics such as simulation methods, general physics, mars (our cluster), cultural and food habits in

different countries, Bollywood/Tollywood film industry... Thanks for all the fun we had over the years.

My stay in Utrecht was pleasant and joyful, it wouldn't have been possible without many of you. I would like to thank many other co-workers from the SCM group who were helpful many times. Marlous, Nina, Henriëtte, Wessel and especially Thijs for explaining many experimental and synthesis details which made my education in soft matter systems complete and also for many miscellaneous joyful occasions. Many thanks to Rao for interesting discussions about the latest literature, Indian politics and movies. A special thanks goes to Marlous and Ernest for decoding my Dutch letters and for dealing with my cunning housing agents. Bas Kwaadgras for translating this thesis summary into het Nederlands and for the miscellaneous things we did together!

Doing sports always helped me take a break from work and refresh. I would like to thank a lot of people for filling my free time with sports. John, Bas and Henriëtte for fun times at Ultimate Frisbee; SCM Badminton team: Wiebke, Srivatssan, Tian-Song, Jessi and many others for regularly making me run and gasp in the badminton court; Teun, Frank and Helene for indoor rock climbing during my first year and for after beers.

All of above, as well as Zdenek, Guido, Tonnishtha, Kristina, Somil, Rik, Murphy, Berend, Harini, Vasileios, Douglas, Johan, Fabian, Bart, Da, Bo, Chanming, Yang, Arjen, Marjolein van der Linden, Djamal, Jissy, Simone Belli, Jeffrey, Bram, Mathijs, Sela, Niels, Thomas and Andreas are thanked for all the good times we had at our coffee breaks, lunches and/or pub times we shared. Also, I enjoyed going to various conferences and group outings with you.

In addition to friends at work, I have met many friends in Utrecht outside office during the last years. In particular the Indian community at Utrecht: Deepa, Sai, Ram, Aridaman, Vamshi, Sada, Mohit, Tanmay, Akshay, Tanmoy, Krishna, Subha, Akshatha, Sudhanshu, Bhavya and Harinath. I always had fun meeting you guys for dinners, drinks and debates.

Many professors/lecturers from my undergraduate and graduate studies have motivated me to pursue a career in physics. Of those, most notably the lectures of K. P. N. Murthy and V. S. S. Sastry have encouraged me embrace computational physics. I thank you both for introducing me to statistical physics of soft matter systems during my masters program at University of Hyderabad, India. Especially, K. P. N. Murthy, your lectures and supervision during my masters have influenced me greatly. I also like to thank fellow lab/class/room mates in my masters, from whom I benefited greatly: Trivikram, Preethi, Jaya Sri, Sridhar, Vamshi, Eswar, Rajesh, Manoj, Guru, Kuru, Suresh and Tarak. It is also a pleasure to thank my dear friends Sankaran, Arun, Venkat, Frank, Shervin, Rudolf, Oliver, Vamshi and Florian who were there for me in important times and also for being good friends, when I was working in Stuttgart. Further more, I like to thank Christian Holm, ICP, Stuttgart for his support to continue my research career. I would also like to thank all of my friends back home (India), in the Netherlands and abroad for the good times.

I further would like to thank my cousins Naga Raju, Ramalingamiah and Venkatesh for their unconditional support. I am grateful to my family, especially my mom, dad and brother Chowdappa, for all the support and help.

Finally, for your love, support and for always being there for me: thanks Raji!

List of Publications

This thesis is based on the following publications:

- Ward van der Stam, Anjan P. Gantapara, Quinten A. Akkerman, Giuseppe Soligno, Johannes D. Meeldijk, René van Roij, Marjolein Dijkstra, and Celso de Mello Donega, *Self-assembly of colloidal hexagonal bipyramid-and bifrustum-shaped ZnS nanocrystals into two-dimensional superstructures*, Nano Letters **14**, 1032 (2014)

- Anjan P. Gantapara, Joost de Graaf, René van Roij, and Marjolein Dijkstra, *Phase diagram and structural diversity of a family of truncated cubes: degenerate close-packed structures and vacancy-rich states*, Phys. Rev. Lett. **111**, 015501 (2013)

- Ran Ni, Anjan P. Gantapara, Joost de Graaf, René van Roij, and Marjolein Dijkstra, *Phase diagram of colloidal hard superballs: from cubes via spheres to octahedra*, Soft Matter, **8**, 12135 (2012)

- Anjan P. Gantapara, Weikai Qi and Marjolein Dijkstra, *Phase behavior of 2D hard triangles*, in preparation

- Anjan P. Gantapara, Joost de Graaf, René van Roij, and Marjolein Dijkstra, *Phase Behavior of a Family of Truncated Hard Cubes*, in preparation

- Anjan P. Gantapara, Johannes Haering, Tadeus Ras, Matthias Fuchs, and Marjolein Dijkstra *Dispersion relations for colloidal crystals with diffusion*, in preparation

Other publications by the author:

- Nick Tasios, Anjan P. Gantapara, and Marjolein Dijkstra, *Glassy dynamics of convex polyhedra*, accepted in J. Chem. Phys (2014).

- Weikai Qi, Anjan P. Gantapara, and Marjolein Dijkstra, *Two-stage melting induced by dislocations and grain boundaries in monolayers of hard spheres*, Soft Matter **10**, 5449 (2014)

- M. Suman Kalyan, Anjan P. Gantapara, V. S. S. Sastry and K. P. N. Murthy, *A note on non-equilibrium work fluctuations and equilibrium free energies*, Physica A, **390**, 1240 (2011).

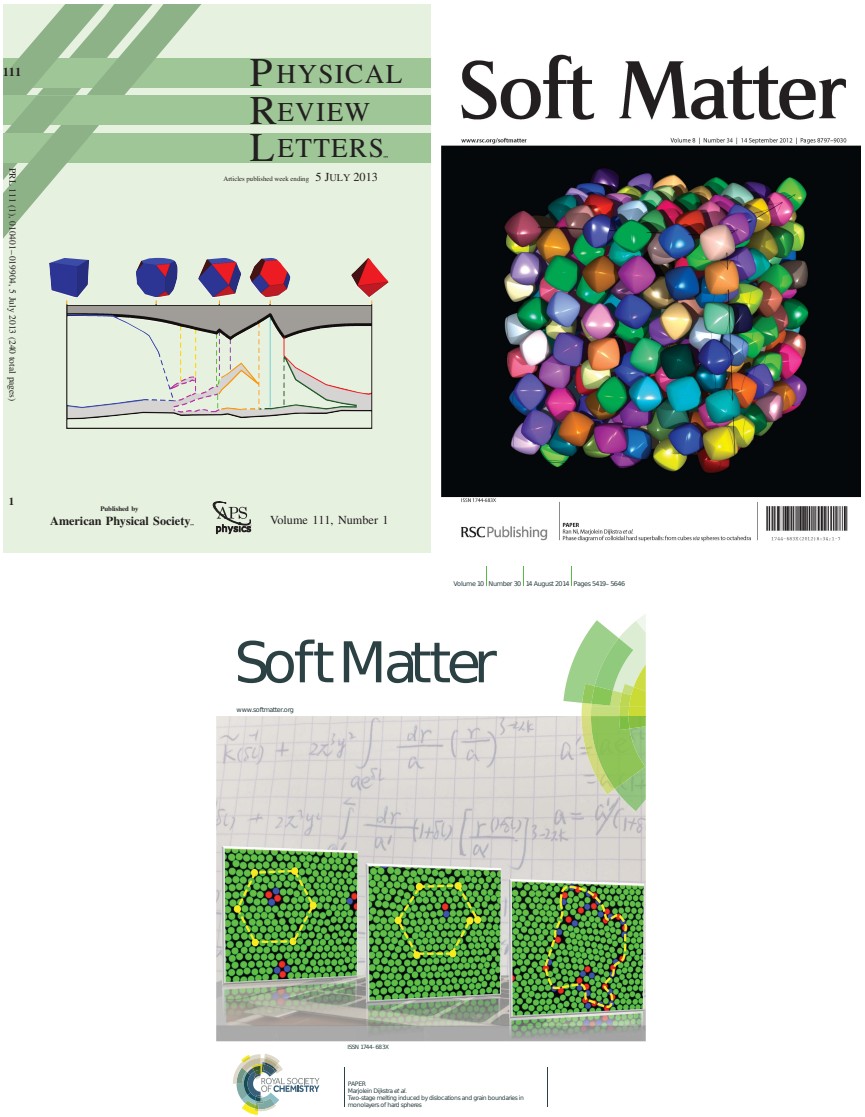

Figure: Covers featuring the research in Refs. [49], [77] and [179], respectively. (Top left) Reprinted by permission from the American Physical Society: Physical Review Letters volume 111 issue 1, copyright (2013). (Top right) Reprinted by permission from Royal Society of Chemistry: Soft Matter volume 8 issue 34, copyright (2012). (Bottom) Reprinted by permission from Royal Society of Chemistry: Soft Matter volume 10 issue 30, copyright (2014).